

School of Science  
Department of Physics and Astronomy “Augusto Righi”  
Master’s Degree in Astrophysics and Cosmology

# **Cosmological Constraints with Standard Sirens: Tackling Galaxy Catalog Incompleteness in Current Gravitational Wave Analysis**

**Candidate:**  
Giulia Cuomo

**Supervisor:**  
Prof. Michele Ennio Maria  
Moresco

**Co-supervisors:**  
Dr. Nicola Borghi  
Dr. Matteo Tagliazucchi



# Abstract

Gravitational waves (GWs) provide independent distance measurements when used as standard sirens, but require additional redshift information in order to operate as *cosmological probes*; this type of information can be obtained from real galaxy catalogs via statistical association with potential hosts. The limitations of such catalogs in different sky regions, however, must be properly accounted for to ensure robust and unbiased results.

This work focuses on the development of the necessary updates to the Bayesian framework in the CHIMERA pipeline to correctly model the incompleteness of a real galaxy catalog (GLADE+).

The developed pipeline, together with galaxy luminosity weighting, are tested on a selection of events taken from the GWTC-3 catalog: two significant GW events are used to produce statistical inferences for the Hubble constant ( $H_0$ ), and a sample of 42 Binary Black Hole events is analyzed through a Markov Chain Monte Carlo simulation: this allows for a joint estimation of cosmological and astrophysical parameters.

The Thesis highlights the need to account for galaxy catalog incompleteness in standard siren analyses and demonstrates the potential of the updated CHIMERA pipeline to perform cosmological analyses on real data, especially in anticipation of upcoming GW data from the LVK detector network.



# Contents

<b>Introduction</b>	<b>1</b>
<b>1 Gravitational waves and the cosmological scenario</b>	<b>3</b>
1.1 The Cosmological Setting . . . . .	3
1.1.1 Luminosity distance . . . . .	4
1.1.2 Components of the universe in the $\Lambda$ CDM model . . . . .	5
1.2 Gravitational Wave Theory . . . . .	6
1.2.1 The Transverse-Traceless gauge . . . . .	7
1.2.2 The Energy-Momentum Tensor of Gravitational Waves . . . . .	8
1.2.3 Interaction of Gravitational Waves with Test Masses . . . . .	8
1.2.4 Sources of Gravitational Waves . . . . .	9
1.2.5 Gravitational Waves from a Compact Binary System . . . . .	10
1.2.6 Gravitational Wave Propagation in a Cosmological Setting . . . . .	11
1.3 Gravitational Waves as Cosmological Probes . . . . .	12
1.4 Gravitational Wave Detectors . . . . .	13
1.5 Bayesian Inference . . . . .	15
1.6 Population Models . . . . .	16
1.7 Catalog Completeness . . . . .	18
<b>2 Data and Methods</b>	<b>20</b>
2.1 The GWTC-3 Catalog . . . . .	20
2.1.1 Selection criteria . . . . .	20
2.2 The GLADE+ Galaxy Catalog . . . . .	25
2.2.1 The Sub-Catalogs . . . . .	26
2.2.2 The construction of GLADE+ . . . . .	27
2.2.3 Redshift and redshift errors in GLADE+ . . . . .	28
2.3 The CHIMERA framework . . . . .	31
2.4 Extending the CHIMERA framework to the analysis of real data . . . . .	32
2.5 Accounting for GW and electromagnetic selection effects . . . . .	33
2.5.1 The injection method . . . . .	34
2.5.2 Computing GW selection effects in CHIMERA . . . . .	37
2.5.3 Computing the completeness term in CHIMERA . . . . .	38
2.5.4 The updated CHIMERA workflow . . . . .	42
<b>3 Results from GWTC-3 data</b>	<b>44</b>
3.1 Applying the new framework to two representative events . . . . .	45
3.1.1 GW170817 as a dark siren . . . . .	46
3.1.2 GW190814: a benchmark dark siren . . . . .	49
3.2 Applying the new framework to a sample of 42 BBH events from GWTC-3 . . . . .	54

3.2.1	1-D analysis of $H_0$ . . . . .	54
3.2.2	Full MCMC analysis . . . . .	61
<b>4</b>	<b>Conclusions and Future Prospects</b>	<b>67</b>
<b>A</b>	<b>Additional plots</b>	<b>73</b>
A.1	GWTC-3 BBH sample - mean properties . . . . .	73
A.2	GWTC-3 BBH sample - posteriors KDEs . . . . .	74
A.3	PLPLUSUNIF distribution . . . . .	74
A.4	Full MCMC corner plot . . . . .	75
A.5	MCMC step plots . . . . .	76
A.6	GLADE+ weighted galaxy interpolant . . . . .	77



# Introduction

Since the first detection in 2015 (B. P. Abbott et al. 2016), Gravitational Waves (GWs) have provided yet another proof of Einstein’s theory of General Relativity. Beyond that, they are consolidating as powerful cosmological probes, providing independent measurements of the expansion history of the Universe.

Currently, the best cosmological framework used to describe the Universe is the  $\Lambda$ CDM model, which identifies four main matter-energy components: Dark Energy (as the cosmological constant  $\Lambda$ ), Cold Dark Matter (CDM), relativistic matter (radiation), and non-relativistic baryonic matter. In addition to this, the  $\Lambda$ CDM model also accounts for the Universe’s observed accelerated expansion (Riess, Adam G. et al. 1998).

The measurement of these features required the development of new methods, such as the use of Type Ia Supernovae and the Cosmic Microwave Background (CMB). With the increase in accuracy, discrepancies such as the *Hubble tension* (Verde, Treu, and Riess 2019) have arisen, for which consistently different values of the local expansion rate of the Universe ( $H_0$ ) are found and have yet to be explained, either by previously unaccounted-for systematic effects or new physics.

The importance of GWs lies in their ability to provide independent luminosity distance measurements that are not based on the knowledge of the source’s electromagnetic properties. Therefore, they can help break the *Hubble tension* in the measurement of  $H_0$  (D. A. Holz 2005). For this reason, GW signals are referred to as *standard sirens*, as opposed to conventional cosmological probes such as *standard candles* and *standard rulers*. In the last decade, the LIGO-Virgo-KAGRA (LVK) Detector Network has observed GW signals from various binary systems, including Binary Black Holes, Binary Neutron Stars, and Neutron Star-Black Hole binaries. The LVK Collaboration has published data from its first three observing runs (O1, O2, O3a, O3b) and is currently conducting the fourth observing run (O4), with a fifth campaign (O5) planned for the future.

The main challenge in using GWs as cosmological probes lies in the inherent degeneracy between binary masses and the redshift at which the sources are located. When no *electromagnetic counterpart* is available to provide redshift information, different approaches can be used. The most widely developed methods include the *dark siren* approach, which makes use of external galaxy catalogs to provide redshift information, and the *spectral siren* approach, which breaks the mass-redshift degeneracy by including information on astrophysical population models. The current state-of-the-art methodology combines these two approaches. For this purpose, different codes have been developed to provide joint constraints to cosmological and astrophysical population parameters: ICAROGW (Mastrogiovanni et al. 2021), GWCOSMO (Gray, R et al. 2023, Gray, Messenger, and Veitch 2022, Rachel Gray et al. 2020) and CHIMERA (Borghi, Mancarella, Moresco, et al. 2024). The latter is the code I extended and used to produce the results at the core of this Thesis.

The main goal of this Thesis was the production of constraints of cosmological and population parameters starting from real galaxy and gravitational data, accompanied by a study on the systematic effects introduced by the use of real catalogs; this in turn required me to extend the CHIMERA pipeline and to focus on different areas:

- Analyzing the data; GW information that was used in this work was extracted from the GWTC-3 catalog (Abbott, R. et al. 2023a), whereas the galaxy data was taken from the GLADE+ catalog (Dály, G. et al. 2022).
- Adapting the code's modules to the extraction of real galaxy and GW data from publicly available repositories.
- Compensating for the galaxy catalog's incompleteness at higher redshift; this portion of the work in particular was the most relevant and required the adaptation of various modules of the code to the introduction of the necessary corrective terms.
- Modifying the selection bias term, which is one of the main components of the statistical inference, to account for the catalog's incompleteness.
- Updating the selection bias term to the use of *injection data* meant to simulate a GW catalog.

In order to test the updated framework of the code I conducted tests on a selection of GW events and compared the best results to those found in the existing literature.

The work can be summarized as follows:

1. Chapter 1 contains an overview of the theoretical subjects necessary to the understanding of the work; the cosmological setting is described, along with descriptions of its main quantities and definitions, and is followed by a section which defines the theory at the basis of GW astrophysics.
2. Chapter 2 delves into the data that was used to perform statistical inference in this work and the methods that were employed for said purpose; starting from a presentation of the GLADE+ galaxy catalog and the GWTC-3 GW catalog, the chapter moves on to a brief overlook on the CHIMERA Python code, followed up by a description of the updates I applied to the selection bias term and an in-depth look at the way I implemented a completeness correction into the code's framework.
3. Chapter 3 presents the results obtained with the updated CHIMERA framework made in order to tests its capabilities; two significant GW events are used as benchmarks for the production of  $H_0$  statistical inferences with fixed population parameters, followed by a sample of 42 events; the latter are also used to perform a Monte Carlo Markov Chain simulation, which allows for a joint cosmological-astrophysical statistical analysis in which other parameters are set free to vary besides  $H_0$ .

The work ends with a list of the results I obtained and possible future prospects; most importantly, I stress the need to use the code to analyze GW data coming from future runs of the LVK detector network in order to improve the constraints on both cosmological and astrophysical parameters; I also point to possible future applications of the CHIMERA code to the analysis of other cosmological parameters.

# Chapter 1

## Gravitational waves and the cosmological scenario

The following Chapter contains an introduction to the theoretical concepts and assumptions referenced throughout the Thesis; a brief description of the main cosmological definitions and the theory behind gravitational wave astrophysics is followed by an introduction to Bayesian inference with gravitational waves and the completeness correction term that must be applied in the context of dark sirens.

### 1.1 The Cosmological Setting

Cosmology, intended as the study of the origin and evolution of the Universe, aims to effectively describe it by means of a cosmological model, a set of equations and physical parameters regulated by basic assumptions.

One such model, today taken as the best available one, is the *Standard Cosmological Model*; the two main assumptions behind it are the following:

- Gravity is well-described by the theory of *General Relativity*.
- The Universe is everywhere *homogeneous and isotropic* (*Cosmological Principle*).

The Universe's geometry can be described with a metric  $g_{\mu\nu}$ , which defines a space-time interval in the following form

$$ds^2 = g_{\mu\nu} dx^\mu dx^\nu, \quad (1.1)$$

by means of its energy content. This is encapsulated by the *Einstein's Field Equation*

$$R_{\mu\nu} - \frac{1}{2}g_{\mu\nu}R - g_{\mu\nu}\Lambda = \frac{8\pi G}{c^4}T_{\mu\nu}, \quad (1.2)$$

which relates the mass (or energy) content of the Universe, here represented by the *energy-momentum tensor*  $T_{\mu\nu}$ , with the curvature of space-time (by means of  $g_{\mu\nu}$ , the Ricci tensor  $R_{\mu\nu}$  and the Ricci scalar  $R$ ); the equation also contains the  $-\Lambda g_{\mu\nu}$  term introduced by Einstein in 1921 to represent a negative pressure component,  $c$  as the speed of light, and  $G$  as the cosmological constant.

Assuming that the Universe's eventual curvature can be defined by means of a *curvature parameter*  $K$  (which is equal to 0 in the case of a flat Universe), the metric defined in 1.1 can be parametrized

as follows, when all mixed time and space terms are zero according to the Cosmological Principle:

$$\begin{aligned} ds^2 &= c^2 dt^2 - a^2(t) \left[ \frac{dr^2}{1 - Kr^2} + r^2 (d\theta^2 + \sin^2 \theta d\phi^2) \right] \\ &= c^2 dt^2 - a^2(t) \left[ \frac{dr^2}{1 - Kr^2} + r^2 d\Omega \right], \end{aligned} \quad (1.3)$$

where  $r$  is used to parametrize the radius in a Euclidian Universe,  $\Omega$  is defined as a solid angle and  $a(t)$  is the time-dependent *scale factor* of the Universe, which can be used to define the physical distance between two objects,  $r_{phys} = a(t) \cdot r$ .

From 1.2 and 1.3 one can derive a set of two equations, defined as the *Friedmann equations*, which relate the density of the different components of the Universe with its curvature and the evolution of the scale factor in time:

$$\begin{cases} \ddot{a}(t) = -\frac{4\pi G}{3} \left( \rho + \frac{3p}{c^2} \right) a(t) \\ \dot{a}^2(t) + Kc^2 = \frac{8\pi G}{3} \rho a^2(t). \end{cases} \quad (1.4)$$

It is possible to define the main parameters that characterize cosmological models and test them against observations:

- $H_0 := \frac{\dot{a}(t_0)}{a(t_0)}$ , defined as the *Hubble constant*. It describes the rate of expansion of the Universe at present day,  $t_0$ ;
- $\Omega_{i,0} := \frac{\rho_{i,0} 8\pi G}{3H_0^2}$ , the *density parameter* of a given component of the Universe at  $t_0$ ; if one defines the *critical density* at present day as  $\rho_{crit} := \frac{8\pi G}{3H_0^2}$ , the density parameter can be re-written as  $\Omega_{i,0} := \frac{\rho_0}{\rho_{crit,0}}$ .

These two parameters are related as follows:

$$H_0^2 \left( 1 - \sum_i \Omega_{i,0} \right) = -\frac{Kc^2}{a(t_0)^2}, \quad (1.5)$$

easily derivable if one divides the second equation in 1.4 by  $a(t_0)^2$  (or  $a_0^2$ ) when the equation is computed at  $t = t_0$ .

### 1.1.1 Luminosity distance

When considering the concept of distance in a Universe characterized by a given curvature parameter it is crucial to make a distinction between the concepts of *proper distance*, which is defined as

$$d_P := a \int_0^r \frac{dr}{\sqrt{1 - Kr^2}} \quad (1.6)$$

and *comoving distance*:

$$d_C := d_P(t_0). \quad (1.7)$$

While 1.6 represents the actual distance between two points given a curvature parameter, 1.7 is a constant value measured at present day which may be used as a reference distance.

When observing a luminous source, the expansion of the Universe results in different effects which act on the propagation of light and, in turn, affect the measure of distance:

- *time dilation*,  $\frac{dt}{dt_0} = \frac{a}{a_0}$ ;
- *redshift*, or loss of energy of the traveling photon:  $\frac{dE_0}{dE} = \frac{a}{a_0}$ ;
- *variations in the geodesic of the photon*, as given by the scale factor  $a$ :  $d_P(t_0) = a_0 r$ .

These different contributions concur in the definition of the *luminosity distance*  $d_L$ : given a light source of luminosity  $L$  from which we receive a given flux  $l$ ,

$$l = \frac{L}{4\pi a_0^2 r^2 (1+z)} \longleftrightarrow d_L := a_0 r (1+z). \quad (1.8)$$

Through an appropriate expansion of the scale factor in terms of the Hubble constant, the redshift and the *deceleration parameter*  $q_0 = -\frac{\ddot{a}a}{\dot{a}^2}$ , the luminosity distance can be defined in terms of these parameters as

$$d_L \simeq \frac{cz}{H_0} \left( 1 + \frac{1}{2}(1 - q_0)z \right). \quad (1.9)$$

This relation is relevant in the use of gravitational wave signals for the statistical inference of the value of  $H_0$  (see section 1.3).

## 1.1.2 Components of the universe in the $\Lambda$ CDM model

Depending on the choice for the curvature parameter, which defines the geometry of the Universe, and the set of components which are assumed to make up its energy content, we can produce different cosmological models.

The most widely accepted today is the flat  $\Lambda$ CDM *model*; its defining features are the following:

- A *Euclidian geometry*, given by  $K = 0$ ; the Universe is therefore assumed to be flat.
- A set of components made up of relativistic matter (radiation), non-relativistic baryonic matter, non-relativistic and non-baryonic matter (*Cold Dark Matter*) and *dark energy*, whose presence is identified by the *cosmological constant*  $\Lambda$ .

The different components' densities are defined by means of their Equation Of State parameters  $w_i$  as

$$\rho_i(z) = \rho_{i,0}(1+z)^{3(1+w_i)}, \quad (1.10)$$

where  $w = 0$  for both non-relativistic baryonic and non-baryonic matter,  $w = \frac{1}{3}$  for relativistic matter and  $w = -1$  for dark energy; equation 1.10 is the consequence of assuming that all components of the Universe expand adiabatically.

According to 1.5, a null curvature implies that  $\Omega_{TOT} = \sum_i \Omega_i = 1$ . If one considers the components of the Universe to be the ones listed above, we have the following condition on their density parameters:

$$\Omega_r + \Omega_m + \Omega_\Lambda = 1, \quad (1.11)$$

where  $\Omega_r$  is the density parameter of radiation,  $\Omega_m$  is that of the combined contribution of baryonic and dark matter and  $\Omega_\Lambda$  is given by the cosmological constant. Moreover, these three parameters can be related to the Hubble constant and the redshift-dependent *Hubble parameter*  $H(z)$  by the following equation:

$$H^2(z) = H_0^2 \left[ \Omega_m (1+z)^3 + \Omega_r (1+z)^4 + \Omega_\Lambda \right], \quad (1.12)$$

where we have used equations 1.5, 1.10, 1.11 and the relation:

$$\frac{a_0}{a} = 1 + z. \quad (1.13)$$

## Cosmological tensions and the importance of gravitational waves

Since the discovery of the accelerated expansion of the Universe by Riess, Adam G. et al. 1998, numerous probes have been used to characterize it by measuring the  $H_0$  parameter (Moresco et al. 2022): among these, the use of Type Ia Supernovae as *standard candles* to measure the distance between the observer and a given object, and measurements of the Cosmic Microwave Background.

With the increase in measurement accuracy, both due to the reduction of systematic errors and the development of new and better technology, the results obtained through the various available probes started showing discrepancies which could not be justified by uncertainty levels. As discussed in Verde, Treu, and Riess 2019, for example, discrepancies can arise from values of  $H_0$  obtained with different methods.

If one considers the value of  $H_0$  inferred by Aghanim, N. et al. 2020 ( $H_0 = 67.36 \pm 0.57 \text{ km/s/Mpc}$ ) with the Cosmic Microwave Background, and compares it to the one found through type Ia Supernovae distance measurements by Riess, Adam G. et al. 2022 with the SHOES collaboration ( $H_0 = 73.04 \pm 1.04 \text{ km/s/Mpc}$ ), the difference is noticeable and does not seem to be justified by the measurements' uncertainties.

For these reasons, the development of new methods such as gravitational wave inference, which allow to probe different epochs of the Universe's history, is pivotal in pinpointing the origins of such discrepancies, whether they lie in unforeseen systematic effects or unknown physics.

## 1.2 Gravitational Wave Theory

The starting point of the theory of gravitational waves is a linearized approach to Einstein's Field Equation; this means that it is based on the following expansion of the metric:

$$g_{\mu\nu} = \eta_{\mu\nu} + h_{\mu\nu} \quad \wedge \quad |h_{\mu\nu}| \ll 1. \quad (1.14)$$

It is possible to see how, in the linearized approximation, the metric tensor can be seen as a sum of a flat metric tensor ( $\eta_{\mu\nu}$ ) and a small *perturbation term* ( $h_{\mu\nu}$ ).

This specific choice leads to a loss of freedom when it comes to the conservation of Einstein's Field Equation in all possible coordinate sets, which is granted in the general case. We can however find a specific coordinate change which keeps the equation's validity:

$$x^\mu \longrightarrow x'^\mu = x^\mu + \xi^\mu(x). \quad (1.15)$$

By applying coordinate transformation laws one can derive an expression for the  $h$  term in the new coordinate system:

$$h_{\mu\nu}(x) \longrightarrow h'_{\mu\nu}(x) = h_{\mu\nu}(x) - (\partial_\mu \xi_\nu + \partial_\nu \xi_\mu); \quad (1.16)$$

This expression can then be used to derive a linearized version of the Riemann tensor,

$$R_{\mu\nu\rho\sigma} = \frac{1}{2} (\partial_\nu \partial_\rho h_{\mu\sigma} + \partial_\mu \partial_\sigma h_{\nu\rho} - \partial_\mu \partial_\rho h_{\nu\sigma} - \partial_\nu \partial_\sigma h_{\mu\rho}). \quad (1.17)$$

This adaptation to the linear approximation is summarized by the linearized version of the Field Equation:

$$\begin{aligned}\square \overline{h_{\mu\nu}} + \eta_{\mu\nu} \partial^\rho \partial^\sigma \overline{h_{\rho\sigma}} - \partial^\rho \partial_\nu \overline{h_{\mu\rho}} - \partial^\rho \partial_\mu \overline{h_{\nu\rho}} &= -\frac{16\pi G}{c^4} T_{\mu\nu} \\ \wedge h_{\mu\nu} &= \overline{h_{\mu\nu}} - \frac{1}{2} \eta_{\mu\nu} \overline{h} \\ \wedge \overline{h_{\mu\nu}} &= h_{\mu\nu} - \frac{1}{2} \eta_{\mu\nu} h \\ \wedge h &= \eta_{\mu\nu} h^{\mu\nu} = \overline{h}.\end{aligned}\tag{1.18}$$

One can reduce 1.18 to a simpler form by setting a *gauge*, a choice that modifies or nullifies one or more components within the equation. In this case we opt for the *Lorentz gauge*, whose definition is given by

$$\partial^\nu \overline{h_{\mu\nu}} = 0;\tag{1.19}$$

by applying a change of variables to  $\overline{h_{\mu\nu}}$ ,

$$\overline{h_{\mu\nu}} \longrightarrow \overline{h'_{\mu\nu}} = \overline{h_{\mu\nu}} - (\partial_\mu \xi_\nu + \partial_\nu \xi_\mu - \eta_{\mu\nu} \partial_\rho \xi^\rho),\tag{1.20}$$

the Lorentz gauge is given by

$$\partial^\nu \overline{h'_{\mu\nu}} = 0.\tag{1.21}$$

This in turn is the result of the application of a *harmonic condition* (equation 1.22) on the  $\partial^\nu$  partial derivative of equation 1.20:

$$\square \xi_\mu = \partial^\nu h_{\mu\nu};\tag{1.22}$$

The Einstein Field Equation is then simplified to the following form:

$$\square \overline{h_{\mu\nu}} = -\frac{16\pi G}{c^4} T_{\mu\nu},\tag{1.23}$$

which appears to have wave-like solutions. The conservation of energy is a natural consequence of 1.23, since the Lorentz gauge forces  $\partial^\nu T_{\mu\nu} = 0$ . Overall, the Lorentz gauge reduces the number of degrees of freedom of Einstein's Field Equation from ten to six.

### 1.2.1 The Transverse-Traceless gauge

Further assumptions can be made on the  $h_{\mu\nu}$  tensor when we consider the vacuum setting ( $T_{\mu\nu} = 0$ ); for instance, by applying the following set of conditions,

$$h^{0\mu} = 0, \quad h^i_i = 0, \quad \partial^j h_{ij} = 0,\tag{1.24}$$

the number of degrees of freedom of Einstein's Field Equation can be further reduced to two. This means that  $h_{\mu\nu}$ , which defines the propagation of a wave in vacuum, can be factorized in two different polarizations: *plus* (+) and *cross* (×). If we assume the direction of propagation of the wave to coincide with the z-axis,

$$h_{ij}^{TT}(t, z) = \begin{bmatrix} 0 & 0 & 0 & 0 \\ 0 & h_+ & h_\times & 0 \\ 0 & h_\times & -h_+ & 0 \\ 0 & 0 & 0 & 0 \end{bmatrix}.\tag{1.25}$$

This expression can be simplified by defining a matrix  $A_{\mu\nu}^{TT}$  as follows:

$$A_{\mu\nu}^{TT} = h_+ e_+ + h_\times e_\times \quad \wedge \quad e_+ = \begin{bmatrix} 0 & 0 & 0 & 0 \\ 0 & 1 & 0 & 0 \\ 0 & 0 & -1 & 0 \\ 0 & 0 & 0 & 0 \end{bmatrix}, \quad e_\times = \begin{bmatrix} 0 & 0 & 0 & 0 \\ 0 & 0 & 1 & 0 \\ 0 & 1 & 0 & 0 \\ 0 & 0 & 0 & 0 \end{bmatrix},\tag{1.26}$$

## 1.2.2 The Energy-Momentum Tensor of Gravitational Waves

It is possible to prove that the passage of a gravitational wave through a region of space where test masses are present causes a variation of the velocity associated to said masses on their respective geodesics. In order to maintain energy conservation within such a system, it is necessary to assume that a gravitational wave carries energy and momentum. More specifically, gravitational waves are themselves sources of deformation in spacetime.

This becomes apparent when we express the metric tensor in terms of a background term and a gravitational wave term:

$$g_{\mu\nu} = \overline{g_{\mu\nu}}(x) + h_{\mu\nu}(x) \quad \wedge \quad |h_{\mu\nu}(x)| \ll 1; \quad (1.27)$$

the main difference between 1.27 and 1.14 is the fact that, in order to investigate the possible presence of curvature due to gravitational waves, we cannot see them as perturbations over a flat metric. We can then follow the same principle of linearization to expand the Ricci tensor into three terms:

$$R_{\mu\nu} = \overline{R_{\mu\nu}} + R_{\mu\nu}^{(1)} + R_{\mu\nu}^{(2)}, \quad (1.28)$$

where the first one is a background term, the second is related to the low-frequency component of a gravitational wave and the third is related to both the low and high-frequency components on the account of it being quadratic in nature.

After some manipulation it is possible to obtain the following expression for Einstein's Field Equation, which encapsulates the contribution of gravitational waves to the curvature of spacetime:

$$\begin{aligned} \overline{R_{\mu\nu}} - \frac{1}{2}\overline{g_{\mu\nu}}\overline{R} &= \frac{8\pi G}{c^4}(\overline{T_{\mu\nu}} + t_{\mu\nu}) \\ \wedge \quad t_{\mu\nu} &= -\frac{c^4}{8\pi G}\langle R_{\mu\nu}^{(2)} - \frac{1}{2}\overline{g_{\mu\nu}}R^{(2)} \rangle, \end{aligned} \quad (1.29)$$

where the term  $t_{\mu\nu}$  represents the gravitational wave's own energy-momentum tensor and the  $\Lambda$  term is momentarily neglected. Said term can be rewritten in a different form when the both the Ricci tensor and the Ricci scalar are explicitly computed:

$$t_{\mu\nu} = \frac{c^4}{32\pi G}\langle \partial_\mu h_{\alpha\beta}\partial_\nu h^{\alpha\beta} \rangle. \quad (1.30)$$

In the specific case of a gravitational wave expressed in the TT gauge and traveling along the direction of the z-axis we have the three following conditions:

$$t^{03} = t^{00} = \frac{c^2}{16\pi G}\langle \dot{h}_+^2 + \dot{h}_x^2 \rangle, \quad t^{01} = t^{02} = 0. \quad (1.31)$$

## 1.2.3 Interaction of Gravitational Waves with Test Masses

We can investigate the interaction of passing gravitational waves with a given detector by studying the simplified case of a set of test masses; the behavior of said test masses varies depending on the reference frame we adopt to observe them.

We start by defining the geodesic of an object that is free-falling along a curve parametrized by  $\tau$ , the *proper time* relative to the geodesic defined on  $x^\mu(\tau)$ :

$$\frac{dx^\mu}{d\tau^2} + \Gamma_{\nu\rho}^\mu(x)\frac{dx^\nu}{d\tau}\frac{dx^\rho}{d\tau} = 0. \quad (1.32)$$

If we define another geodesic with a  $\xi^\mu$  separation from the first as  $x^\mu(\tau) + \xi^\mu(\tau)$ , the equation that regulates the evolution of such separation is found to be

$$\frac{d^2\xi^\mu}{d\tau^2} + 2\Gamma_{\nu\rho}^\mu(x) \frac{dx^\nu}{d\tau} \frac{d\xi^\rho}{d\tau} + \xi^\sigma \partial_\sigma \Gamma_{\nu\rho}^\mu(x) \frac{dx^\nu}{d\tau} \frac{dx^\rho}{d\tau} = 0; \quad (1.33)$$

this is only true if the scale of the deviation  $|\xi^\mu|$  is much smaller than that of any variation in the gravitational field (this becomes relevant later).

As already anticipated, the frame of reference we use to study the laws of motion of a given object which is considered still at  $\tau$  varies according to the frame of reference we select.

### Test Masses in the TT Gauge

It can be demonstrated that the geodesic equation at  $\tau = 0$  as measured in what is called *TT frame* becomes that of a *local inertial frame*:

$$\left. \frac{d^2\xi^\mu(\tau)}{d\tau^2} \right|_{\tau=0} = 0. \quad (1.34)$$

This means that, when considered in the TT frame, a test mass remains still regardless of whether or not a gravitational wave traverses the region in which it is located. The coordinate separation between two events at  $x_1$  and  $x_2$  however, which can be identified by  $L$  in the TT gauge, is different than the *proper distance* between them:

$$s = (x_2 - x_1) [1 + h_+ \cos(\omega t)]^{\frac{1}{2}} \simeq L \left[ 1 + \frac{1}{2} h_+ \cos(\omega t) \right], \quad (1.35)$$

where  $\omega$  is the angular frequency of the passing gravitational wave.

### Test Masses in the Proper Detector Frame

An earthbound gravitational wave detector, as opposed to the TT frame, cannot be thought of as a local inertial frame. The coordinate separation between geodesics in such a frame, which also indicates the coordinate separation between our test masses, is described by the following law of motion:

$$\ddot{\xi}^i = \frac{1}{2} \dot{h}_{ij}^{TT} \xi^j. \quad (1.36)$$

Equation 1.35 is only valid when the scale of the geodesic deformation is much smaller than the scale of the deformation of the gravitational field induced by the gravitational wave, which is identified by  $\bar{\lambda} = \frac{\lambda}{2\pi}$ . It is apparent from equation 1.36 how the acceleration term can be non-null and how the effect of the passage of a gravitational wave is akin to that of a *Newtonian force* on the test masses. The proper separation  $L$  is needed to understand the functioning of gravitational wave detectors (Maggiore 2007).

## 1.2.4 Sources of Gravitational Waves

Gravitational wave signals can be of different types and originate from a variety of sources and events. When referring to a GW signal, it can be classified as one of four kinds: *burst*, *continuous*, *stochastic* and *inspiral*.

- Burst signals are related to transient events such as a massive star's collapse onto its core (this type is difficult to both detect and model);

- Continuous signals are produced by binary systems before they enter the inspiral phase or by the rotation of a compact source. The stability of such signals makes them harder to detect by comparison with a background;
- Stochastic signals have possibly originated from background variations of the metric of the early Universe ( $g_{\mu\nu} = g_{\mu\nu}^{(0)} + \delta g_{\mu\nu}$ );
- Inspirational signals, so far the only ones to have been detected, are short-lived signals produced by the last stages of the inspiral phases of binary systems.

With specific reference to the last type, it is useful to introduce the three types of compact body system that are most likely to generate a detectable signal in a so-called *Compact Binary Coalescence event* (or CBC):

- **Binary Neutron Star (BNS)** - the coalescence of two neutron stars results in a *kilonova*, an event characterized by a mass release in the form of a heated expanding ejecta (which can be of the order of  $10^3 - 10^{-2} M_{\odot}$  as in the case of GW170817, Abbott, B.P. et al. 2017b, Maggiore 2018) and a *Gamma Ray Burst* (GRB). Most importantly, a GW signal with a frequency up to 4 kHz is produced (Abbott, B.P. et al. 2017b). The presence of an accompanying electromagnetic signal in the form of a GRB and r-process nucleosynthesis in the ejecta (Maggiore 2018) is especially advantageous in the context of cosmological parameter inference (see section 1.3 and Chapter 3);
- **Neutron Star - Black Hole (NSBH)** pair - the coalescence of a neutron star with a black hole, also potentially accompanied by an EM signal;
- **Binary Black Hole (BBH)** - the coalescence of two black holes, which by definition is not usually accompanied by an EM signal but makes up the majority of observed CBC events.

As shown in the next sections, these types of sources present unique advantages in the determination of cosmological parameters: this is because they allow for a direct measurement of their luminosity distances from the observer without the need for a distance ladder, as is the case for *standard candles* such as Type Ia Supernovae.

## 1.2.5 Gravitational Waves from a Compact Binary System

A gravitational wave generated in linear regime has the following shape, which is a solution of 1.23:

$$\overline{h_{\mu\nu}}(t, x) = \frac{4G}{c^4} \int d^3x' \frac{1}{|x - x'|} T_{\mu\nu} \left( t - \frac{|x - x'|}{c}, x' \right). \quad (1.37)$$

The compact body approximation holds when the observer is located at a much larger distance from the system than the separation between its components. It is possible to prove that, in the center-of-momentum frame of the compact system, the expression of the gravitational waves generated by it is related to the space *quadrupole-moment tensor*  $I^{ij}$  as follows:

$$\overline{h_{ij}}(ct) = -\frac{2G}{c^6 r} \left[ \frac{d^2 I_{ij}}{dt'^2} \right]_{t=t_{ret}}. \quad (1.38)$$

If one considers the time-varying component of 1.38 and the observer whose line of sight forms an angle  $i$  with the normal to the system's orbit, it is possible to prove that, for a system of two objects

on a quasi-stationary circular orbit, we have the following two expressions for the cross and plus polarizations of the gravitational waves:

$$\begin{aligned} h_+ &= \frac{4G\mu R^2\omega_s^2}{c^4 r} \left( \frac{1 + \cos^2 i}{2} \right) \cos(2\omega_s t_{ret}) \\ h_\times &= \frac{4G\mu R^2\omega_s^2}{c^4 r} \cos i \sin(2\omega_s t_{ret}), \end{aligned} \quad (1.39)$$

where  $\omega_s$  is the angular frequency of the binary system, which happens to also be half the angular frequency of the gravitational wave ( $\omega_{gw} = 2\omega_s$ ). This expression can be simplified by introducing the *chirp mass*  $M_c = \mu^{\frac{3}{5}} m^{\frac{2}{5}}$  together with the gravitational wave frequency  $f_{gw}(\tau) = \frac{1}{8\pi} \left( \frac{5}{\tau} \right)^{\frac{3}{8}} \left( \frac{GM_c}{c^3} \right)^{-\frac{5}{8}}$  (where  $\tau$  is defined as the time until coalescence):

$$\begin{aligned} h_+ &= \frac{4}{r} \left( \frac{GM_c}{c^2} \right)^{\frac{5}{3}} \left( \frac{\pi f_{gw}}{2} \right)^{\frac{2}{3}} \left( \frac{1 + \cos^2 i}{2} \right) \cos(2\pi f_{gw} t_{ret}) \\ h_\times &= \frac{4}{r} \left( \frac{GM_c}{c^2} \right)^{\frac{5}{3}} \left( \frac{\pi f_{gw}}{2} \right)^{\frac{2}{3}} \cos i \sin(2\pi f_{gw} t_{ret}). \end{aligned} \quad (1.40)$$

When considering the fact that the frequency of the gravitational wave is time-dependent, the term  $\Phi(t) = \int_{t_0}^t dt' \omega_{gw}(t')$  can simply replace  $2\pi f_{gw} t_{ret}$  as the argument of the sin and cos functions in 1.40.

## 1.2.6 Gravitational Wave Propagation in a Cosmological Setting

Whilst retaining most of its features, a gravitational wave must adapt to propagation in a cosmological setting in three ways:

- the definition of the distance of the observer from the compact system, which can be expressed in terms of the luminosity distance;
- the definition of the frequency of the gravitational wave, which is affected by redshift;
- the definition of the chirp mass of the gravitational wave, which is affected by redshift.

1.40 can be rewritten as follows to account for the aforementioned effects:

$$\begin{aligned} h_+ &= h_c(t_s^{ret}) \left( \frac{1 + \cos^2 i}{2} \right) \cos \left( 2\pi \int^{t_{ret}} f_{gw}(t') dt' \right) \\ h_\times &= h_c \cos i \sin \left( 2\pi \int^{t_{ret}} f_{gw}(t') dt' \right) \\ h_c(t_c^{ret}) &= \frac{4}{d_L} \left( \frac{GM_c}{c^2} \right)^{\frac{5}{3}} \left( \frac{\pi f_{gw}^{obs}(t_{obs}^{ret})}{c} \right)^{\frac{2}{3}} \\ \mathcal{M}_c &= (1+z)M_c \\ f_{gw}^{obs}(t_{obs}^{ret}) &= \frac{1}{1+z} f_{gw}^s(t_s^{ret}). \end{aligned} \quad (1.41)$$

$\mathcal{M}_c$  is the result of the conversion of  $M_c$  from source to detector frame in a cosmological setting; the same applies to  $f_{gw}^{obs}(t_{obs}^{ret})$ . This factor becomes relevant when discussing the role of gravitational waves as cosmological probes in section 1.3.

### 1.3 Gravitational Waves as Cosmological Probes

The application of GW measurements was first introduced as a possibility by Schutz 1986, particularly when it came to the determination of the luminosity distance of a given source.

In principle, one can re-write equation 1.41 to obtain a combined expression for  $h(t)$  as

$$h(t) = \frac{\mathcal{M}_z^{5/3} f_{gw}(t)^{2/3}}{d_L} F(\text{angles}) \cos(\Phi(t)), \quad (1.42)$$

one can express it in terms of the frequency of the radiation alone; this is possible since it's proven that

$$\mathcal{M}_z = \left( \frac{5}{96} \pi^{-8/3} f_{gw}(t)^{-11/3} \dot{f}(t) \right). \quad (1.43)$$

The measurement of a gravitational wave's amplitude and frequency is not sufficient for the determination of the source's luminosity distance with a constraint better than  $\mathcal{O}(10\%)$ : this is because the components of the right-hand side of 1.43 are redshift-dependent (D. A. Holz 2005). In particular, a mass measurement in the detector's frame of reference is linked to that in the source's by the following relation:

$$m_{1,2}^{det} = m_{1,2}(1+z). \quad (1.44)$$

This factor introduces the need for an independent source of redshift information. Once said information is obtained, it is possible to link the definition of the luminosity distance to those of some relevant cosmological parameters through

$$d_L = c(1+z) \int_0^z \frac{dz'}{H_0 E(z')} \quad \wedge \quad E(z') = \sqrt{\Omega_{r,0}(1+z')^4 + \Omega_{m,0}(1+z')^3 + \Omega_{\Lambda,0}}, \quad (1.45)$$

which is true assuming a flat  $\Lambda$ CDM cosmology. There are three main ways to obtain independent redshift information for a given gravitational wave event:

- the *bright siren* approach, which makes use of an *electromagnetic counterpart* to the gravitational wave signal (Abbott, B.P. et al. 2017b); this method is valid for those inspiral events that can be associated to an *electromagnetic counterpart*: such is the case for Binary Neutron Stars when the merger coincides with a kilonova event (Borghi, Mancarella, Moresco, et al. 2024);
- the *dark siren* approach, which makes use of the sources contained in a galaxy catalog by statistically assigning redshift information from potential hosts within the gravitational wave's localization volume (Borghi, Mancarella, Moresco, et al. 2024);
- comparing the GW event with an assumed population model which describes the distribution in redshift of the event's type ; this approach is prone to systematic effects (Borghi, Mancarella, Moresco, et al. 2024, Moresco et al. 2022).

The last point in particular refers to a variety of possible approaches:

- GW signals alone can be matched to known features in their population distributions (Ezquiaga and Holz 2022); this last option is referred to as *spectral sirens*.
- When dealing with well-localized GW events, their spatial clustering as a function of luminosity distance can be matched to the distribution of galaxy clustering in redshift even with poorly-populated galaxy catalogs (MacLeod and Hogan 2008, Oguri 2016, Mukherjee and Wandelt 2018, Bera et al. 2020).

- Prior assumptions made about the redshift distribution of CBC merger events can be matched to the observed distance luminosity distribution relative to a set of GW sources (Ye and Maya Fishbach 2021).

As for the uncertainties in the measurements related to gravitational wave signals, future challenges may be related to calibration effects and waveform selection.

## 1.4 Gravitational Wave Detectors

The current gold-standard of gravitational wave detectors is represented by the ones that make up the *LVK Gravitational Wave Network*: the *Laser Interferometry Gravitational-Wave Observatory (LIGO)* (Aasi et al. 2015) located in two separate facilities (Hanford, WA (USA) and Livingston, LA (USA)), the *Virgo Gravitational Wave Interferometer* (Acernese, F et al. 2014) in Pisa (Italy) and the *Kamioka Gravitational Wave Detector (KAGRA)* (Akutsu, T. et al. 2019) in Kamioka-cho, Hida-city, Gifu-prefecture (Japan). These detectors were designed following the same layout, a *Michelson-Morley interferometer*, and are comprised of the following set of key components:

- a laser beam;
- a *beam-splitter*, which can reflect a portion of the laser beam and leave the remaining one unaffected;
- two km-long arms over which the laser beam can propagate;
- two *Fabry-Perot cavities* positioned along the two arms, whose purpose is lengthening the space over which the laser beam propagates;
- two seismically-isolated *test masses* (or mirrors) positioned at the extremities of each arm, whose thermal deformability must be compensated in order to avoid systematic effects;
- a photo-detector located at the exit point of the laser beam, which is re-built by the beam-splitter.

The laser beam, once recombined, can provide evidence to the passage of a gravitational wave in the form of a deformation of the distance over the length of the two arms (see section 1.2.3); such deformation is of the following order of magnitude:

$$\delta L \simeq 10^{-8} \left( \frac{h}{10^{-21}} \right) \left( \frac{L}{km} \right) m. \quad (1.46)$$

In order for the interferometer to detect such a small deformation, various techniques are implemented, one of which being the aforementioned Fabry-Perot cavity. Together with said device, seismic and thermal isolation are achieved in different ways depending on the detector at hand. For reference, a layout of the Virgo interferometer, is shown in Figure 1.1. When one considers the overall strain output of a detector, a noise component must be considered in the following form:

$$s(t) = n(t) + h(t), \quad (1.47)$$

where  $s(t)$  is the total output strain and  $n(t)$  is the additional noise component.

A detector's signal-to-noise ratio can be defined as follows:

$$SNR^2 = 4 \int_0^\infty \frac{|\tilde{h}(f)|^2}{S_n(f)} df, \quad (1.48)$$

where  $S_n$ , the *power spectral density* of the detector, is used as an indicator of the noise that affects the strain measurements.

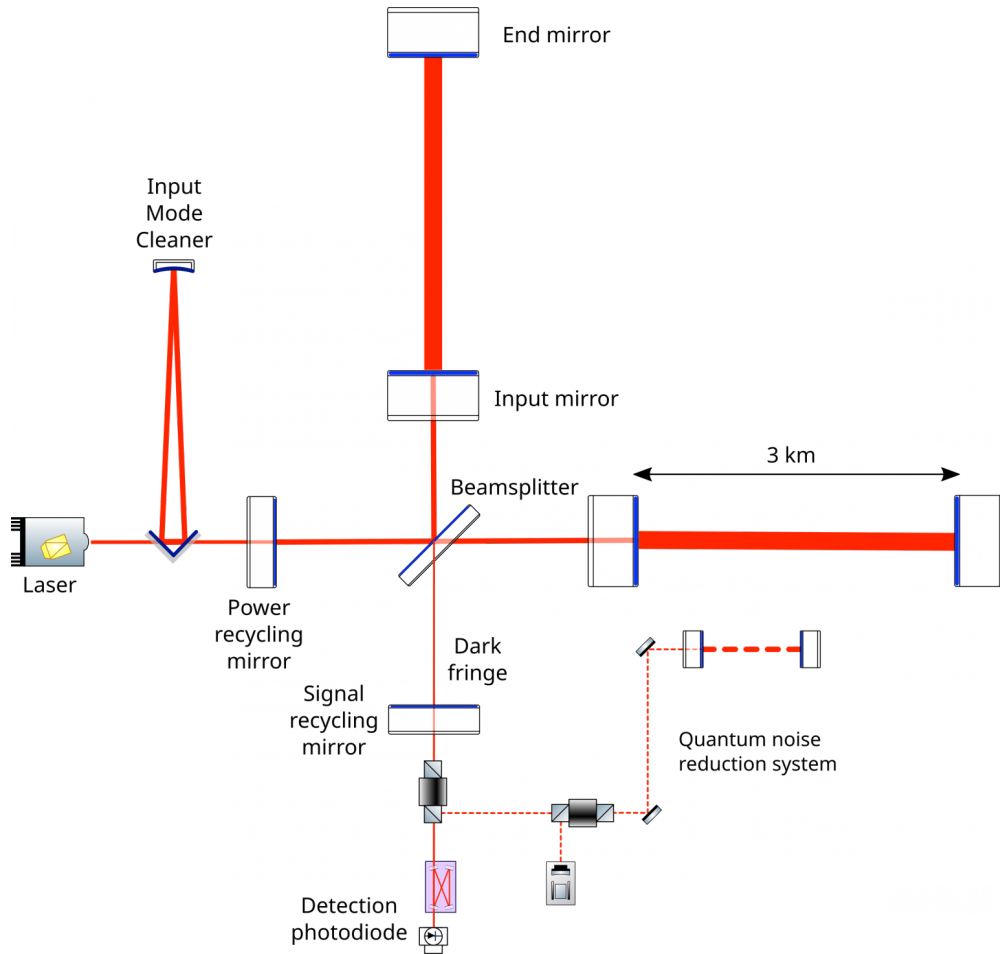


**Figure 1.1:** Optical layout of the Advanced VIRGO Gravitational Wave interferometer as of 2020 (Flaminio 2020). Together with the standard Michelson-Morley interferometer layout, the Advanced VIRGO configuration is equipped with additional components: the *Fabry-Perot cavity*, the *Input Mode Cleaner*, the *Power -Recycling Mirror*, the *Signal-Recycling Mirror* and various noise reduction systems.

## 1.5 Bayesian Inference

The relevance of Gravitational waves as cosmological probes is discussed in section 1.3. The theoretical framework that is often adopted to perform the necessary statistical inference of cosmological parameters starting from gravitational wave data is the *Hierarchical Bayesian Framework*. The usefulness of said approach has to be found not only in its predictive ability even when available data is scarce, but also in how it handles measurement uncertainties via likelihood marginalization (Loredo 2004). Apart from measurement uncertainties, an effective analysis must keep track of *selection biases*, which affect the probability of observing an object or event on the basis of how loud or luminous it is.

We start from a set of  $N_{ev}$  gravitational wave events described by a set of parameters:

$$\vec{\theta} = \{\mathcal{M}_c, \eta, d_L, \theta, \phi, \iota, \psi, t_c, \Phi_c, \chi_{1x}, \chi_{2x}, \chi_{1y}, \chi_{2y}, \chi_{1z}, \chi_{2z}, \Lambda_1, \Lambda_2\}, \quad (1.49)$$

where  $\mathcal{M}_c$  is the chirp mass of the event as measured in the detector's frame,  $\eta$  is the symmetric mass ratio of the two objects,  $d_L$  is the luminosity distance,  $\theta$  and  $\phi$  are the two angular coordinates that define the system's position in the sky,  $\iota$  is the angle between the normal to the system and the observer's line of sight,  $\psi$  is the polarization angle,  $\Phi_c$  is the phase of the gravitational wave at the time of coalescence  $t_c$ ,  $\chi_{ij}$  identifies the spin of object  $i = (1, 2)$  along the  $j = (x, y, z)$  directions and  $\Lambda_i$  is the tidal deformability of each of the two objects, null in the case of black holes (see Maggiore 2007).

For what concerns our analysis, we only focus on a set of these 17 parameters,  $d_L, \theta, \phi$  and  $\mathcal{M}_c$  in its two components  $m_1^{det}$  and  $m_2^{det}$ , while marginalizing over the others (which are assumed to have flat distributions).

The observed events are sampled from a population distribution  $p_{pop}(\theta|\lambda)$ , which depends on a set of *hyper-parameters*  $\lambda$ ; the total number density of the events in the selected  $\theta$  parameter space is related to the original distribution as (Mandel, Will M Farr, and Gair 2019)

$$\frac{dN}{d\theta}(\lambda) = N_{ev} p_{pop}(\theta|\lambda). \quad (1.50)$$

When sampling a certain number of observed events  $N_{obs}$  from the original population distribution we associate a *likelihood probability*  $\mathcal{L}(d_i|\theta_i)$  to each event  $i \in [1, N_{obs}]$  with measured data  $d_i$  and event parameters  $\theta_i$ ; this term describes how likely a measurement of some data is given a set of event parameters.

Assuming we are interested in the determination of the hyper-parameters  $\lambda$ , *Bayes' theorem* defines the relative *posterior probability* as follows:

$$p(\lambda|\{d_i\}) = \frac{\mathcal{L}(\{d_i\}|\lambda)\pi(\lambda)}{p(\{d_i\})}, \quad (1.51)$$

where  $\mathcal{L}(\{d_i\}|\lambda)$  represents the *hyper-likelihood probability*,  $\pi(\lambda)$  stands for the *prior probability* related to the population hyper-parameters and  $p(\{d_i\})$  is the integral of the hyper-likelihood probability over the  $\lambda$  parameter space. Since gravitational wave data is available, as in posterior samples relative to the different parameters that define a GW signal, we must find a way to relate the hyper-likelihood to the event-related posterior probability which, in the absence of any uncertainties, can be defined as follows:

$$p(\{\theta_i|\lambda\}) = \prod_{i=1}^{N_{ev}} \frac{p_{pop}(\theta_i|\lambda)}{\int p_{pop}(\theta'|\lambda) d\theta'}. \quad (1.52)$$

The event-related posterior on  $\theta$  must be updated when *detection probability*  $P_{det}(\theta)$  is taken into account. Said probability is equal to 1 for the observed event, but must be different when considering  $N_{ev}$ :

$$p(\{\theta_i\}|\lambda) = \prod_{i=1}^{N_{ev}} \frac{p_{pop}(\theta_i|\lambda)P_{det}(\theta_i)}{\int p_{pop}(\theta'|\lambda)P_{det}(\theta')d\theta'} \quad (1.53)$$

$$P_{det}(\theta) = \int_{d \in \text{Detectable data}} p(d'|\theta)dd'.$$

The hyper-likelihood probability can then be related to the event posterior:

$$\mathcal{L}(d_i|\lambda) = \frac{\int p(d_i|\theta')p_{pop}(\theta'|\lambda)d\theta'}{\int_{d \in \text{Det}} dd' \int p(d'|\theta')p_{pop}(\theta'|\lambda)d\theta'}; \quad (1.54)$$

equation 1.54 can then be inserted into equation 1.51 to obtain

$$p(\lambda|\{d_i\}) = \frac{\pi(\lambda)}{\xi(\lambda)^{N_{ev}}} \prod_{i=1}^{N_{ev}} \int p(d_i|\theta_i)p_{pop}(\theta_i|\lambda_i)d\theta_i \quad (1.55)$$

$$\xi(\lambda) := \int P_{det}(\theta')p_{pop}(\theta'|\lambda)d\theta',$$

where  $\xi_\lambda$  is an isolated term representing the *selection bias* related to the detectability of each event. This approach ignores the denominator in equation 1.51.

When *poissonian noise* is taken into consideration, equation 1.55 can be updated as follows:

$$p(\lambda, N_{ev}|\{d_i\}) = e^{-N_{exp}} (N_{exp})^{N_{ev}} \pi(N) \frac{\pi(\lambda)}{\xi(\lambda)^{N_{ev}}} \prod_{i=1}^{N_{ev}} \int p(d_i|\theta_i)p_{pop}(\theta_i|\lambda_i)d\theta_i \quad (1.56)$$

$$N_{exp} := N_{ev}\xi(\lambda).$$

This framework is used in the CHIMERA Python code and is discussed in Chapter 2.

## 1.6 Population Models

The population probability first presented in equation 1.52 describes the probability associated to a given GW event's parameters ( $\theta$ ) in relation to all the possible hyper-parameters  $\lambda$  that define the GW population.  $p_{pop}(\theta|\lambda)$  can be factorized in two separate components related to mass ( $m_1, m_2$ ) and localization ( $z, \hat{\Omega}$ ):

$$p_{pop}(\theta|\lambda) = p(m_1, m_2|\lambda_m)p(z, \hat{\Omega}|\lambda_c, \lambda_z), \quad (1.57)$$

where the hyper-parameter set was sub-divided in three components: *mass*-related  $\lambda_m$ , *redshift*  $\lambda_z$  and *cosmological*  $\lambda_c$  hyper-parameters. The first term of equation 1.57 defines the population's *mass model*, while the second defines the *rate* and *redshift distribution* models, grouped together in the *redshift prior* term. When it comes to the characterization of the mass model, prior considerations regarding the formation and evolution of binary systems must be made. Given that the most frequently observed ones are Binary Black Hole pairs, I briefly discuss the features found in the mass model adopted in this work. The mass spectrum of the components of BBH binaries is thought to be characterized by two main features: a cut-off at around  $5 M_\odot$ , which can be justified with various possible supernova mechanisms (such as neutrino-driven supernova explosions, Fryer

et al. 2012), and a peak at around  $30 - 40 M_{\odot}$  related to *pair-instability supernovae* (Talbot and Thrane 2018, Abbott, R. et al. 2021), which occur for stars with masses larger than  $100 M_{\odot}$ . These features are shown in this section through the example of the **POWER-LAW PLUS PEAK** model.

Referring back to equations 1.41, it is necessary to note that cosmological hyper-parameters enter the definition of redshift:  $z = z(d_L|\lambda_c)$ . For this reason, given that the available gravitational wave data is given in *detector frame*, the necessary cosmological conversion is affected by  $\lambda_c$ , more specifically  $m_{1,2} = \frac{m_{1,2}^{det}}{1+z(d_L|\lambda_c)}$ .

As for the two elements in equation 1.57, they can be analyzed separately:

- $p(m_1, m_2|\lambda_m)$  can be separated in two probabilities as

$$p(m_1, m_2|\lambda_m) = p(m_1|\lambda_m)p(m_2|m_1, \lambda_m), \quad (1.58)$$

where the first probability refers to the mass of the first object alone and the second describes a conditional  $m_2$  probability under the assumption that  $m_2 < m_1$ . Various models can be used to describe the two probabilities, such as **UNIFORM**, **TRUNCATED POWER-LAW**, **BROKEN POWER-LAW**, **POWER-LAW + PEAK** and **POWER-LAW + 2 PEAKS**. For the sake of the discussion that follows, only the first and last of this list are considered. More specifically, the **POWER-LAW + PEAK** model, described as

$$p(m_1|\alpha, \delta_m, m_{low}, m_{high}, \mu_g, \sigma_g, \lambda_g) \propto [(1 - \lambda_g) \mathcal{P}(m_1) + \lambda_g \mathcal{G}(m_1)] \mathcal{S}(m_1), \quad (1.59)$$

includes the contributions of a power-law distribution ( $\mathcal{P} = \mathcal{P}(m_1, \alpha)$ ) and a gaussian peak ( $\mathcal{G} = \mathcal{G}(m_1, \mu_g, \sigma_g)$ ) smoothed-out by the  $\mathcal{S} = \mathcal{S}(m_1, \delta_m)$  function; the contribution fraction of each is determined by  $\lambda_g$  and the overall probability is defined within a  $[m_{low}, m_{high}]$  interval. As for the mass of the second object, the probability associated to it is defined by means of the  $q = \frac{m_2}{m_1}$  ratio:

$$p(q|m_1, m_{low}, \beta) \propto q^\beta \mathcal{S}(q, m_1|m_{low}, \delta_m). \quad (1.60)$$

The **POWER-LAW + PEAK** distribution can be associated to the BBH population as it can accurately model said population's over-density at masses of  $M_{BH} \simeq 30 - 40 M_{\odot}$ , whereas a **UNIFORM** mass distribution can be associated to the binary neutron star population, for which information is still very scarce (Abbott, R. et al. 2023b).

- $p(z, \hat{\Omega}|\lambda_z, \lambda_c)$  can also be separated in multiple components:

$$p(z, \hat{\Omega}|\lambda_z, \lambda_c) = \frac{p_{gal}(z, \hat{\Omega}|\lambda_c)p_{rate}(z|\lambda_z)}{\int p_{gal}(z', \hat{\Omega}'|\lambda_c)p_{rate}(z'|\lambda_z)dz'd\hat{\Omega}'}, \quad (1.61)$$

where  $p_{gal}$  represents the probability of finding a galaxy at given redshift and sky localization and  $p_{rate}$  models the rate at which GW events happen as a function of redshift. This last term is particularly relevant on the account of its redshift dependency, highlighted by

$$p_{rate}(z|\lambda_z) \propto \frac{\psi(z|\lambda_z)}{1+z}, \quad (1.62)$$

which defines the relation between the detector-frame rate model ( $p_{rate}$ ) and the one in the source's frame ( $\psi$ ). This last term can, as for the mass models, be parametrized via different functions such as the **POWER-LAW** and the **MADAU-DICKINSON** (Madau and Dickinson 2014) models. For our purposes, the **MADAU-DICKINSON** model can be defined as

$$\psi(z|\lambda_z) \propto \frac{(1+z)^\gamma}{1 + \left(\frac{1+z}{1+z_{peak}}\right)^{\gamma+\kappa}}. \quad (1.63)$$

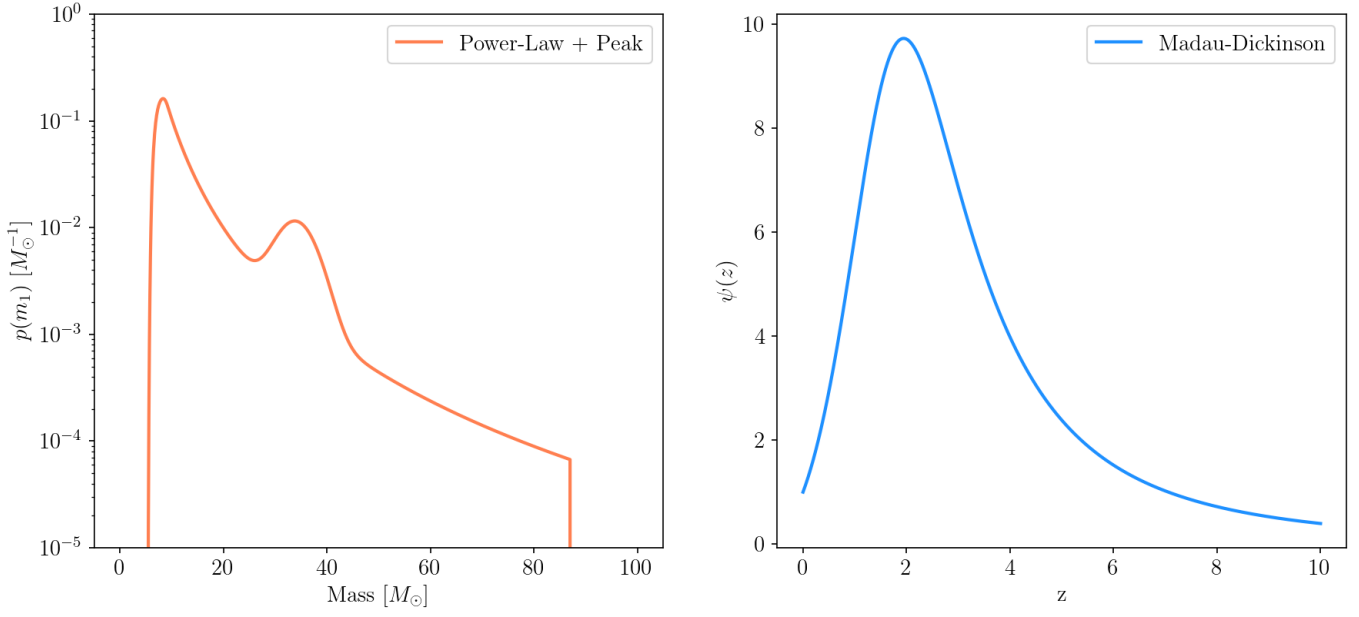


**Figure 1.2:** On the left, the POWER-LAW PLUS PEAK mass model computed for a mass range comprised between 0 and 100 solar masses. On the right, the MADAU DICKINSON CBC rate model computed on a redshift range comprised between 0 and 10.

Figure 1.2 features the two population models discussed above: the mass model is computed for the primary mass over a range defined as  $[0, 100] M_\odot$ , whereas the model itself is inherently limited between  $m_1 \in [5.1, 87] M_\odot$  which is a good choice for a given black hole population; the rate model, on the other hand, is computed over a redshift range defined between 0 and 10 as to show its full extent up to high redshift values.

## 1.7 Catalog Completeness

The use of a galaxy catalog is necessary when using a dark or spectral siren approach to associate redshift information to a given gravitational wave signal. In an ideal case, a galaxy catalog can be considered *complete*, which means that it can be thought to contain all galaxies along any given direction. In this case, where  $p_{cat}(z, \hat{\Omega}|\lambda_c)$  is the probability of finding a galaxy from the catalog at a given redshift and a given sky localization, we have the following:

$$p_{gal}(z, \hat{\Omega}|\lambda_c) = p_{cat}(z, \hat{\Omega}|\lambda_c) = \frac{\sum_g w_g p(z|d_g^{EM}, \lambda_c) \delta(\hat{\Omega} - \hat{\Omega}_g)}{\sum_g w_g} \quad (1.64)$$

$$p(z|d_g^{EM}, \lambda_c) = \frac{\mathcal{N}(z|\tilde{z}_g, \sigma_{z,g}^2) \frac{dV_c}{dz}(z|\lambda_c)}{\int \mathcal{N}(z'|\tilde{z}_g, \sigma_{z,g}^2) \frac{dV_c}{dz'}(z'|\lambda_c) dz'}$$

where  $p(z|d_g^{EM}, \lambda_c)$  represents a posterior related to the single  $g$  galaxy's redshift and is defined through Bayes' theorem with a gaussian likelihood ( $\mathcal{N}$ ) and a uniform in co-moving volume prior ( $\frac{dV_c}{dz}$ ).  $w_g$  stands for the weights associated with each galaxy, and  $\delta(\hat{\Omega} - \hat{\Omega}_g)$  is the galaxy's position prior.

In reality, a galaxy catalog will not contain all galaxies present within a given localization region  $\mathcal{S}(z, \hat{\Omega}; \Delta z, \Delta \hat{\Omega})$  with associated co-moving volume  $V_c$ ; catalog completeness must therefore be

accounted for, since  $p_{gal} \neq p_{cat}$ . Firstly, it is necessary to define completeness through the number density of *missed* galaxies  $n_{miss}$ :

$$\frac{1}{V_c(\mathcal{S})} \int_{\mathcal{S}} [n_{cat}(z, \hat{\Omega}) + n_{miss}(z, \hat{\Omega})] dV_c = \overline{n_{gal}}. \quad (1.65)$$

Equation 1.65 defines the expected average number density of galaxies,  $\overline{n_{gal}}$ , in relation to the number density of the galaxies found within the catalog ( $n_{cat}$ ) and those that are not ( $n_{miss}$ ). One can then define the *completeness probability* or  $P_{compl}$  as follows:

$$P_{compl} = \frac{N_{cat}(\mathcal{S})}{\overline{n_{gal}} V_c(\mathcal{S})}, \quad (1.66)$$

where  $N_{cat}$  is the total number of galaxies in the catalog.

The definition given in equation 1.66 only accounts for the expected number density of objects in a given region, which means that galaxies are not weighed in any way ( $w_g$ ); said definition can be updated if one considers *luminosity* as a completeness criterion: in this case,  $w_g$  takes the values of each galaxy's luminosity. Equation 1.66 can then be updated as follows:

$$P_{compl} = \frac{L_{tot}(L_g > L_{thr}, \mathcal{S})}{\overline{l_{gal}} V_c}; \quad (1.67)$$

$L_{tot}(L_g > L_{thr}, \mathcal{S})$  in equation 1.67 is the total luminosity of the catalog in the  $\mathcal{S}$  region for the galaxies whose luminosities cross a threshold value equal to  $L_{thr}$ , whereas  $\overline{l_{gal}}$  is the average expected luminosity per co-moving volume; the latter value, assuming the law that best describes the galaxies' luminosities is a Schechter function in the shape of

$$\Phi(L)dL = \Phi^* \left( \frac{L}{L^*} \right)^\alpha e^{-\frac{L}{L^*}} d \left( \frac{L}{L^*} \right) \quad (1.68)$$

where  $L^*$  identifies the *knee* of the distribution,  $\overline{l_{gal}}$  is given by

$$\overline{l_{gal}} = \Phi^* L^* \Gamma \left( \alpha + 2, \frac{L}{L^*} \right), \quad (1.69)$$

where all values marked with \* correspond to the distribution's knee and  $\Gamma$  is the incomplete Gamma function.

How  $P_{compl}$  comes into the composition of the likelihood is given by the redshift prior term, more specifically the  $p_{gal}$  term which appears in equation 1.64, which can now be seen as a sum of two terms:

$$p_{gal}(z, \hat{\Omega} | \lambda_c) = f_{\mathcal{R}} p_{cat}(z, \hat{\Omega} | \lambda_c) + (1 - f_{\mathcal{R}}) p_{miss}(z, \hat{\Omega} | \lambda_c); \quad (1.70)$$

the term  $f_{\mathcal{R}}$  represents the *completeness fraction* of the catalog, which is defined as

$$f_{\mathcal{R}} := \frac{1}{V_c(\lambda_c)} \int P_{compl}(z, \hat{\Omega}) dV_c \quad (1.71)$$

where the integral is performed over the largest possible comoving volume in which GW events can be observed. The  $p_{miss}$  term, on the other hand, aims to describe the distribution of those galaxies that are missing from the catalog; in the presence of a largely incomplete catalog, it can be assumed that galaxies are distributed uniformly in comoving volume and, as such,

$$p_{miss}(z, \hat{\Omega} | \lambda_c) = \frac{1 - P_{compl}(z, \hat{\Omega})}{(1 - f_{\mathcal{R}}) V_c} \frac{dV_c}{dz}(z | \lambda_c). \quad (1.72)$$

# Chapter 2

## Data and Methods

What follows in this Chapter is a description of the data sets and the Hierarchical Bayesian inference method at the core of my work, together with the methodological enhancements I developed and implemented in the analysis pipeline.

The Chapter begins with a description of the galaxy and gravitational wave datasets, starting from the GWTC-3 catalog and the selection criteria used to extract a sample of 47 events to perform analyses on, followed up by the GLADE+ galaxy catalog, the sub-catalogs that were used to build it, its sky coverage, and the redshift uncertainties.

The Chapter then provides an introduction to the original framework of the CHIMERA code and the main components that are computed in its workflow: the GW kernel, the galaxy catalog redshift and sky position, and the selection effects term.

After that, I describe the updates I applied to the current pipeline to carry out hierarchical Bayesian inference on sets of real gravitational wave and galaxy data in an effort to produce this type of analysis with a code that is independent of the LVK Collaboration. The major changes I applied to the different modules of CHIMERA are discussed, more specifically, the completeness correction and the selection bias term.

### 2.1 The GWTC-3 Catalog

Our gravitational wave dataset is extracted from the **Gravitational Wave Transient Catalog 3 (GWTC-3)** (Abbott, R. et al. 2023a, Abbott, R. et al. 2023b), compiled by the LIGO Scientific, Virgo and KAGRA Collaborations through the end of the third observing run (O3). It contains data related to three different classes of binary merger events: Binary Black Holes (BBH), Binary Neutron Stars (BNS) and Black Hole Neutron Star binaries (BHNS).

In particular, it consists of 90 events selected on the basis of the inferred probability of a signal having astrophysical origins as opposed to being a result of instrumental noise,  $p_{astro} > 0.5$ . This probability estimate is extracted from noisy data using a Bayesian approach, for which assumptions about the stochastic background and the foreground signals are made (Will M. Farr et al. 2015).

#### 2.1.1 Selection criteria

The first step in producing cosmological parameter inference through real gravitational wave data is to analyze it.

Gravitational wave data from LVK are organized in HDF5-format files with a dictionary-like structure: each key corresponds to a parameter (for example, luminosity distance, primary and secondary mass) and is linked to a 2-D table containing posterior samples for each gravitational wave event. The posterior samples are obtained with a variety of different waveforms that are

used to model the GW signal, such as IMRPhenomD or IMRPhenomXPHM. GW posteriors are also released with different prior choices: for instance, a  $d_L^2$  prior can be applied to the luminosity distance samples to account for the cosmological volume effect. Our analysis, however, makes use of prior-free GW event samples.

The events featured in Abbott, R. et al. 2023a are 90 in total, of which 47 are selected on the basis of their Signal-to-Noise Ratio (SNR) and False Alarm Rate (FAR): only those events whose SNR is equal or higher than 11 and FAR is lower than  $\frac{1}{4} \text{ yr}^{-1}$  are used in Abbott, R. et al. 2023a's cosmological analysis. 42 out of said 47 events are classified as BBHs, while the remaining 5 are either Binary Neutron Stars (2) or Neutron Star-Black Hole Binaries (3). As for the events up to the third Observing Run of LVK, I use the second version of said data<sup>1,2</sup>.

In this work, I use the same sample of events adopted in Abbott, R. et al. 2023a to allow for a comparison with previous analyses. Figure 2.1 presents the mean and standard deviation of the primary and secondary masses, and the luminosity distance values of the 42 BBHs, while the posteriors of each event are shown in Figure 2.2. The mean luminosity distance for this sample is  $\approx 1.5 \text{ Gpc}$  with a standard deviation of around  $1.2 \text{ Gpc}$ ; the average primary mass is  $\approx 45 \pm 30 M_\odot$ , whereas for the secondary mass samples we have  $\approx 30 \pm 21 M_\odot$ . Figure 2.3 shows the localization areas of the BBH events (plotted with `GW_stats`, section 2.4) separated in groups of six; together with the plots, I extract relevant information relative to the 47 events (both BBH and non-BBH), which is presented in Table 2.1. The average pixel localization area relative to the events that belong to the sample of BBH events alone is around  $\approx 700 \text{ deg}^2$ , with some (such as GW200311\_115853) being localized in much smaller areas of the order of  $\approx 100 \text{ deg}^2$ ; the actual localization areas at different confidence levels are likely to be smaller, since those found in 2.1 are computed considering all possible localization pixels.

The BBH sample's redshift distribution is also shown in Figure 2.4, where  $H_0$  is assumed to be equal to  $70 \text{ km/s/Mpc}$  in order to translate the luminosity distance information into redshift. The mean of this distribution is at  $z \approx 0.2$ , but some samples extend out to values similar to 1.4.

As for the non-BBH events, namely GW170817, GW190425, GW190814, GW200105\_162426 and GW200115\_042309, the first two represent cases of Binary Neutron Star events, while the latter three are classifiable as Black Hole-Neutron Star binaries. GW170817 and GW190814, in particular, are discussed in more detail in Chapter 3.

When applying the same criteria adopted by Abbott, R. et al. 2023a on the second version of the GW files, I encountered some differences in terms of our selection: this is probably due to the SNR value assigned to each event being modified and revised in newer versions of the event files; notice how the SNR values for two events in Table 2.1, GW190517\_055101 and GW200202\_154313, are lower than 11. In Appendix A, I show the same set of plots for this different data set (Figures A.1 and A.2). To ensure a more fair comparison I proceed with the same set of events as in Abbott, R. et al. 2023a, for which the selection cut adopted and referenced throughout the Thesis refers to the first version of the catalog.

<sup>1</sup>LIGO Scientific Collaboration and Virgo Collaboration. (2022). GWTC-2.1: Deep Extended Catalog of Compact Binary Coalescences Observed by LIGO and Virgo During the First Half of the Third Observing Run - Parameter Estimation Data Release (Version v2) [Data set]. Zenodo. <https://doi.org/10.5281/zenodo.6513631>

<sup>2</sup>LIGO Scientific Collaboration and Virgo Collaboration and KAGRA Collaboration. (2023). GWTC-3: Compact Binary Coalescences Observed by LIGO and Virgo During the Second Part of the Third Observing Run — Parameter estimation data release [Data set]. Zenodo. <https://doi.org/10.5281/zenodo.8177023>

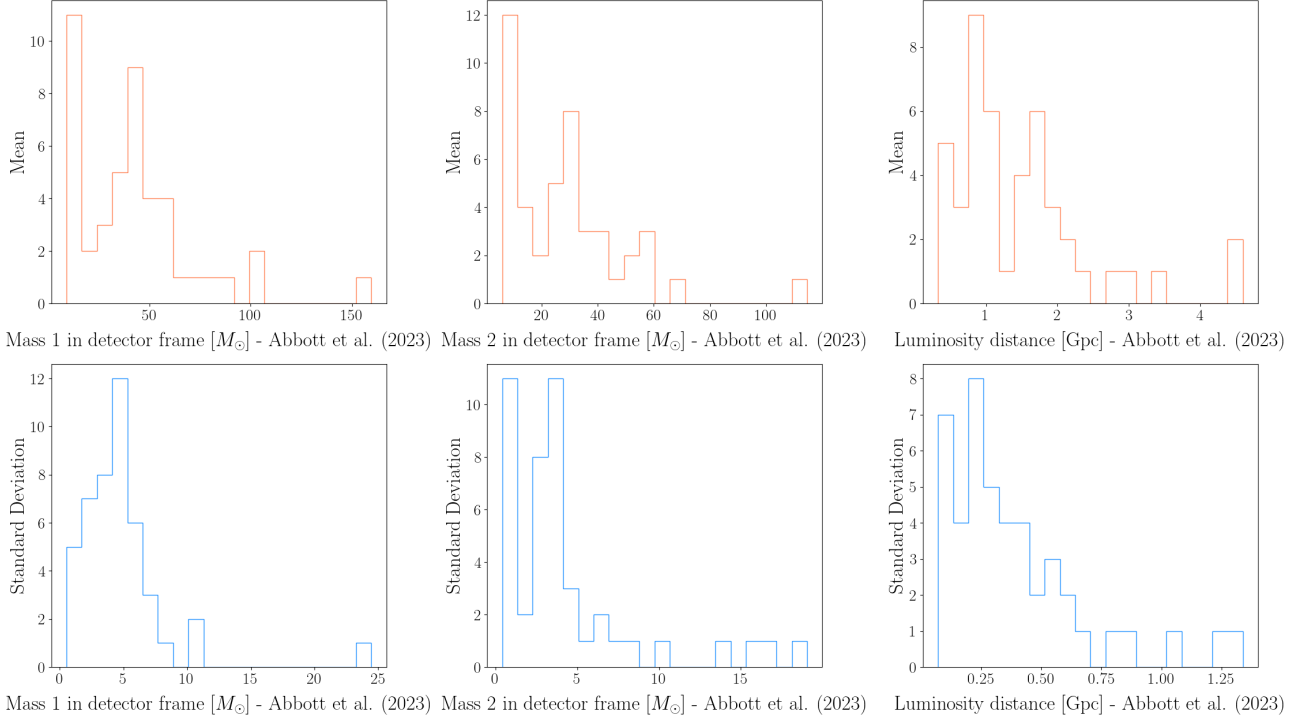


**Figure 2.1:** Properties of 42 BBHs from GWTC-3 selected with a criterion of  $\text{SNR} > 11$  and  $\text{FAR} < \frac{1}{4} \text{ yr}^{-1}$  (as in Abbott, R. et al. 2023a) for the values of luminosity distance  $d_L$ , mass of the primary object  $m_1$ , mass of the secondary object  $m_2$  (first row) and standard deviation (second row).

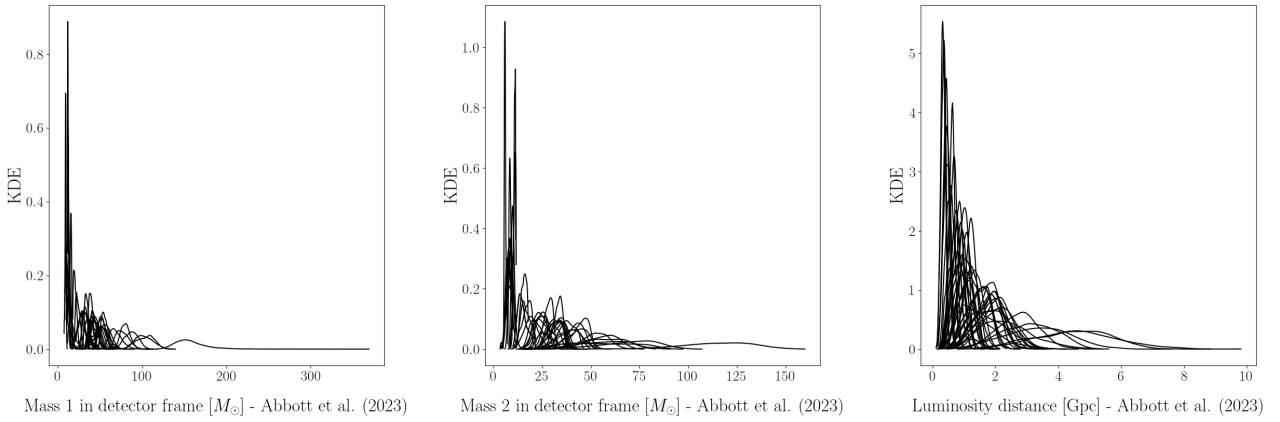


**Figure 2.2:** Posteriors of 42 BBHs from GWTC-3 selected with a criterion of  $\text{SNR} > 11$  and  $\text{FAR} < \frac{1}{4} \text{ yr}^{-1}$  (as in Abbott, R. et al. 2023a) for the values of luminosity distance  $d_L$ , mass of the primary object  $m_1$  and mass of the secondary object  $m_2$ .

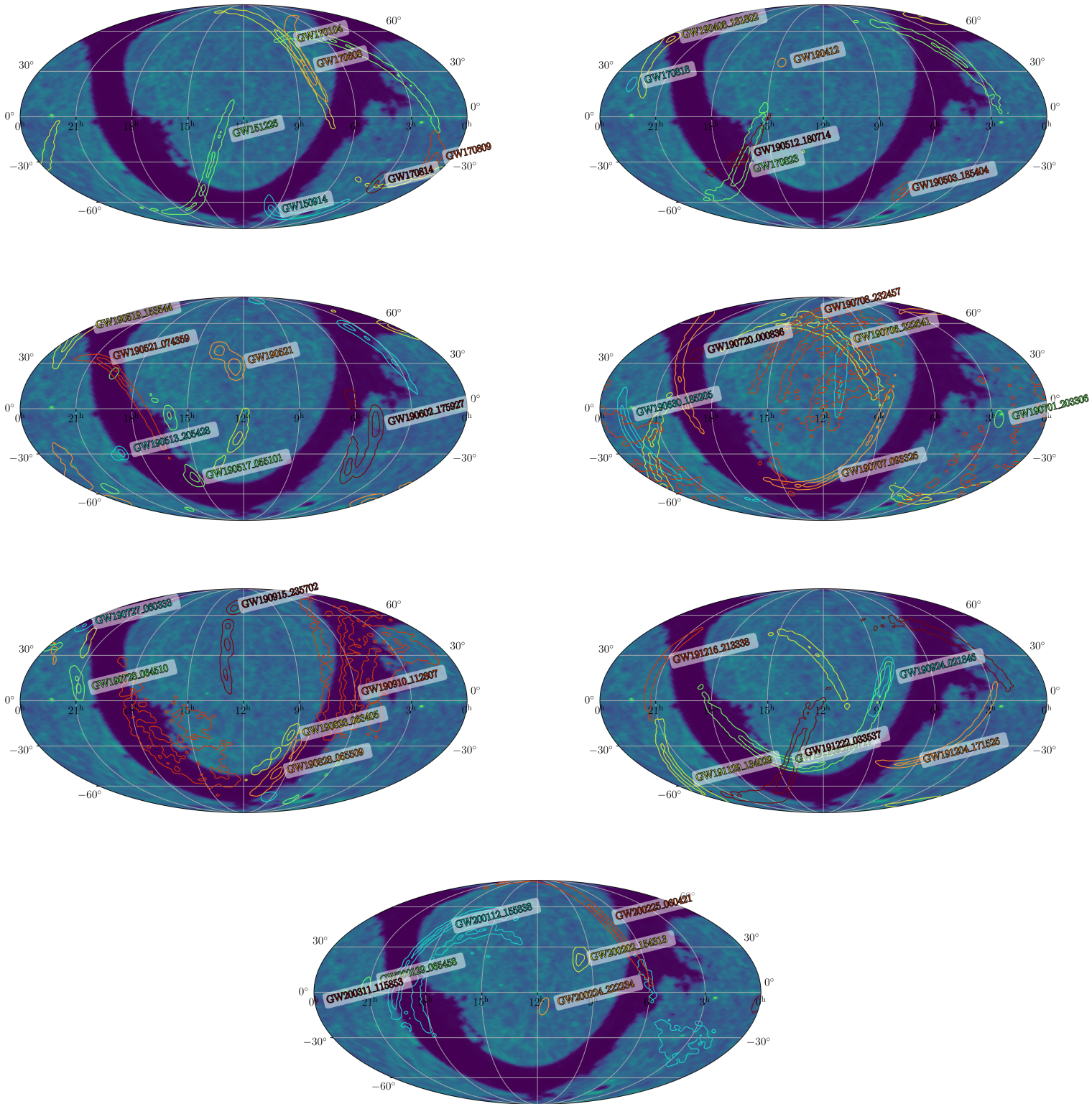


**Figure 2.3:** Localization areas (at 50% and 90% cumulative probability) of 42 BBHs from GWTC-3 selected with  $\text{SNR} > 11$  and  $\text{FAR} < \frac{1}{4} \text{ yr}^{-1}$  (as in Abbott, R. et al. 2023a). On the background of each map is a 2-D histogram that assigns a different color to each pixel on the basis of its galaxy number density as extracted from the GLADE+ galaxy catalog (section 2.2). The plots are created using GW\_stats (section 2.4)

**Table 2.1.** Properties of 47 GWTC-3 events selected in Abbott, R. et al. 2023a with  $\text{SNR} > 11$  and  $\text{FAR} < \frac{1}{4} \text{ yr}^{-1}$  and analyzed with `GW_stats` (see section 2.4). In bold, the events that are not classified as BBHs. Columns from left to right: event name, galaxy count within the given redshift uncertainty ranges,  $3\sigma$  lower and upper redshift boundaries, localization area, and SNR from the second version of the catalog.

Event	$\sigma_z < 1.5 \times 10^{-4}$	$\sigma_z > 1.5 \times 10^{-2}$	$1.5 \cdot 10^{-4} < \sigma_z < 1.5 \cdot 10^{-2}$	Minimum Redshift ( $3\sigma$ )	Maximum Redshift ( $3\sigma$ )	Area [ $\text{deg}^2$ ]	SNR
GW150914	20	82557	4166	0.034	0.164	329.003	26.0
GW170814	42	66891	6219	0.06	0.202	228.288	17.7
GW170809	110	270093	14067	0.086	0.339	473.362	12.8
GW151226	213	219704	16377	0.026	0.175	1075.974	13.1
GW170104	191	543095	16077	0.046	0.359	900.562	13.8
GW170818	8	64397	2346	0.075	0.365	124.215	12.0
GW170823	197	567117	22748	0.066	0.65	1336.995	12.2
GW170608	93	64688	6275	0.028	0.123	525.398	15.4
GW190701_203306	29	80950	3291	0.148	0.618	125.894	11.2
GW190720_000836	49	165169	6950	0.013	0.307	343.271	10.9
GW190708_232457	329	1152784	36217	0.032	0.312	1948.001	13.4
GW190503_185404	18	146699	1643	0.096	0.492	210.663	12.2
GW190924_021846	48	168836	6524	0.034	0.209	485.951	12.0
GW190828_065509	23	203815	5189	0.096	0.56	698.292	10.2
GW190706_222641	232	524025	18641	0.165	1.236	805.722	13.4
GW190408_181802	24	181666	6104	0.089	0.474	407.897	14.6
GW190915_235702	78	316751	7526	0.123	0.558	492.665	13.1
GW190728_064510	37	349020	7969	0.06	0.304	551.416	13.1
GW190727_060333	25	192753	3213	0.184	0.793	467.487	11.7
GW190707_093326	48	237371	6322	0.025	0.295	1082.689	13.1
GW190828_063405	27	215895	5120	0.131	0.55	483.433	16.5
GW190602_175927	122	452033	12968	0.0	0.819	786.418	13.2
GW190521	306	604234	22456	0.131	1.323	894.687	14.3
GW190521_074359	174	103039	7198	0.077	0.388	563.166	25.9
GW190910_112807	252	630859	20753	0.08	0.618	2063.823	14.5
GW190519_153544	56	398311	9802	0.13	0.919	705.846	15.9
GW190412	62	107264	3059	0.051	0.28	193.038	19.8
GW190512_180714	107	172489	4190	0.083	0.486	430.558	12.7
GW190630_185205	286	530517	22102	0.031	0.349	908.116	16.4
GW190513_205428	105	179626	9556	0.114	0.588	464.969	12.5
GW191222_033537	232	658736	19335	0.053	1.04	1281.601	12.5
GW200112_155838	319	660307	24517	0.112	0.413	1454.496	19.8
GW191216_213338	51	46215	5041	0.03	0.127	378.521	18.6
GW191204_171526	75	129394	6124	0.065	0.215	434.754	17.5
GW190517_055101	163	444358	10683	0.0	6.495	913.151	10.8
GW200202_154313	60	263203	6825	0.0	6.495	396.147	10.8
GW200225_060421	80	324158	6376	0.057	0.41	642.899	12.5
GW200311_115853	8	46389	2109	0.135	0.356	89.804	17.8
GW200224_222234	10	90824	2460	0.158	0.52	125.055	20.0
GW200129_065458	24	53786	2044	0.105	0.302	101.555	26.8
GW191129_134029	145	490290	19091	0.067	0.272	848.526	13.1
GW191109_010717	189	513357	10052	0.0	0.609	1187.601	17.3
<b>GW190814</b>	12	2537	1376	0.034	0.07	104.072	25.3
<b>GW190425</b>	675	98759	30544	0.006	0.064	5005.547	12.5
<b>GW200105_162426</b>	683	368254	59214	0.014	0.105	5270.764	13.9
<b>GW200115_042309</b>	183	60159	12997	0.021	0.109	990.367	11.3
<b>GW170817</b>	0	2	18	0.005	0.013	3.357	33.0

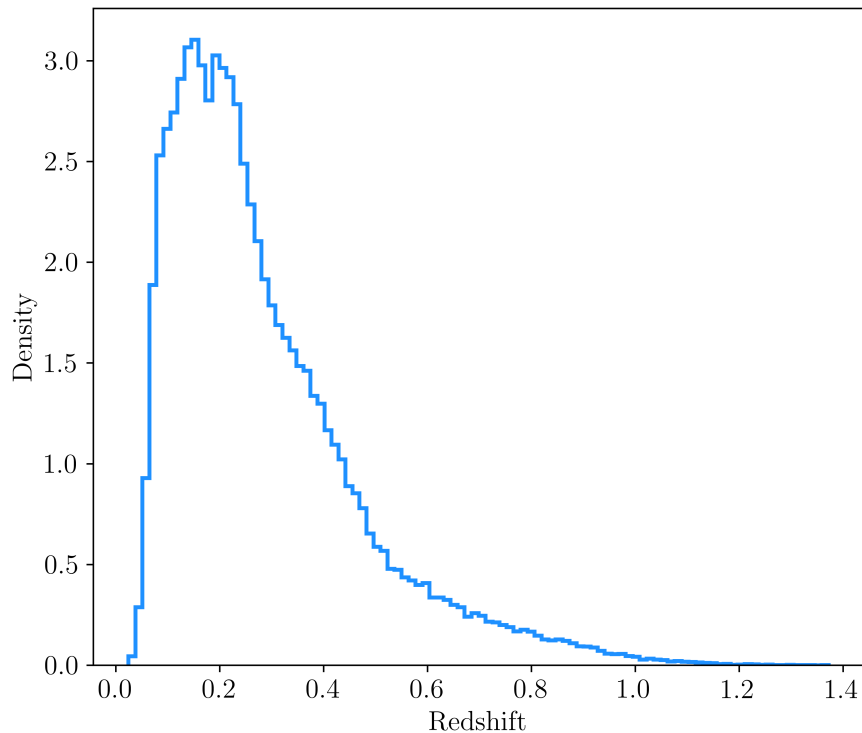


**Figure 2.4:** Redshift distribution of the posterior samples of 42 BBH events selected in Abbott, R. et al. 2023a. The redshift values are obtained by assuming  $H_0 = 70 \text{ km/s/Mpc}$ .

## 2.2 The GLADE+ Galaxy Catalog

The dark siren approach is based on the use of a galaxy catalog (as discussed in Section 1.7). We adopt the second version of the **Galaxy List for the Advanced Detector Era (GLADE+)**, released in 2022 (Dályá, G. et al. 2022), which is a combination of the following subcatalogs:

- the **Gravitational Wave Galaxy Catalog (GWGC)** (White, D. J. et al. 2011);
- the **HyperLEDA** galaxy catalog (Makarov et al. 2014);
- the **2 Micron All-Sky Survey Extended Source Catalog (2 MASS XSC)** (Jarrett et al. 2000);
- the **2 MASS Photometric Redshift Catalog (2MPZ)** (Bilicki et al. 2013);
- the **WISEXSCOS Photometric Redshift Catalog (WISEXSCOSPZ)** (Bilicki, M. et al. 2016);
- the **Sloan Digital Sky Survey - 16th data release (SDSS-DR16Q)** (Lyke, B. W. et al. 2020).

The first four catalogs were already part of the previous version of GLADE (Dályá, G. et al. 2018), while the latter two are the most recent additions to it with the SDSS-DR16Q catalog taking the place of SDSS-DR12Q (Pâris, I. et al. 2017).

## 2.2.1 The Sub-Catalogs

What follows is a brief description of the six catalogs mentioned above and their properties. In general, the main differences between the various sub-catalogs come down to the number of galaxies, their sky coverage (which determines differences in galaxy number density and becomes relevant in the computation of the catalog completeness term, section 1.7), and the galaxy redshift errors.

### The Gravitational Wave Galaxy Catalog (GWGC)

The predecessor to GLADE and GLADE+, the Gravitational Wave Galaxy Catalog (GWGC) contains  $\sim 50\,000$  galaxies and  $\sim 150$  globular clusters as a result of the combination of three existing catalogs:

- the **Tully Nearby Galaxy Catalog** (Tully 1987);
- the **Catalog of Neighboring Galaxies** (Karachentsev et al. 2004);
- the **V8k catalog** (Tully et al. 2009).

Supplemental data for certain objects was derived from the HyperLEDA catalog.

GWGC extends out to a maximum luminosity distance of  $\simeq 100$  *Mpc* and contains luminosity distance data (with measurement errors between 10 and 20 percent) and B-band magnitude data (with average error  $\Delta B = 0.37^m$ ) for each object; the latter was not reliable and had to be corrected using the **VizieR** database (Ochsenbein, F. et al. 2000).

### The HyperLEDA galaxy catalog

HyperLEDA contains over 3 000 000 objects obtained by merging the **LEDA** (Paturel, G. et al. 1988) and the **Hypercat** (Prugniel, Ph. et al. 1999) databases; out of the total number of objects,  $\sim 2\,600\,000$  were kept, corresponding to the number of galaxy objects. Luminosity distances from spectroscopic redshift measurements are given with a 36 percent mean error.

### 2MASS XSC

The 2MASS XSC catalog consists of  $\sim 1\,600\,000$  objects and their respective photometric magnitudes; all objects were kept for analysis despite some being classifiable as stellar in nature: this was possible given that the stellar contamination is thought to be minimal. The catalog does not contain B magnitude nor redshift data.

### The 2MPZ galaxy catalog

2MPZ is the result of the cross-match of two different catalogs:

- the **Wide-field Infrared Survey Explorer** catalog (Wright, E. L. et al. 2010);
- the **SuperCOSMOS** optical catalog (Hambly, N.C. et al. 2001).

For the objects which are presented with photometric redshift data, the relative errors are independent of distance and have an all-sky average of  $\Delta z = 1.5 \cdot 10^{-2}$ ; as for the spectroscopic redshift data (provided for approximately 300 000 entries out of 900 000) the average error is  $\Delta z = 1.5 \cdot 10^{-4}$ .

### The WISExSCOS Photometric Redshift Catalog (WISExSCOSPZ)

WISExSCOSPZ is the result of a cross-match between the **AllWISE** (Cutri, R.M. et al. 2021) full-sky release of **WISE** (Wright, E. L. et al. 2010) and the **SuperCOSMOS Sky Survey** (Hambly, N.C. et al. 2001). It contains around 20 000 000 galaxies, making it the most populated out of all the sub-catalogs. Each object contained in it features photometric redshifts and relative errors; the latter are independent of distance and have an overall accuracy of  $\approx 0.033 \times (1 + z)$ .

### The SDSS-DR16Q quasar catalog

SDSS-DR16Q contains the photometric redshift information relative to around 750 000 spectroscopically targeted and visually confirmed quasars; these include the 300 000 objects present in SDSS-DR12Q, which was used in the creation of GLADE.

### 2.2.2 The construction of GLADE+

The first version of GLADE was constructed using the cross-match of GWGC, 2MPZ, 2MASS XSC, HyperLEDA, and SDSS-DR12Q. More specifically, GWGC and HyperLEDA were initially cross-matched separately on the basis of object names, which were the same in both catalogs and therefore allowed for a direct comparison and removal of any duplicates (the same was done for 2MASS XSC and 2MPZ). The resulting catalogs were then cross-matched using the objects' RA, Dec, B magnitude, and luminosity distance values following a chi-square approach. SDSS-DR12Q was then added to the final result, as no matches were present.

In order to create GLADE+, GLADE was further cross-matched with the WISExSCOSPZ catalogue, and SDSS-DR12Q was substituted with the more extended SDSS-DR16Q.

To better understand the composition of GLADE+, Figure 2.5 shows the sky distribution of a sub-sample of the full GLADE+ catalog extracted via CosmoHUB (Tallada et al. 2020, Carretero et al. 2017); these 89852 randomly selected sources are colored according to the catalog they belong to. Given that a single source can be present in multiple catalogs, the less populated catalogs occupy the forefront layers of the plot to make their presence more visible.

GLADE+ contains 23 181 758 objects, 22 431 348 of which are galaxies and 750 410 are quasars.

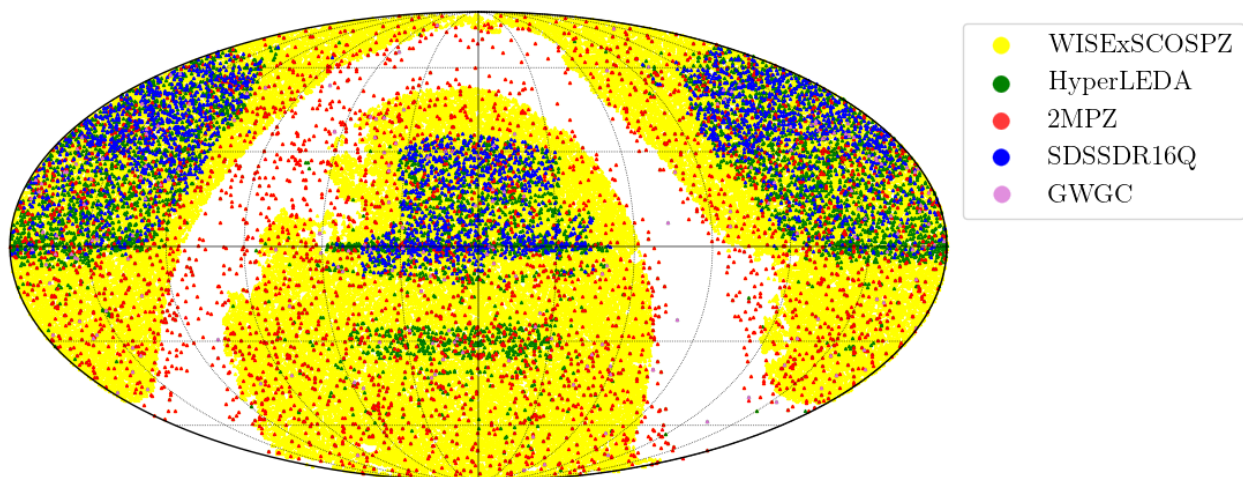


**Figure 2.5:** Right ascension (RA) and declination (Dec) distribution of the 89853 sources extracted randomly from GLADE+ using CosmoHUB (Tallada et al. 2020, Carretero et al. 2017); the sources are colored according to the catalog they appear in: yellow stands for WISEXSCOSPZ, green stands for HyperLEDA, red stands for 2MASS XSC, blue stands for SDSSDR16Q and pink stands for GWGC. Sources belonging to multiple catalogs are assigned to the more populated one.

### 2.2.3 Redshift and redshift errors in GLADE+

One of the main areas of interest when it comes to characterizing the catalog is the method used to assign an uncertainty to specific values. In particular, the errors associated to the redshift values contained in GLADE+ vary depending on the sub-catalog they were originally found in.

Refer to Figure 2.6 for a 1-D redshift distribution of the galaxies in the GLADE+ catalog; together with it, an interpolant computed on the same distribution can be seen (orange line). It is apparent from Figure 2.6 how GLADE+ is limited to low redshift values: this becomes relevant in the analysis performed in Chapter 3.

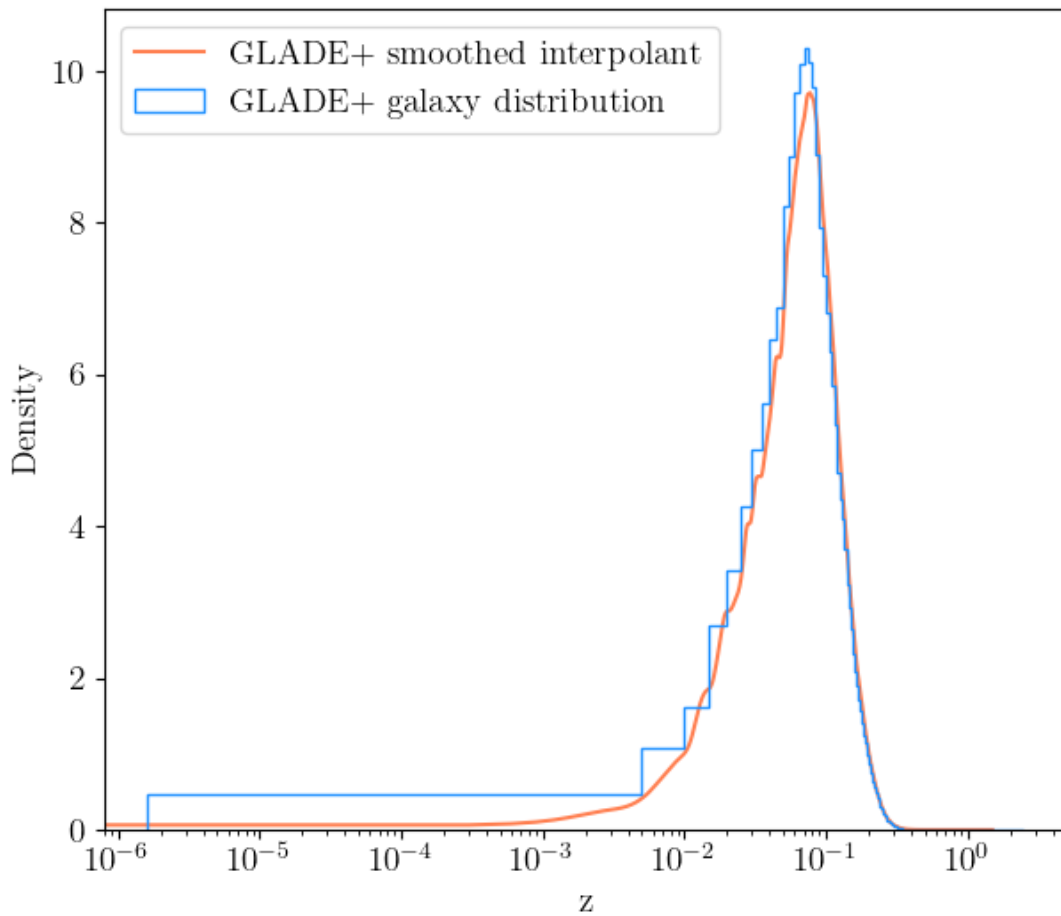


**Figure 2.6:** GLADE+ redshift distribution (histogram in blue); superimposed on it, the smoothed interpolant computed on the same distribution (in orange). The x-axis, representing the redshift values, is shown in  $\log_{10}$  scale.

What follows in Figure 2.7 is a representation of the galaxies' redshift densities (x-axis) with respect to their error (y-axis); the galaxy data is displayed in a 2D histogram on the basis of the galaxies' right ascensions and declinations with a  $300 \times 300$  RA, Dec resolution. In particular, from Figure 2.7 (bottom) one can notice how the errors (y-axis) follow starkly different trends, which could in principle lead back to the capabilities of the instruments used in each catalog, as well as the assumption made to construct them (some of these trends were already presented in sub-section 2.2.1). The plot in Figure 2.7 (top) is separated in three areas based on the assumption that redshift uncertainties higher than  $1.5 \cdot 10^{-2}$  correspond to *photometric measurements*, whereas errors lower than  $1.5 \cdot 10^{-4}$  are indicative of *spectroscopic measurements*. The values comprised between these two levels are assumed to have been assigned post-measurement following one of the diagonal trends displayed in Figure 2.7 (bottom).

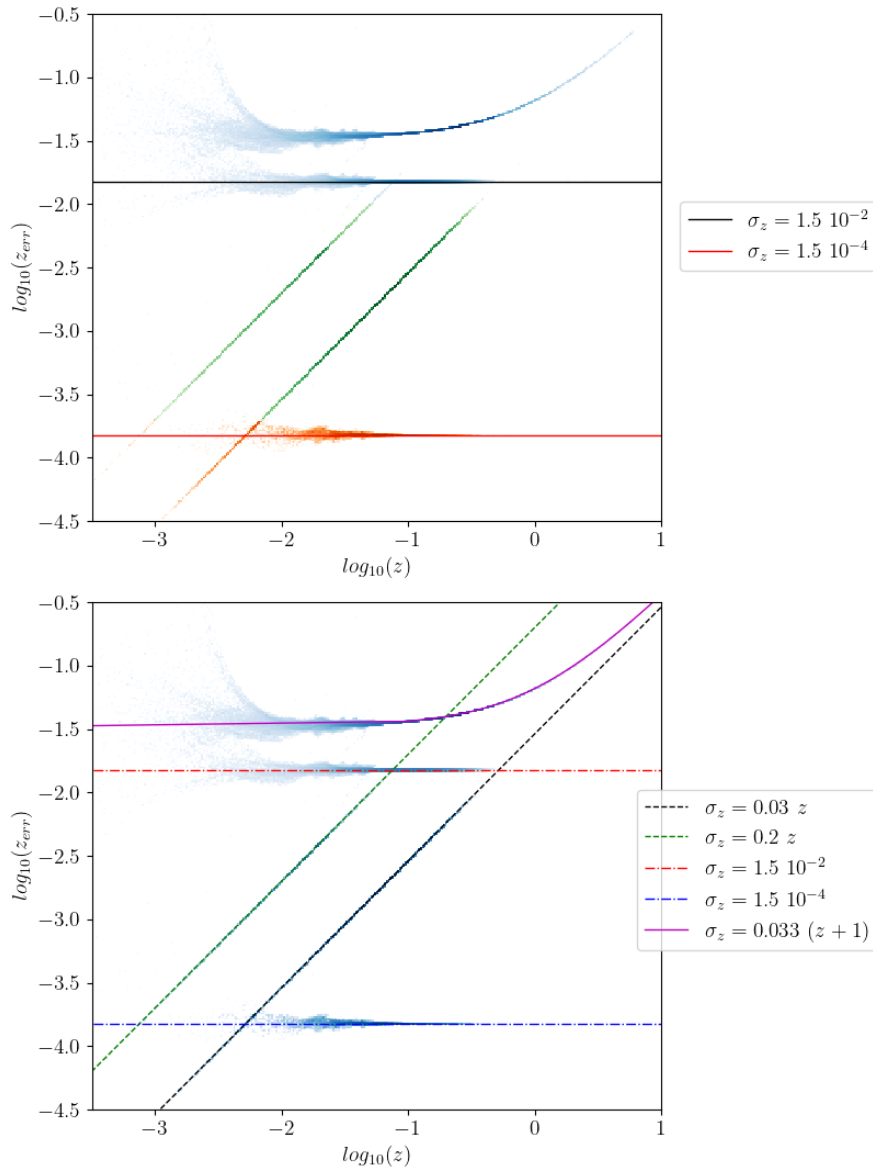


**Figure 2.7:** On top, the redshift distribution of the galaxies in GLADE+ (x axis, in  $\log_{10}$ ) compared to the relative uncertainties (y axis, in  $\log_{10}$ ) with a  $300 \times 300$  RA-Dec resolution; the distribution is separated in three areas: spectroscopic redshifts ( $\sigma_z < 1.5 \cdot 10^{-4}$ ), photometric redshifts ( $\sigma_z > 1.5 \cdot 10^{-2}$ ) and the remaining measurements in between. On the bottom, five trends in redshift values ( $z$ ) in relation to their respective uncertainties  $\sigma_z$ :  $\sigma_z = 0.03 z$ ,  $\sigma_z = 0.2 z$ ,  $\sigma_z = 1.5 \cdot 10^{-2}$ ,  $\sigma_z = 1.5 \cdot 10^{-4}$  and  $\sigma_z = 0.033 (z + 1)$  shown as logarithms both on the x-axis and the y-axis.

### GLADE+ sky maps

In an effort to better quantify the distribution of galaxies in the GLADE+ catalog, as well as the GW events, I make use of the `healpy` (Zonca et al. 2019, Górski et al. 2005) package, based on the `HEALPix3` library; with a combination of the functions it provides it is possible to build a pixel map starting from an `nside` parameter, which defines the number of pixels per pixel side. Different statistics, like object count or average redshift values, can then be cast on the pixels of the map. Two examples of the application of these functions to the galaxies contained in GLADE+ are displayed in Figure 2.8 (a galaxy count map on top and an average redshift value map on the bottom); the `nside` parameter used to build them (and every other `healpy` map in this Chapter) is 64.

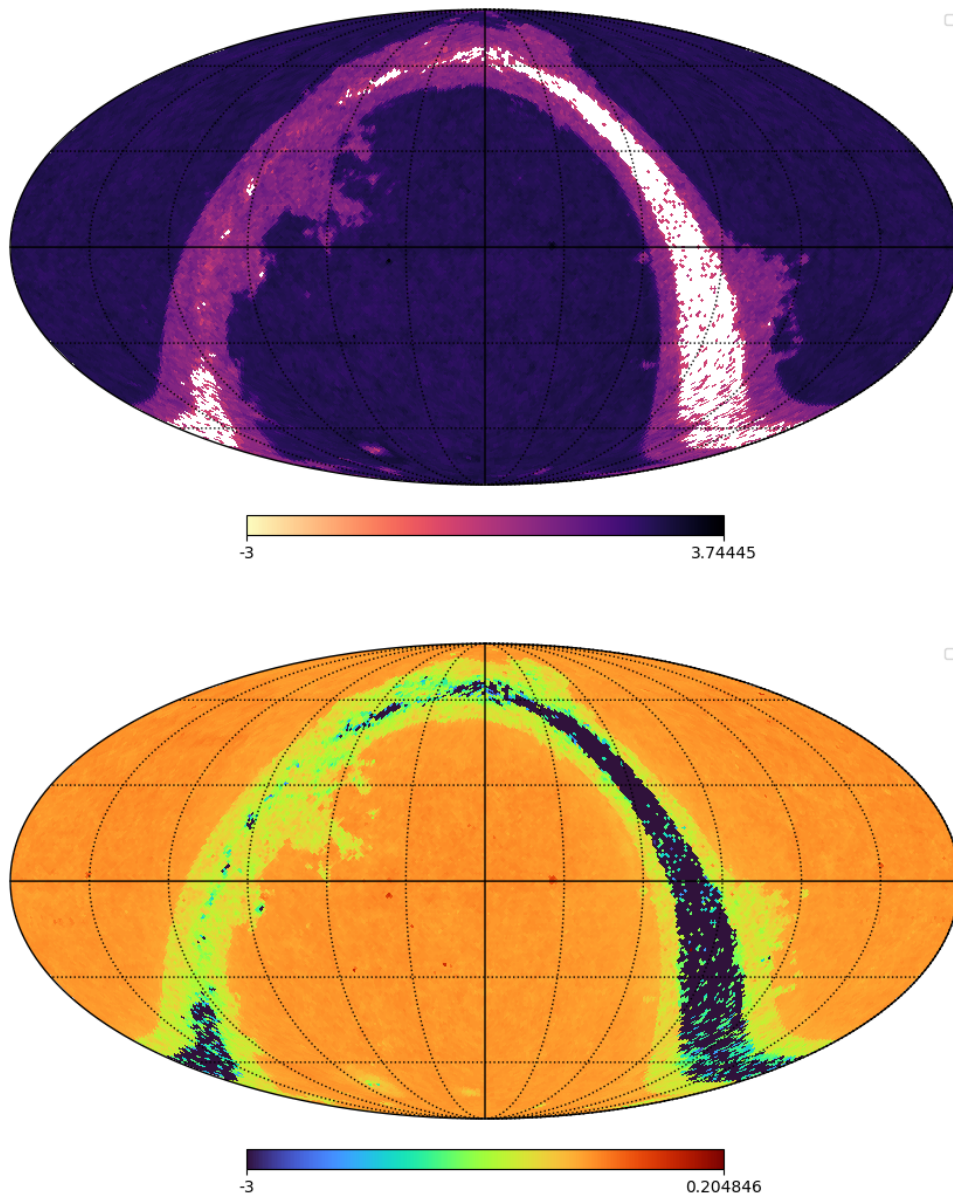


**Figure 2.8:** Two `healpy` maps representing (top) the number density of galaxies within each pixel of the map and (bottom) the average galaxy redshift values of the 23 181 758 objects contained in GLADE+ in each pixel with `nside = 64`; both quantities are represented by colormaps, which are set to a  $\log_{10}$  scale.

<sup>3</sup><http://healpix.sourceforge.net>

## 2.3 The CHIMERA framework

CHIMERA (Combined Hierarchical Inference Model for Electromagnetic and gRavitational wave Analyses) (Borghi, Mancarella, Moresco, et al. 2024) is a Python code designed to perform joint Bayesian inferences for cosmological and population parameters starting from gravitational wave signals and, potentially, additional galaxy catalog information in the context of a dark siren approach. The Bayesian approach is described in section 1.5 of this work.

Originally developed for the analysis of mock gravitational wave and galaxy data, CHIMERA makes use of a dark siren likelihood term which, together with a selection bias term  $\xi(\lambda)$ , constitutes the main component of the posterior term (refer to equation 1.56):

$$p(d^{GW}|\lambda) \propto \frac{1}{\xi(\lambda)^{N_{ev}}} \prod_{i=1}^{N_{ev}} \int \mathcal{K}_{gw,i}(z, \hat{\Omega}|\lambda_c, \lambda_m) \frac{p_{gal}(z, \hat{\Omega}|\lambda_c) p_{rate}(z|\lambda_z)}{\int p_{gal}(z, \hat{\Omega}|\lambda_c) p_{rate}(z|\lambda_z) dz d\hat{\Omega}} dz d\hat{\Omega}; \quad (2.1)$$

In the following sections I briefly present the components of the likelihood term; the main changes I applied to said terms are discussed in sections 2.5.2 and 2.5.3 of this Chapter for what concerns the selection bias and the completeness correction respectively.

### The GW Kernel $\mathcal{K}_{gw}$

The GW Kernel  $\mathcal{K}_{gw}$  is the GW posterior  $p(\theta_i|d_i^{GW}, \lambda)$  marginalized over the binary masses, re-weighted to be proportional to the adopted mass function  $p(m_1, m_2|\lambda_m)$  and converted to source-frame quantities through  $|\frac{d\theta_i}{d\theta_i^{det}}|$ ; overall, the term can be expressed as follows:

$$\mathcal{K}_{gw,i}(z, \hat{\Omega}|\lambda_c, \lambda_m) := \iint \frac{p(\theta_i|d_i^{GW}, \lambda_c)}{\pi(\theta^{det})} \left| \frac{d\theta_i}{d\theta_i^{det}} \right| p(m_1, m_2|\lambda_m) dm_1, dm_2. \quad (2.2)$$

Within the code, this kernel is computed after a preliminary pixelization of the GW event localization area (the pixelization procedure is adaptive, and automatically chooses the best *nside* parameter, see section 2.2.3, on the basis of the localization area of the event).  $\mathcal{K}_{gw,i}(z, \hat{\Omega})$  is approximated by a Kernel Density Estimate (or KDE) properly weighted as mentioned above. As for the GW data that is used to compute this term, each LIGO-Virgo-KAGRA (LVK) run stores files using different keys and waveforms that were used to infer the values of the parameters. In order to operate the CHIMERA code on files from different runs, the `DataGW.py` module translates the files' keys relative to a set of relevant parameters (primary and secondary mass, luminosity distance, right ascension and declination) by copying them to a separate dataset whose keys are the ones used and recognized by CHIMERA. As for the choice of the waveform, `DataGW.py` contains a list of possible waveform names to pick from: if an event's file does not contain the data relative to the first name in the list, `DataGW.py` looks for the second one and so on until a valid name is found.

### The Galaxy Catalog Redshift and Solid Angle Distribution $p_{gal}(z, \hat{\Omega})$

On the basis of the pixels selected to compute the GW kernel, the  $p_{gal}$  probability is calculated using only those galaxies that are enclosed within that same region of space, more specifically in a given confidence level (chosen to be 90% in this work). The full expression of the  $p_{gal}$  term can be found in equation 1.70. If the catalog is thought to be complete, the  $p_{gal}$  probability is assumed to be a sum of Gaussian distributions of each galaxy's redshift PDF contained within the localization volume, with standard deviations defined by the errors in redshift. If the catalog is assumed to be incomplete, on the other hand, the correction presented in section 2.5.3 is applied: the catalog is

pre-pixelized with an *nside* parameter set to 32 (as to avoid memory problems), then separated in a number of masks defined on the basis of an agglomerative clustering algorithm, which operates on the number density or the luminosity volume density of galaxies within each pixel. The  $P_{compl}$  probability (Eqs. 1.66 or 1.67) is then computed, depending on the choice of the completeness goal and, subsequently, the completeness fraction of the catalog in the localization region of the GW event (Eq. 1.71);  $P_{compl}$  is notably set to 1 up until the largest redshift value for which the completeness is larger than 1 ( $z^*$ ) as to maintain the mathematical definition of completeness. More details about the actual computation of the completeness term and its implementation in CHIMERA are given in section 2.5.3.

### The Bias Term $\xi(\lambda)$

The bias term, defined as

$$\xi(\lambda) = \int P_{det}(\theta, \lambda_c) p(m_1, m_2 | \lambda_m) p_{gal}(z, \hat{\Omega} | \lambda_c) p_{rate}(z | \lambda_z) d\theta, \quad (2.3)$$

is the equivalent of the likelihood term, which comes into the definition of the posterior probability, that is computed over the parameter space of all detectable gravitational wave events. It can be calculated and implemented in one of two ways:

- as an analytical term proportional to  $H_0^3$ , which is a valid approximation for the bias term for  $H_0$  at low redshifts (see section 2.5) and can be used for a quick evaluation of selection effects when conducting 1-D analyses;
- as a term informed by the population of GW events which, in the absence of a large enough number of observed events, must resort to the *injection* approach.

In the latter case, the probability of an event being detected ( $P_{det}$ ) is computed starting from a set of injections. More details about the actual computation of the bias term and its implementation in CHIMERA are given in sections 2.5.1 and 2.5.2.

The original framework of CHIMERA is applicable to the analysis of mock data, as was done in Borghi 2024 and Borghi, Mancarella, Moresco, et al. 2024, which will also be extended to perform tests on theories that define modifications to General Relativity - *Modified Gravity* (MG, Belgacem et al. 2018) - in the work by Tagliazucchi et al. 2025.

## 2.4 Extending the CHIMERA framework to the analysis of real data

The extension of CHIMERA to the analysis of real data initially required the development of tools that allow us to investigate their properties. With particular focus on the GW events we want to analyze, it is useful to have an understanding of the volume of space in which they are localized, according to the provided posterior samples relative to right ascension, declination, and luminosity distance. An estimate of the localization region, in fact, can be used to determine the number of galaxies located within it; this, in turn, reflects on the significance of using a real catalog in the statistical parameter inference.

My first addition to the code, on this regard, is `GW_stats`, a function contained in the `DataEM.py` module which can be used to provide useful statistics regarding a single GW event or a list of events given a catalog of galaxies (in our case, either the entirety of GLADE+ or a pre-selected sub-sample). It consists of the following sub-functions:

- `map_from_GW`; this function takes a given event's name, an *nside* value to build a healpy map with and a previously generated galaxy count map as arguments; it returns the pixels of the map within which the GW event is localized, along with the number of galaxies contained in those pixels and the 2D area covered by the resulting selection of pixels: This function is mainly used for plotting in `GW_stats`;
- `select_event_galaxies`; this function returns a mask which assigns a value of True to the galaxies which appear in the GW event's localization pixels; it takes two dictionaries containing the EM and GW data respectively and the *nside* parameter as arguments;
- `event_localization_volume`; this function takes the same two data dictionaries as `select_event_galaxies`, the GW event's name (or list of names), the *nside* parameter, a range of possible  $H_0$  values (set to the fiducial value of  $70 \text{ km/s/Mpc}$  by default) which is used to convert the event's  $d_L$  samples to redshift values, and a *sigma\_level* parameter which is used to determine the event's redshift localization volume starting from its average redshift (when set to False, a localization area is considered instead of a localization volume). This function returns an array of galaxies which are identified as being part of the event's localization volume, where the RA-Dec boundaries are identified with the help of `select_event_galaxies`. The function also returns a list of the names of all the galaxies found inside the volume: since a single galaxy can be found in multiple different catalogs, it is assigned to the most populated catalog in which it is found (this choice does not have relevant implications in the rest of the analysis). A further distinction is operated within the list of galaxies according to the errors associated to their redshift measurements: galaxies with errors larger than  $1.5 \cdot 10^{-2}$  are identified as *photometric*, those with errors smaller than  $1.5 \cdot 10^{-4}$  are labeled as *spectroscopic* and what is left is marked as *in-between*. The function prints out the number of spectroscopic, photometric and *in-between* galaxies and stores the names of said objects in an HDF5 file as `galaxy_spec`, `galaxy_photo` and `galaxy_between` respectively.

All of these functions come together into the definition of `GW_stats` as follows:

- The function initializes a time counter which will return the number of seconds it took to run (this is done with the `time` package).
- The function loads the galaxy catalog, an HDF5 file, and stores its columns into the keys of a dictionary.
- A healpy mollweide galaxy count map is built and each GW event's localization region at the 90% and 50% cumulative credibility levels (found through the `find_greedy_credible_levels` function) is plotted onto it. The GW data is extracted using the load function contained in the `CHIMERA.DataGW.DataLVK` module; the area of the localization region, which was previously computed through the `map_from_GW` function, is then printed.
- As a last step, the `select_event_galaxies` function is called for each event.
- The function prints the total time it took to run.

## 2.5 Accounting for GW and electromagnetic selection effects

The bias term described in section 2.3 is determined by the probability of selecting a given GW signal ( $P_{det}$ ); since this term only depends on detector-frame parameters there is no need for a

source-frame conversion; it is defined as

$$P_{det}(\theta) = \int_{d \in \text{Detectable}} p(d'|\theta) dd', \quad (2.4)$$

where  $d$  represents the gravitational wave data and the integral of the likelihood term related to a given set of  $\theta$  parameters is performed over the space of detectable gravitational wave data.

The definition of the space of detectable data largely depends on a luminosity distance threshold; when errors on the luminosity distance are very small, the  $P_{det}$  term can be thought of as a Heaviside theta function in luminosity distance; the integrand in equation 2.3, being defined over redshift, cannot be thought of as independent of source-frame parameters as is the case for  $P_{det}$  alone. The resulting bias term for  $H_0$  in this case can be written as

$$\xi(H_0) = \frac{\int_0^{z_{thr}} (\hat{d}_L^{thr}, H_0) \frac{dV_c}{dz} dz}{\int_0^{z_{RH}} \frac{dV_c}{dz} dz}, \quad (2.5)$$

where  $z_{thr}$  is the threshold redshift that results from a conversion of the selected threshold luminosity distance given a certain  $H_0$  value, and the  $z_{RH}$  redshift value that defines the integral at the denominator is the upper boundary of the largest possible redshift region in which GW events can be detected.

If we assume that  $z_{RH} \gg z_{thr}$ , the numerator keeps a dependency on the cosmology in the upper boundary of the integral; at low redshifts, the bias term can be summarized by the following dependency (Borghi 2024, Chen, Maya Fishbach, and Holz 2018):

$$\xi(H_0) \propto H_0^3. \quad (2.6)$$

When this approximation no longer holds (for example, at larger  $z$ ) and/or we want to extend the analysis to a multi-dimensional parameter space, another approach is recommended.

### 2.5.1 The injection method

Injections are simulated gravitational wave events that can be sampled from a mock GW population distribution, or any other uniform-in-detector-frame distribution. If an SNR threshold is applied to said set of simulated GW events, the  $\xi$  term for a set of hyper-parameters  $\lambda$  can be computed as a Monte Carlo integral over the number of *detected* events,  $N_{det}$ , and normalized over the number of *total* injection events,  $N_{inj}$ :

$$\xi(\lambda) := \frac{1}{N_{inj}} \sum_{i=1}^{N_{det}} \frac{p_{pop}(\theta_i|\lambda)}{p_{draw}(\theta_i)}, \quad (2.7)$$

where  $p_{draw}$  is the probability distribution function from which the injection data points are sampled. The sum presented in equation 2.7 is computed only when the number of event samples that come into it,  $N_{eff}$ , is large enough, more specifically when

$$N_{eff,i} := \frac{\left( \sum_{j=1}^{N_{samples,i}} w_{i,j} \right)^2}{\sum_{j=1}^{N_{samples,i}} w_{i,j}^2}, \quad (2.8)$$

where  $w_{i,j}$  is the weight associated to a single sample of a single event, is larger than a given threshold (5 in this work). This is because, when  $N_{eff}$  is lower than a given threshold, the resulting integral cannot be seen as a good approximation of the analytical one.

## Injection Re-Weighting

Injection data can be generated by starting from a number of underlying population assumptions. Injection samples, for what pertains GW data, are theoretically defined as draws from a population distribution for every event measurement  $i$ :

$$\theta_i \simeq p(\theta|\lambda) \wedge i = 1, \dots, N_{measurements}. \quad (2.9)$$

The  $p(\theta|\lambda)$  distribution, which is sampled over a number indicated by  $j$ , is itself defined as a posterior

$$\theta_i^{(j)} \simeq p(d_i|\theta)p_0(\theta|\lambda) \wedge j = 1, \dots, N_{samples}, \quad (2.10)$$

where  $p_0(\theta|\lambda)$  represents the underlying prior assumptions used to produce the samples; the  $\theta_i^{(j)}$  values themselves can be extracted via sampling over an index  $k$  on the hyper-parameter posterior

$$p(\lambda|D) \propto \left[ \prod_{i=1}^{N_{ev}} \int p(d_i|\theta_i)p(\theta_i|\lambda) \right] p(\lambda), \quad (2.11)$$

which allows us to extract

$$\lambda^{(k)} \simeq p(\lambda|D) \simeq p(\theta|\lambda^{(k)}). \quad (2.12)$$

With this approximation, the event parameter posterior can be thought of as

$$\theta_i^{(k)} \simeq p(d_i|\theta)p(\theta|\lambda^{(k)}), \quad (2.13)$$

which constitutes a draw from the  $p(\theta|\lambda, D)$  distribution. Said draw is equivalent to the extraction of a random sample  $\theta_i^{(j)}$ ; in order to remove the dependency on the adopted prior, which is the main goal of re-weighting, associated to each  $\theta_i^{(j)}$  sample is the following weight (W. M. Farr and Callister 2021):

$$w_i^{(j)} \propto \frac{p(\theta_i^{(j)}|\lambda^{(k)})}{p_0(\theta_i^{(j)})}, \quad (2.14)$$

where  $p(\theta_i^{(j)}|\lambda^{(k)})$  is extracted from the hyper-parameter posterior defined earlier.

## Injection Sensitivity

Injection sets depend on the sensitivity of the network they were created to simulate. For this reason, choosing an injection dataset that is coherent with the observed GW data and the run during which it was observed is pivotal.

Considering that we use GWTC-3 events in our analysis, which includes events that were observed up to the O3b run, the injection files selected for this work are extracted from the sensitivity estimates for O3 provided by the LVK Collaboration (L. S. Collaboration, V. Collaboration, and K. Collaboration 2021). Injection files are structured in HDF5-format files; four sets are provided for different parameter spaces, Binary Neutron Star (BNS), Neutron Star Black Hole (NSBH), Binary Black Hole (BBH) and Intermediate Mass Black Hole binaries (IMBH) spaces specifically.

This work's analysis is entirely based on the BBH injection file, except for the BNS event GW170817 and GW190814, classified as a possible NSBH; for this and other reasons, which are discussed later in this work, these last two events are analyzed separately.

The main detector-frame parameters that can be extracted from the O3 BBH injection file are shown in Figure 2.9 and are the primary and secondary masses  $m_1^{det}$  and  $m_2^{det}$ , the Signal-to-Noise Ratio of the events, the inclination of the binary  $\iota$  (measured as the angle between the normal to

the binary's orbit and the observer's line-of-sight), the luminosity distance, and the redshift, which is obtained by assuming  $H_0 = 70 \text{ km/s/Mpc}$ . Re-weighting is performed during the computation of the bias term in CHIMERA by making use of the `sampling_pdf` parameter present in the files. Figure 2.9 shows the distributions of the O3 injection parameters compared to those of the O4 and O5 runs taken from Borghi, Mancarella, Moresco, et al. 2024. The distributions are normalized to the total number of samples to account for the different number of total simulated injections. The most noticeable differences are in the SNR, which is reasonably expected to extend to larger values for future LVK runs.

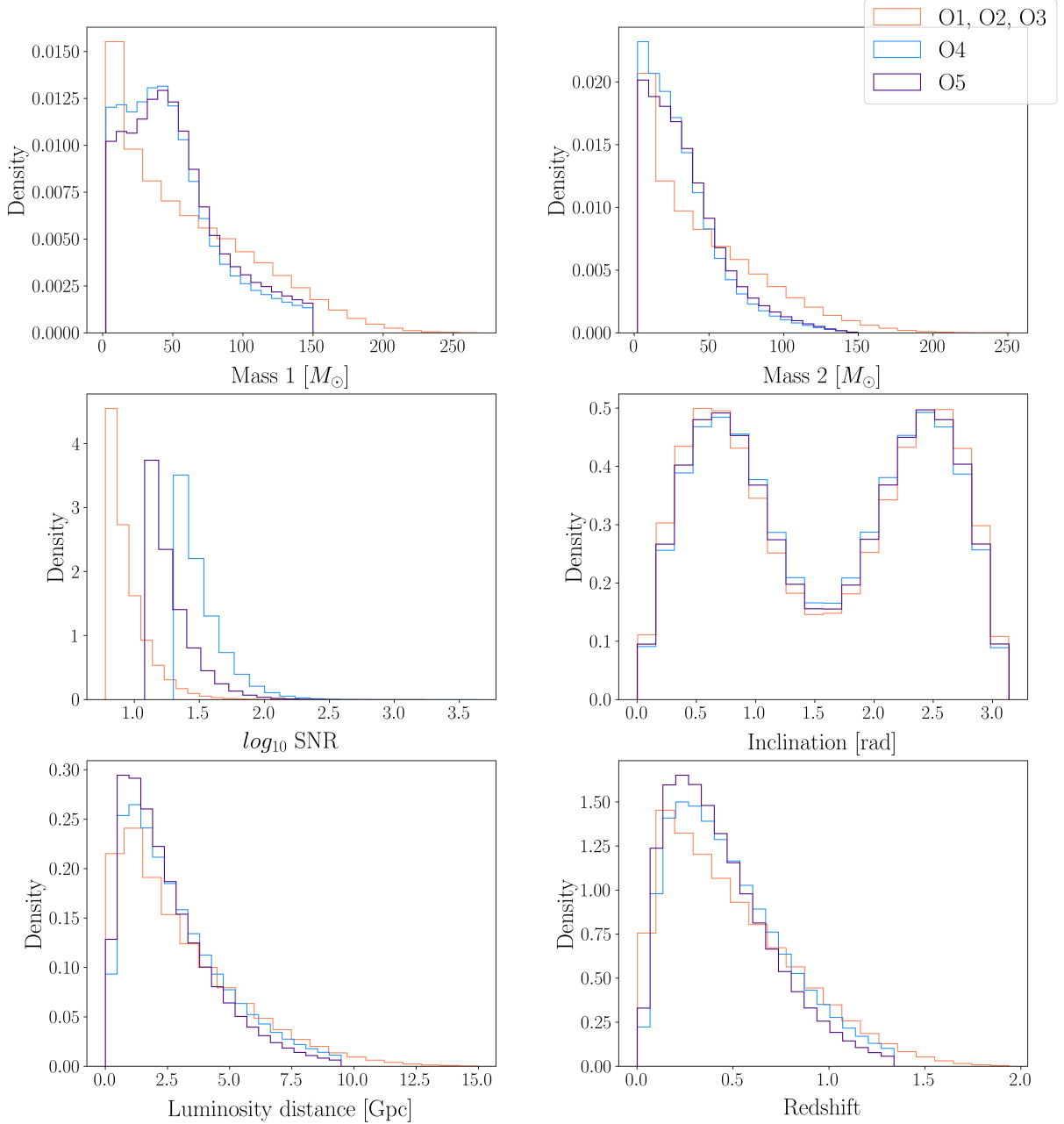


**Figure 2.9:** Density distributions of the main parameters of O3 injections provided by the LVK Collaboration (L. S. Collaboration, V. Collaboration, and K. Collaboration 2021) and O4 and O5 injections provided by Borghi, Mancarella, Moresco, et al. 2024. The parameters are the primary mass in detector-frame  $m_1^{det}$  and the secondary mass in detector-frame  $m_2^{det}$  in  $M_\odot$  (first row), the logarithm in basis 10 of the Signal to Noise Ratio and the line-of-sight's inclination with respect to the binary's normal  $\iota$  (second row), the luminosity distance in  $Gpc$  and the redshift obtained by assuming  $H_0 = 70 \text{ km/s/Mpc}$  (third row).

## 2.5.2 Computing GW selection effects in CHIMERA

Starting from an injection catalog whose underlying assumptions are consistent with the observation run our events belong to (in this case we use the injection file provided by the LVK Collaboration for the O3 run), the Bias module can be used to compute the bias term, given a mass and a rate model (which are consistent with the ones used to compute the likelihood). The significance of different choices for the selection bias is made clearer in Chapter 3.

I adapted `Bias.py` to handle different types of injection data: the module can now differentiate between different LVK runs (O3, O4 and O5) through the run parameter and extract the correct keys from the relative injection files. This makes the code adaptable to future O4 and O5 data analysis. Since the bias term must be consistent with the likelihood at the numerator, the distribution used in place of  $p_{cat}$  is a luminosity-weighted redshift interpolant of the entire galaxy catalog similar to the one presented in Figure 2.6 (the plot for the weighted case can be found in Appendix A, Figure A.6); moreover, when luminosity cuts ( $L_{cut}$ , see Table 2.3) are applied to the catalog that is used to compute the likelihood, this choice must reflect on the bias term: the luminosity-weighted redshift interpolant must be cut in luminosity as well. Using the entirety of GLADE+ to obtain an interpolant of the catalog would be computationally expensive: for this reason, a random sub-sample of 100 000 galaxies is selected to perform this task after verifying that this procedure does not impact on the overall shape of the interpolant. Figure 2.10 shows a comparison of the bias term computed for each set of injection data (O3, O4, O5) compared to the analytical term  $H_0^3$  presented earlier. The bias term is computed assuming the same mass and rate models, in this case POWER-LAW PLUS PEAK and MADAU-DICKINSON, with a set of parameters defined as follows: for `plp`,  $\lambda_p = 0.03$ ,  $\alpha = 3.78$ ,  $\beta = 0.81$ ,  $\delta_m = 4.8$ ,  $m_{low} = 4.98 M_\odot$ ,  $m_{high} = 112.5 M_\odot$ ,  $\mu_g = 32.37 M_\odot$  and  $\sigma_g = 3.88$ ; for `madau_dickinson`,  $\gamma = 4.59$ ,  $\kappa = 2.86$  and  $z_p = 2.47$  (refer to Table 2.2). The galaxy term that comes into the definition of the bias, instead, simulates the case of a complete catalog, for which no completeness correction is required. Including a real galaxy catalog in the computation of the bias and likelihood terms must also account for the catalog *incompleteness* at higher redshifts: the way this is done is explained in section 2.5.3.

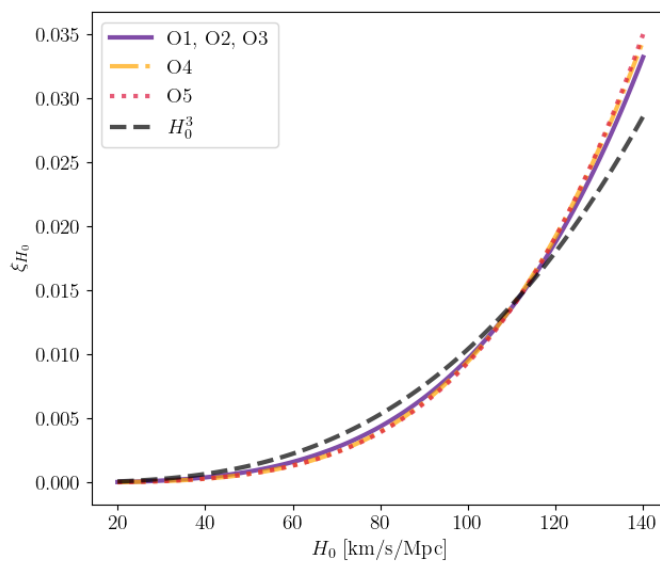


**Figure 2.10:** Bias terms computed from three injection files representing simulated BBH populations for the O3 (violet), O4 (orange), and O5 (red) observing run. In black, the analytical bias term proportional to  $H_0^3$ . All terms are normalized on a redshift grid comprised between 0 and 5.

### 2.5.3 Computing the completeness term in CHIMERA

As already mentioned in Chapter 1, the completeness correction aims to compensate for the galaxies that are missing from a catalog by assuming that they follow a given distribution in the Universe ( $\frac{dV}{dz}$ , in our case).

Firstly, it is useful to identify all areas in which the completeness impacts the computation of the probability terms. We start from the  $p_{gal}$  (Eq. 1.70) and consider the case of homogeneous completeness for the missing galaxies (Eq.1.72). We get:

$$p_{gal} = p_{cat} \cdot f_R + \frac{(1 - P_{compl})}{V_c} \frac{dV}{dz}, \quad (2.15)$$

the elements that are impacted by catalog incompleteness are  $f_R$ , the completeness fraction (Eq. 1.71), and  $P_{compl}$ , which is referenced as *completeness interpolant* from here forward (Eqs. 1.66, 1.67). The CHIMERA modules I modified to introduce this correction are `Completeness.py`, `Likelihood.py` and `Bias.py`; their implementation following my updates can be summarized as follows:

1. The `Completeness.py` module is used to compute the  $f_R$  and  $P_{compl}$  terms separately;
2.  $f_R$  and  $P_{compl}$  are loaded by the `Likelihood.py` module and included in the  $p_{gal}$  term;
3. Two *average*, all-sky  $f_R$  and  $P_{compl}$  terms are used within `Likelihood.py` to compute a background galaxy probability, which is then passed on to the `Bias.py` module to create a symmetry between numerator and denominator in the definition of the posterior probability.

The workflow is summarized in Figure 2.11.

In order to understand the implementation of this correction, the `Completeness.py` module must be introduced, more specifically, the `MaskCompleteness` class. What follows is a schematic description of the class and what the functions within it do with a set of galaxy data.

- Galaxy data is loaded and the (RA, Dec) information is converted into pixels for a given *nside* parameter; in order to avoid memory issues the number of pixels shouldn't be too large, since this would also diminish the benefits of pixelization: for this reason, *nside* is kept at a value of 32 for every step of my analysis;
- If present, galaxy weights are assigned to a class variable (see equation 1.67 for the case of luminosity weighting).
- An average mask consisting of the number density of galaxies for each pixel is computed and used in logarithmic scale to cluster the various pixels through the `AgglomerativeClustering` function.
- For each mask, an interpolant function is computed over a range of redshift bins; the number (or luminosity) densities on which it is based are first gaussianly smoothed and the resulting distribution is normalized over a *completeness goal*, which represents the expected number (or luminosity) density value. The resulting set of completeness values is set to 1 for redshift values lower than  $z^*$ , which is the redshift at which the last completeness value is larger than one; as a last step, the completeness values are used to produce an interpolant in redshift.

The added completeness term modifies both the likelihood and bias terms in different ways: as for the likelihood, the completeness correction is computed for a number of masks (4 in the following analysis) and re-assigned to the event's localization pixels; as for the bias term,

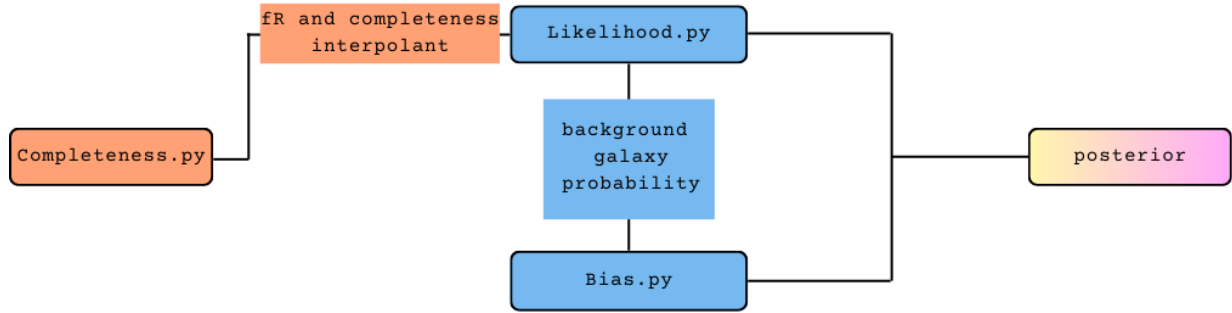


**Figure 2.11:** Completeness correction workflow in CHIMERA.

an *average* interpolant is computed by considering a single mask in order to cover the entire sky area; the mask and average completeness interpolants are saved to external directories, `dir_compl_GLADE` and `dir_compl_sky` respectively, and used in `Likelihood.py` and `Bias.py` when the completeness parameter is set to a string such as `Active` (refer to Table 2.3). The interpolants can be saved to a pickle-format file and plotted for each mask (see Figures 2.12 and 2.13). The completeness fraction  $f_R$  is calculated as defined in equation 1.71, with the comoving volume term  $V_c$  defined by the boundaries of the same redshift range that is used to normalize the rate (`z_det_range`). Figure 2.12 (top) shows a `healpy` map which displays the mask separation produced by `AgglomerativeClustering` with a set of 4 masks; these masks cover different areas, mainly the inner and outer portions of the Milky Way, on the account of there being less observed galaxies, and the remaining portion of the sky, presumably complete to a higher degree.

By choosing different completeness goals, one can set the expected number density (or luminosity density in the case of weighting) to various thresholds. These values can be obtained from deep galaxy surveys as in Conselice et al. 2016, which compile comprehensive measurements of the observed galaxy densities as a function of galaxy mass up to  $z \simeq 8$ . Typical number density when considering galaxies within a given mass range (in  $\log_{10}$  in the subscripts) are:

$$\begin{aligned} \overline{n_{gal}}_{[6,12]} &\simeq 0.1 \text{ Mpc}^{-3} \\ \overline{n_{gal}}_{[9,12]} &\simeq 0.01 \text{ Mpc}^{-3} \\ \overline{n_{gal}}_{[10,12]} &\simeq 0.005 \text{ Mpc}^{-3} \end{aligned}$$

Figure 2.12 (center and bottom rows) shows the interpolants computed for four masks that were identified on the basis of the average number density and in the case of the different completeness goals mentioned above. It is possible to notice how increasing the completeness goal naturally causes the  $P_{compl}$  interpolant to decrease with smaller redshifts. A more astrophysical approach to interpolant computation is given by luminosity weighting, as is described in section 1.7. Once again, different thresholds can be selected to define completeness; in this case, thresholds depend on different  $L_{thr}$  values and the selected luminosity band (my choice for the following analysis is the K luminosity band as it is thought to be a proxy for stellar mass, M. Fishbach et al. 2019). Figure 2.13 (top) shows the `healpy` map of the interpolants computed over 4 masks for  $L_{thr} = 0.02 L_*$ , while the center and bottom rows show the  $P_{compl}(z)$  distributions obtained with different  $L_{thr}$  choices, namely  $0.2 L_*$ ,  $0.02 L_*$  and  $0.002 L_*$ . One can notice how the completeness interpolants computed on the basis of luminosity density are, on average, complete to higher redshifts, on account of the fact that brighter galaxies are less subject to EM selection effects and are observed at higher values of  $z$ . Applying this type of correction, however, may affect the posteriors of those events that are well-localized and are associated to a smaller number of galaxies: such galaxies may be heavily impacted by the additional probability term and wouldn't compensate for its presence.

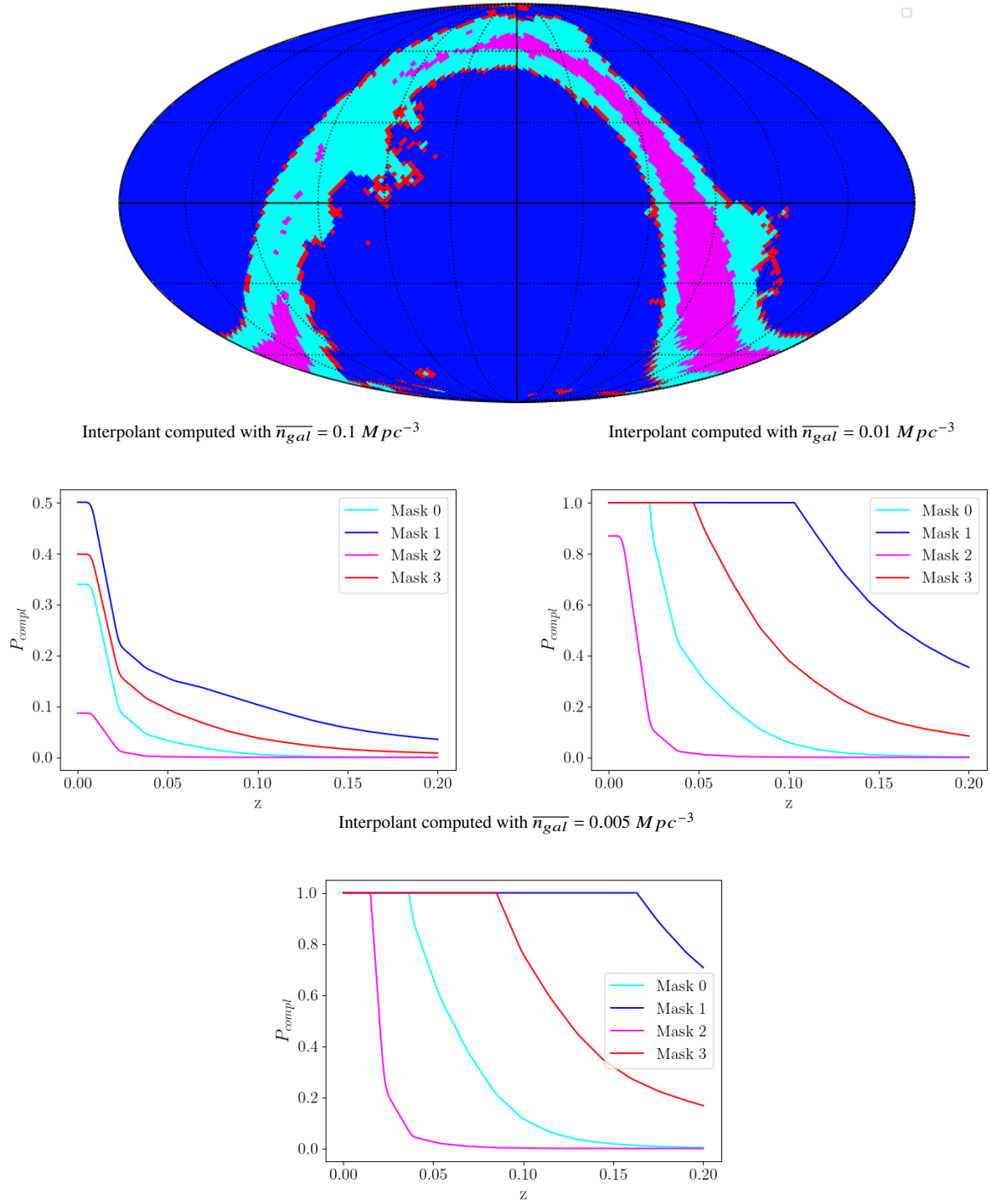


**Figure 2.12:** On top, a healpy map displaying 4 masks resulting from the agglomerative clustering of the galaxies contained in the GLADE+ catalog on the basis of their number density per pixel. Underneath, a set of three completeness interpolants computed starting from the GLADE+ catalog, whose sky coverage was separated into 4 masks. Each interpolant was calculated with a different completeness goal: the first (center-left) was computed with a number density completeness goal equal to  $\overline{n_{gal}} = 0.1 \text{ Mpc}^{-3}$ , the second (center-right) with  $\overline{n_{gal}} = 0.01 \text{ Mpc}^{-3}$ , the third (bottom) with  $\overline{n_{gal}} = 0.005 \text{ Mpc}^{-3}$ .

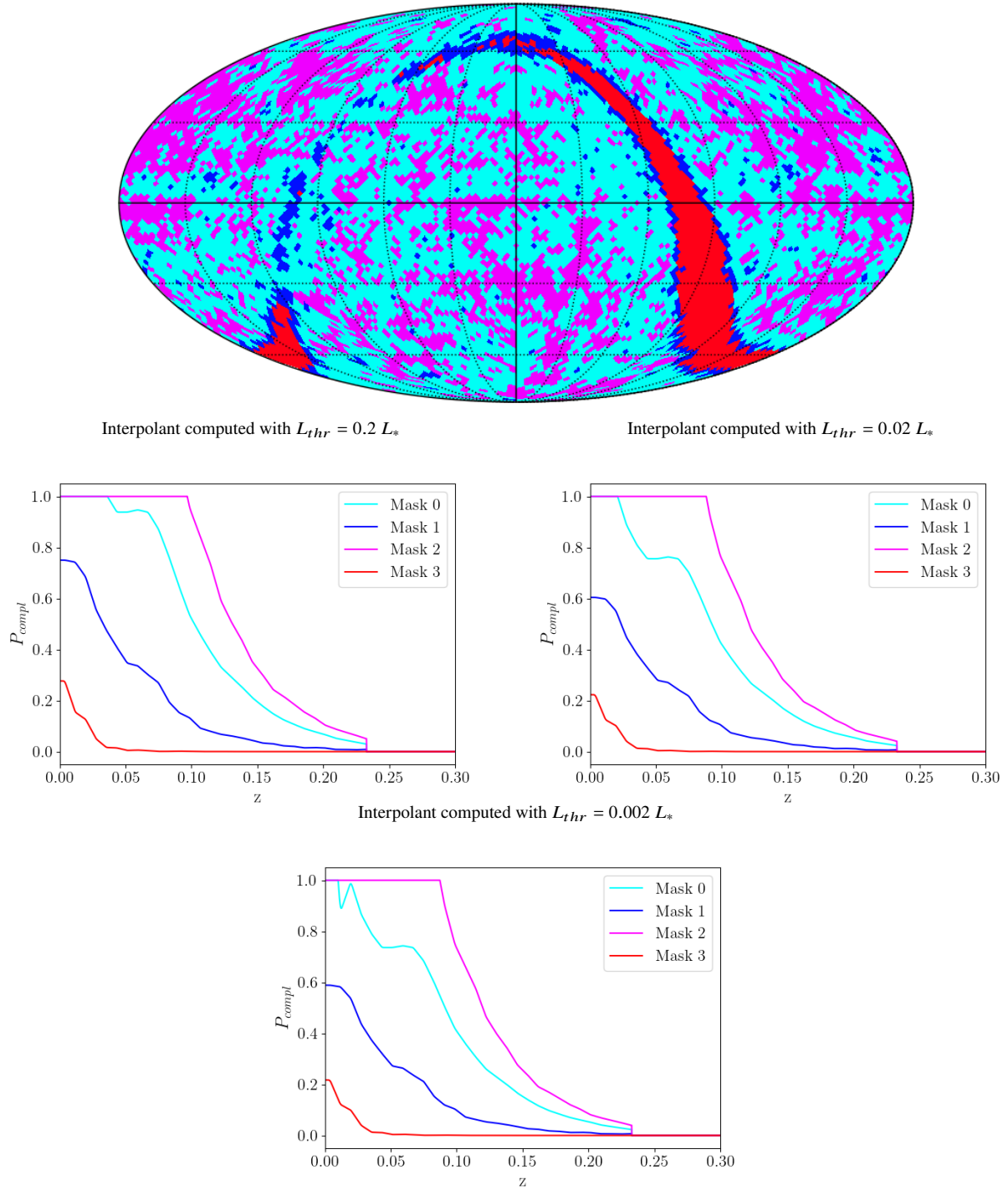


**Figure 2.13:** On top, a healpy map displaying 4 masks resulting from the agglomerative clustering of the galaxies contained in the GLADE+ catalog on the basis of their K-band luminosity with a set  $L_{thr}$  threshold of  $0.02 L_{\odot}$ . Underneath, a set of three completeness interpolants computed starting from the GLADE+ catalog, whose sky coverage was separated into 4 masks. Each interpolant was calculated with a different completeness goal: the first (center-left) was computed with a luminosity density completeness goal based on  $L_{thr} = 0.2 L_*$ , the second (center-right) with  $L_{thr} = 0.02 L_*$ , the third (bottom) with  $L_{thr} = 0.002 L_*$ .

## 2.5.4 The updated CHIMERA workflow

The updated workflow of the code is summarized in Figure 2.14 and can be explained as follows: the mass, rate, spin and cosmological models found in the `mass.py`, `rate.py`, `spin.py` and `cosmo.py` modules of the code, are processed by the `GW.py` module, while the completeness correction is initialized by the `Completeness.py` module (when requested). Galaxy and gravitational wave data are handled by the `DataEM.py` and `DataGW.py` modules, respectively; the processed data comes into the `GW.py` module to build the GW Kernel, which is then handled by the `Likelihood.py` module together with  $p_{gal}$ . The bias term is handled separately with the use of external injection data using the `Bias.py` module; the likelihood term is then divided by the bias term to obtain the full posterior relative to the given hyper-parameters  $\lambda$ . Table 2.3 includes all the parameters of interest used inside CHIMERA with a short description where necessary. Table 2.2, on the other hand, features a list of all the parameters that are used to describe the galaxy and GW populations when the POWER-LAW PLUS PEAK and MADAU-DICKINSON models are used.

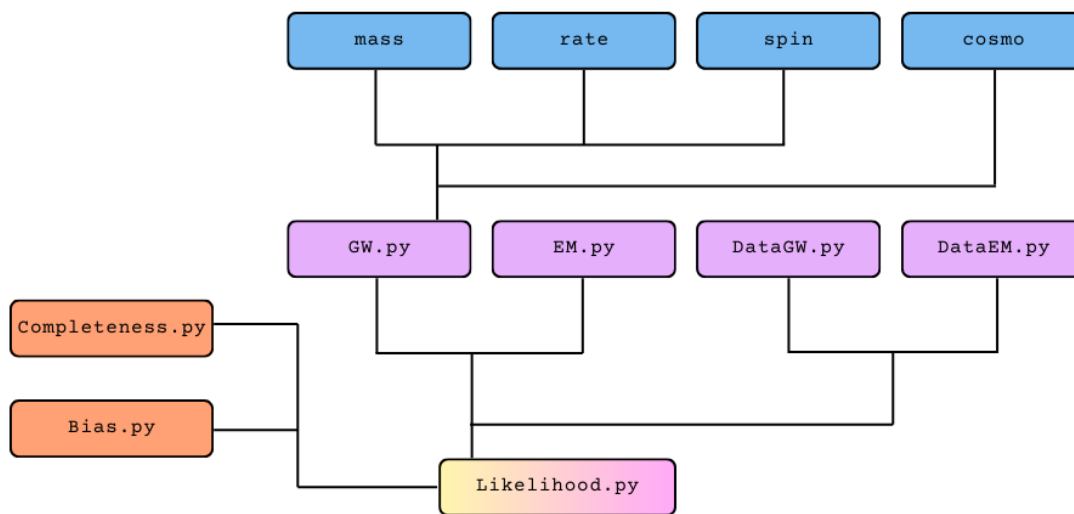


**Figure 2.14:** Workflow of the CHIMERA code (Borghini, Mancarella, Moresco, et al. 2024). In blue, the modules of the code that contain the various population and cosmological assumptions, in violet those that handle the galaxy and gravitational wave terms in the computation and in orange the selection corrections that are computed separately.

**Table 2.2.** Parameters used for the main population and cosmological models (POWER-LAW PLUS PEAK, MADAU-DICKINSON and FLRW) in CHIMERA, together with the SCHECHTER FUNCTION used to describe the galaxy luminosity distribution. See sections 1.6, 1.7 and 1.1 for detailed descriptions of the parameters.

POWER-LAW PLUS PEAK [1.6]	MADAU-DICKINSON [1.6]	FLRW [1.1]	SCHECHTER [1.7]
$\lambda_p$	$\gamma$	$H_0$	$L^*$
$\alpha$	$\kappa$	$\Omega_{m,0}$	$M^*$
$\beta$	$z_p$	$\Omega_{k,0}$	$\alpha$
$\delta_m$		$\Omega_{r,0}$	$\phi^*$
$m_{low}$		$w_0$	
$m_{high}$		$w_a$	
$\mu_g$			
$\sigma_g$			

**Table 2.3.** Parameters used for the computation of the likelihood and bias terms in CHIMERA. In bold, the descriptions of the parameters added to introduce the completeness term and the injection-based bias term.

Parameter	Description
model_cosmo	the cosmological model adopted for the analysis
model_mass	the mass model adopted for the analysis
model_rate	the CBC merger rate model adopted for the analysis
dir_GW	directory of the GW posterior sample files
event_list	list of GW events to be analysed
Nsamples	number of posterior samples to be randomly selected from the GW files
data_GW_smooth	smoothing factor applied to the computation of the $p_{GW}$ term
data_GAL_weights	if present, the galaxy data is weighted according to its luminosity in a given band
sky_conf	confidence level used to delimit the localization area
nside_list	list of <i>nside</i> parameters the program can choose from
z_int_sigma	uncertainty level assigned to the boundaries of the redshift grid over which the GW Kernel is computed
z_det_range	redshift limits within which the rate term is normalized
$H_0$ _prior	values within which the $H_0$ term can vary
z_int_res_like	redshift grid resolution for the computation of the likelihood term
kde_kind	the type of Kernel-computing scheme to use
kde_cut_sigma	defines the boundaries within which to compute the GW Kernel
kde_binned	determines whether the data is binned before computing the GW Kernel
num_bins	number of data bins if <code>kde_binned</code> is True
data_GAL_dir	directory of the galaxy catalog
$L_{cut}$	cut in luminosity to be applied to the galaxy catalog (in units of the $L_*$ of a Schechter function)
band	luminosity band to consider when applying a luminosity cut
completeness	<b>string which can activate the completeness module</b>
dir_compl_GLADE	<b>directory of the masked completeness interpolant for the galaxy catalog</b>
dir_compl_sky	<b>directory of the sky-averaged completeness interpolant for the galaxy catalog</b>
z_det_range	redshift limits within which the bias term can be normalized (optional)
z_int_res_bias	redshift grid resolution for the computation of the bias term
p_bkg	interpolant used to approximate the distribution of galaxies in the galaxy catalog
file_inj_dir	directory of the injection file
neff_min	minimum number of effective injections required
N_inj	total number of injections
snr_th	SNR threshold to determine which injection samples are to be considered 'observed'
run	<b>LVK run simulated by the injection file</b>

# Chapter 3

## Results from GWTC-3 data

The following Chapter contains the results obtained by applying the new framework discussed in Chapter 2 to real data; this includes the addition of a completeness correction and an injection-based bias term to the computation of cosmological and astrophysical parameter estimates through Bayesian inference. Given the wide variety of possible choices that can be made for the completeness term, I choose a  $P_{compl}$  interpolant based on the catalog’s luminosity as described in Chapter 2; among the values for  $L_{thr}$  presented in section 2.5.3 I choose  $L_{thr} = 0.02 L_*$ , which is not too stringent and does not cause the completeness correction to become dominant at low redshift values and also accounts well for the redshift distribution of galaxies in GLADE+.

In order to first validate and test the robustness of the new pipeline to then implement it to real data, we follow an incremental approach, through which we first apply the new pipeline to two notable GW events (GW170817 and GW190814) which are known to be the best GW events found to date. These serve as illustrative cases to test the completeness-informed pipeline on a controlled setup. For this particular case, the two events are used to produce posteriors for  $H_0$  by fixing all population parameters and, together with the best results, the  $H_0$  posteriors obtained by changing the parameters used to compute the likelihood and bias terms. This is done in order to determine the effects of various systematic differences on the final posterior; in particular, the absence of an injection-based bias term and of a completeness correction, changes to the luminosity cuts and weighting applied to the galaxy catalog and the  $\sigma$  parameter used to compute the redshift grid over which the  $p_{gw}$  term is computed.

Once the robustness of the code is validated, we expand the approach to the full set of 42 BBHs from the GWTC-3 catalog described in Chapter 2 (Gray, R et al. 2023, Abbott, R. et al. 2023a); we limit our analysis to  $H_0$  in this case as well, and perform the same tests that are also carried out on GW190814 and GW170817 to identify possible differences between the two cases; in addition to those, the BBH sample is also tested on different assumptions regarding the  $m_{low}$  and  $\gamma$  population parameters, which appear to be very impactful on the shape and peak of the  $H_0$  posterior. We refer to these two cases as *1D posterior analysis*, exploring the constraints only on  $H_0$  and fixing all the other values to fiducial ones.

Finally, we explore the full posterior obtained for a set of 12 cosmological and astrophysical parameters with the sample of 42 BBHs. This is done by making use of a Markov Chain Monte Carlo simulation, which produces a joint cosmological and population inference whereas the astrophysical parameters are previously assumed to be fixed at fiducial values. With regards to the corner plot results relative to the  $m_{low}$  and  $\gamma$  population parameters, I investigate the possible anti-correlation trends between them and  $H_0$ . All posterior constraints for  $H_0$  in this Chapter are presented with errors derived from an uncertainty level equal to 68%.

### 3.1 Applying the new framework to two representative events

In order to test the robustness of the code, with particular focus on the additional completeness term and the injection-based bias term, I select two representative gravitational wave signals to apply them to: GW170817 and GW190814, two events that are commonly found in the existing literature. This portion of the analysis is limited to the production of  $H_0$  posteriors in a controlled parameter setup, which also allows for a study of possible systematics. With regards to the case of GW190814, in particular, I carry out a variety of tests by modifying certain parameters; the areas of interest are:

- The **bias term** - the event posteriors are computed both with and without the use of injection data in order to determine the significance of using them instead of an analytical term proportional to  $H_0^3$  (see section 2.5); this is done in the absence of a completeness correction.
- The **completeness correction** - the addition of a completeness correction, whose interpolant is always computed with a luminosity threshold equal to  $L_{thr} = 0.02 L_*$ , is tested by comparison with posteriors where it is not included (see section 2.5.3).
- The **luminosity cut** - by setting the  $L_{cut}$  parameter to different values, it is possible to analyze the effects of ignoring galaxies that are less luminous than a set of different thresholds; in particular, it is useful to compare the varying levels of uncertainty of the  $H_0$  posterior peak. The values chosen to perform the luminosity cuts are  $L_{cut} = 1 L_*$  and  $L_{cut} = 0.001 L_*$  (see Table 2.3).
- **Luminosity weighting** - a luminosity-dependent weight can be assigned to the galaxies within the galaxy catalog as follows: given a redshift range over which to compute a single galaxy's redshift likelihood  $p_{gal}(z)$ , the normalized, non-weighted Gaussian probability is given by

$$\frac{p_{cat,i}(z) \frac{dV}{dz}}{\int_{z_{min}}^{z_{max}} p_{cat,i}(z) \frac{dV}{dz} dz}, \quad (3.1)$$

where the index  $i$  iterates over the redshift values,  $p_{cat}(z)$  is the redshift probability associated to each galaxy as given by the galaxy catalog and  $z_{min}$  and  $z_{max}$  are the extremes of the chosen redshift range. If one introduces weighting, the numerator is multiplied by the weights relative to each redshift value and the overall probability is normalized over their sum as follows:

$$\frac{\sum_i \left[ \frac{p_{cat,i}(z) \frac{dV}{dz}}{\int_{z_{min}}^{z_{max}} p_{cat,i}(z) \frac{dV}{dz} dz} \right] w_i}{\sum_i w_i}. \quad (3.2)$$

The effects of luminosity weighting can be compared to those that derive from applying luminosity cuts: in the tests that follow, the posteriors obtained with a stringent cut at  $L_{cut} = 0.6 L_*$  and no weighting are compared to those obtained through K-band luminosity weighting alone, without cuts (see Table 2.3 for definitions of the relevant parameters).

- The  $\sigma$  **redshift grid parameter** - the effects of computing the event's  $p_{gw}$  term on wider or narrower redshift grids is tested by modifying the `z_int_sigma` parameter in the likelihood recipe (Table 2.3).

The parameters that are subject to change when analyzing the effects listed above, together with all other parameters used to produce posterior inferences, are presented in Tables 3.1, 3.2, and 3.3. The effects of parameter variations are more visible when applied to GW190814, whose posterior results are compared to the work by Gray, R et al. 2023. The same tests are also applied to a set of BBH GWTC-3 events, as shown in section 3.2.

### 3.1.1 GW170817 as a dark siren

Since its detection in 2017, GW170817 (Abbott, B.P. et al. 2017b) has so far represented the only example of a bright siren case; it is in fact associated to the detection of a transient electromagnetic event, through which an accurate identification of the emitting source (located within NGC4993) was possible. This in turn allowed to localize the event within a very small area of the sky, which is visible in Figure 3.1. For these reasons, GW170817 presents unique advantages in its ability to precisely constrain cosmological parameters such as  $H_0$ . Despite this particular event allowing for  $H_0$  estimation in a *bright siren* framework (with a resulting a-posteriori peak value and minimal 68.3% credible interval of  $H_0 = 70.0^{+12.0}_{-8.0} \text{ km/s/Mpc}$ , as shown in Abbott, B. P. et al. 2017a), we use it in this work as if no electromagnetic counterpart was available for it, as in M. Fishbach et al. 2019, which we take as a reference analysis. The results we obtain with this approach must not be taken as the best possible ones, but rather as a test on the validity of our framework.

When applied to the case of GW170817, `Gw_stats` returns a galaxy catalog cutout relative to the event's localization area (when a sigma level is not specified) or its localization volume (when a sigma level is specified). The galaxy catalog cutout is then used within `LikeNumeratorLVK` to compute the EM and GW terms within the likelihood and, consequently, the  $H_0$  posterior with a given bias term.

The likelihood term in particular requires a set of assumptions concerning the population mass and rate models referring to our object type: since GW170817 is classified as a BNS event, describing such a population is not straightforward; for this reason, we choose uniform distributions for both the mass and rate models (`dummy_mass` and `dummy_rate`, respectively). The parameters chosen for the cosmological model are the following:  $\Omega_{m,0} = 0.3$ ,  $\Omega_{k,0} = 0$ ,  $\Omega_{r,0} = 0$ ,  $w_0 = -1$ ,  $w_a = 0$ ; the parameters of the Schechter luminosity function which is used to describe the galaxy catalog's distribution and to apply possible luminosity cuts and weights are:  $L_* = 4.06 \cdot 10^{10} L_\odot$ ,  $M_* = -23.39$ ,  $\alpha = -1.09$ ,  $\phi_* = 5.5 \cdot 10^{-3}$ . The full list of the likelihood and bias parameters is presented in Table 3.1. The changes in

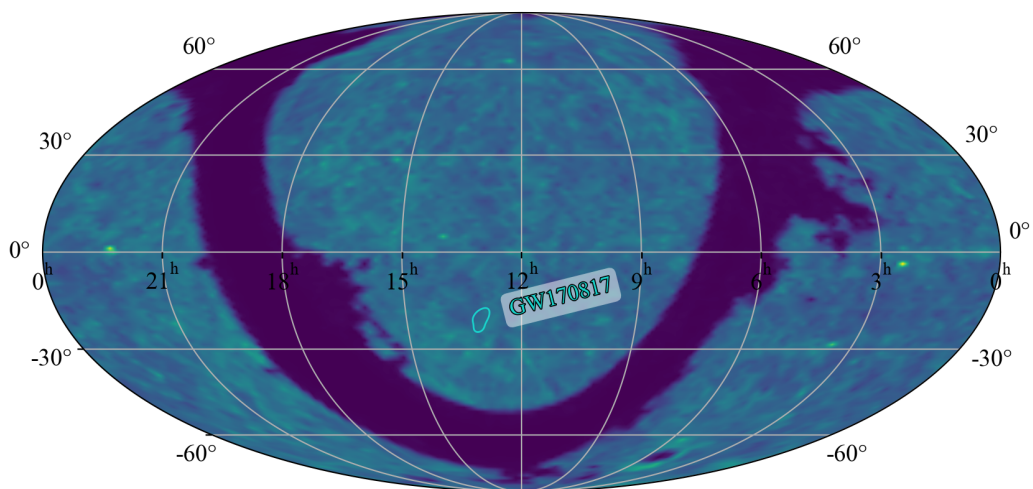


**Figure 3.1:** Localization area of GW170817 at a level of uncertainty equal to 90%; the heatmap underneath assigns an average number density to each pixel by means of a colormap.

the bias, luminosity cuts and weighting,  $H_0$  prior, and completeness do not significantly impact

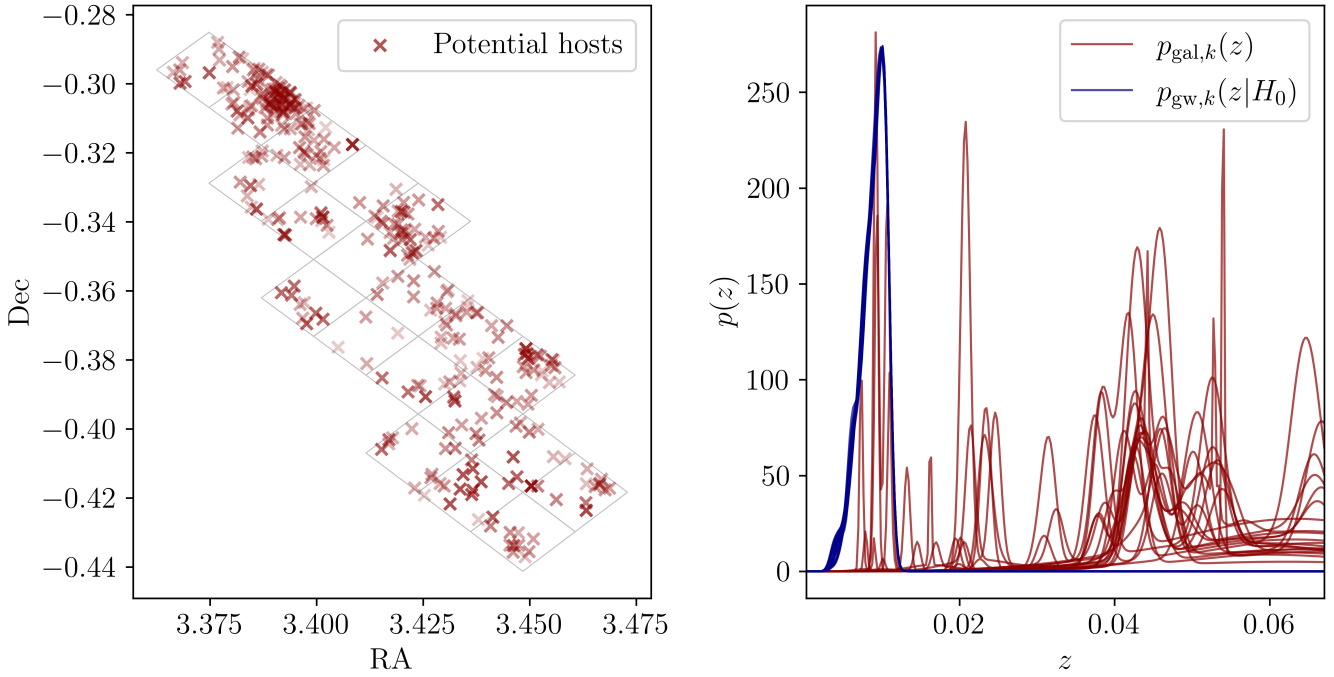
Table 3.1. Parameters used for the computation of the likelihood and bias terms for GW170817 (see Table 2.3 for the definitions). In bold, the parameters that are varied throughout the analysis in order to determine their impact on the results.

Parameter	Value
model_cosmo	flrw
<b>model_mass</b>	dummy_mass
<b>model_rate</b>	dummy_rate
Nsamples	3000
data_GW_smooth	0.3
<b>data_GAL_weights</b>	L-K (K-band luminosity)
sky_conf	0.9
nside_list	[512, 256, 128, 64, 32, 16, 8]
<b>z_int_sigma</b>	5
z_det_range	[0, 5]
H0_prior	[10, 200]
z_int_res_like	300
kde_kind	full
kde_cut_sigma	2
kde_binned	True
num_bins	100
<b>Lcut</b>	0.02 $L_*$
band	K
<b>completeness</b>	Active
z_det_range_bias	None
z_int_res_bias	1000
p_bkg	interpolant
neff_min	5
N_inj	4009760
snr_th	20
run	O3

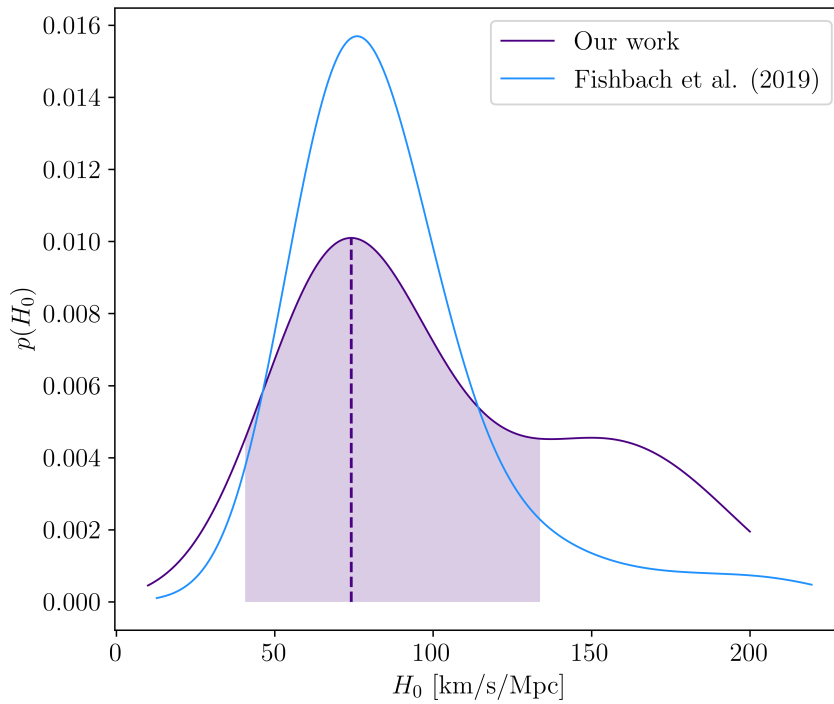
the results. In Figure 3.3 we present a reference posterior plot, which is obtained with a bias term computed with the O3 injection file provided by the LVK Collaboration, a completeness interpolant with a luminosity threshold of  $L_{thr} = 0.02 L_*$ , luminosity weighting on the K-band and an  $L_{cut} = 0.02 L_*$  luminosity cut; all the parameters in Table 3.1 are chosen to match the choices made by M. Fishbach et al. 2019, whose results are shown in Figure 3.3 in comparison to ours (data points digitized from Figure 6 of M. Fishbach et al. 2019).

Figure 3.2 shows the positions of the galaxies within the event’s localization region (left) and the event’s term in the likelihood,  $p_{gw}$  (right, blue), with the galaxy terms,  $p_{gal}$  (right, red), with the same choices in parameters. To convert the GW luminosity distance in redshift, a value of  $H_0 = 70 \text{ km s}^{-1} \text{ Mpc}^{-1}$  is adopted. It is interesting to note that there is a peak in  $p_{gal}$  in close proximity of the  $p_{gw}$ . Table 2.1 shows that most of the galaxies that are found in this event’s localization region are characterized by redshift errors comprised between  $10^{-4}$  and  $10^{-2}$ : this reflects on the width of the gaussian probabilities associated to each galaxy, which are noticeably narrow. Together with this, the  $\frac{dV_c}{dz}$  trend introduced by the completeness term is marginally visible at higher redshift; indeed, GW170817 is located at a redshift where the catalog can still be considered complete.

Our  $H_0$  value for GW170817 is constrained at  $H_0 = 74_{-33}^{+60} \text{ km/s/Mpc}$  (68% confidence level), which is consistent with M. Fishbach et al. 2019’s result at around  $H_0 = 76_{-24}^{+29} \text{ km/s/Mpc}$ . The constraints are obtained by applying a *smoothing factor* to the posterior probability derived from the data: in this case, the smoothing factor is set to 0.5 both for our result and M. Fishbach et al. 2019’s.



**Figure 3.2:** Two plots representing (*left*) the positions relative to all the galaxies in a 90% event localization cumulative credibility region and (*right*) the galaxies' redshift probability distributions (in red) together with the event's likelihood distribution  $p_{gw,k}(z|H_0)$  (in blue). the likelihood and bias terms are computed with the parameters presented in Table 3.1. A completeness correction calculated with a  $L_{thr} = 0.02 L_*$  value is applied (see section 2.5).



**Figure 3.3:** Our  $H_0$  posterior probability function (violet) compared to M. Fishbach et al. 2019's (blue); the likelihood and bias terms are computed with the parameters presented in Table 3.1. A completeness correction computed with a  $L_{thr} = 0.02 L_*$  value is applied (see section 2.5).

### 3.1.2 GW190814: a benchmark dark siren

Observed on August 14<sup>th</sup>, 2019, GW190814 represents a unique case in GW detection. The masses of the two objects that constitute this CBC event were constrained by the LIGO Scientific Collaboration and Virgo Collaboration (R. Abbott et al. 2020) in intervals of  $[22.2, 24.3] M_{\odot}$  and  $[2.50, 2.67] M_{\odot}$ , with the latter being especially interesting given that it could either be assigned to the lightest black hole ever observed or the most massive neutron star to date. Apart from this, the event's significance is also related to its small localization area ( $\simeq 18.5 \text{ deg}^2$ , R. Abbott et al. 2020). By running *GW\_stats* on GW190814 we obtain an area of around  $95 \text{ deg}^2$ , which is larger than the value obtained by R. Abbott et al. 2020, as *GW\_stats* returns the entire pixel area of the event. The localization region at a cumulative credible level equal to 90% is shown in Figure 3.4 (top). As opposed to the case of GW170817, the majority of the galaxies associated to GW190814 is characterized by redshift errors larger than  $10^{-2}$ : this is reflected on the width of the galaxies' gaussian probabilities in Figure 3.4 (bottom), which shows a distribution of said galaxies (left) together with a plot displaying the  $p_{gw}$  term in blue  $p_{gal}$  and term in red (right), with the latter being visibly affected by the completeness correction's  $\frac{dV_c}{dz}$  trend at high redshifts.

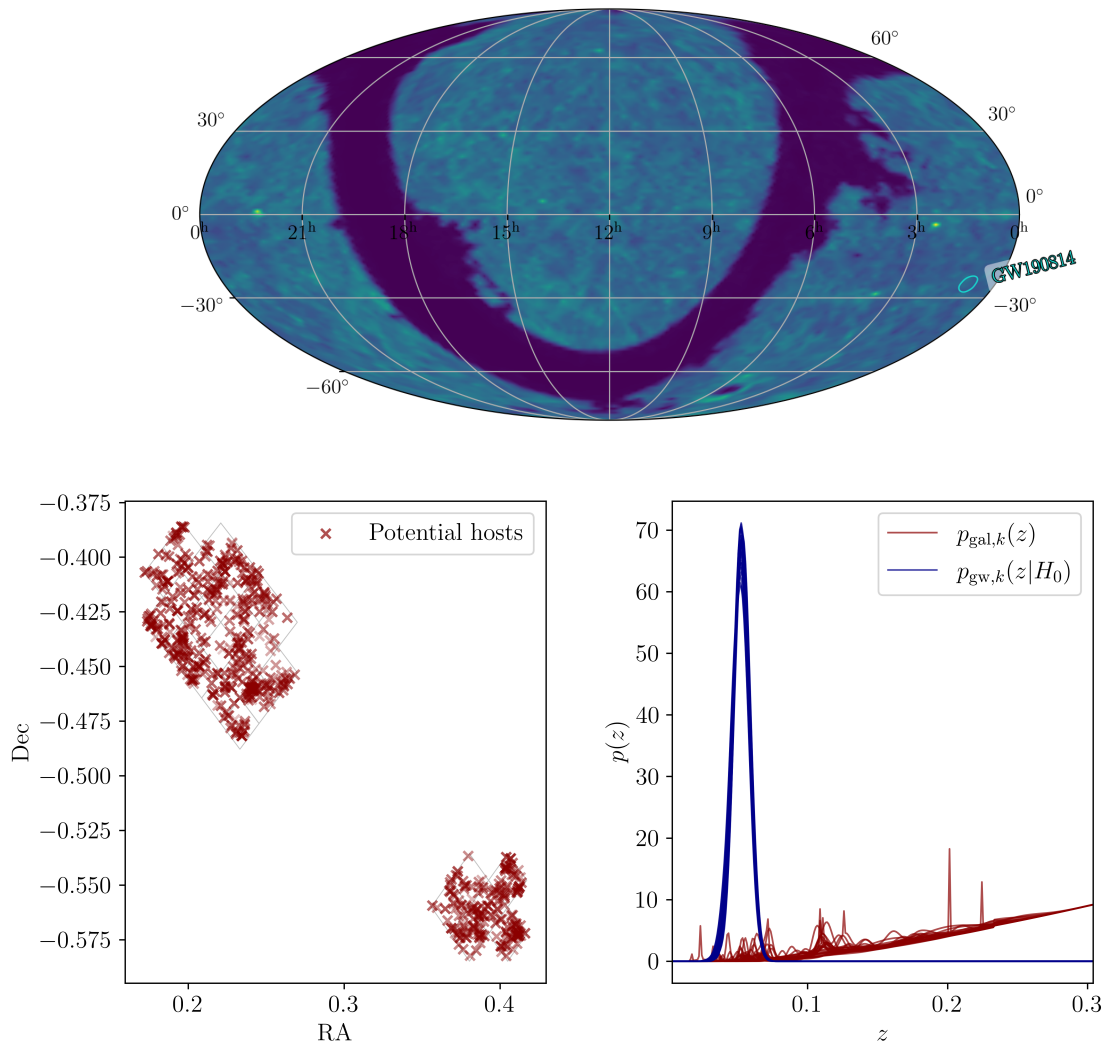


**Figure 3.4:** On top, the localization area of GW190814 at a level of uncertainty equal to 90%; the healpy map underneath assigns an average number density to each pixel by means of a colormap. On the bottom, two plots representing (left) the galaxies selected for GW190814 and (right) the event's  $p_{gal,k}(z)$  (in red) and  $p_{gw,k}(z|H_0)$  (in blue) terms; the parameters used to produce the posterior are presented in Tables 3.2 and 3.3. A completeness interpolant computed with  $L_{thr} = 0.02 L_*$  is used.

### GW190814 - comparison with Gray et al. (2023) and benchmark $H_0$ posterior

The results presented here are obtained by setting population, likelihood and bias parameters to the values used in the work by Gray, R et al. 2023 to allow for comparisons (data taken from [https://git.ligo.org/rachel.gray/gwcosmo-cosmo-pop-method-paper/-/tree/main/data/fixed-population/GW190814?ref\\_type=heads](https://git.ligo.org/rachel.gray/gwcosmo-cosmo-pop-method-paper/-/tree/main/data/fixed-population/GW190814?ref_type=heads)). It is important to briefly discuss the code used to produce the aforementioned results, GWCOSMO (Gray, R et al. 2023, Gray, Messenger, and Veitch 2022, Rachel Gray et al. 2020). The computation of the  $p_{gal}$  term in it is not based on a completeness fraction since it separates the term in two: an *in-catalog* part and an *out-of-catalog* part. Furthermore, its likelihood is computed on a wider redshift grid equal to  $[0.5 \cdot z_{min,GW}, 2 \cdot z_{max,GW}]$ . As for the completeness term, GWCOSMO computes it differently for every GW localization pixel on the basis of each pixel's magnitude threshold.

With all this in mind, the comparisons presented in the following portion of the thesis cannot be considered as the result of a perfect match of assumptions and choices; nevertheless, since the different methods can be thought of as analogous in their theoretical approaches, it is reasonable to compare them by adapting CHIMERA to match them as closely as possible. To do this, our likelihood features the parameters presented in Tables 3.2 and 3.3; in particular, I added a new mass model to the existing ones, `plpandunif`, to describe a Neutron Star-Black Hole Binary population; the model uses a POWER-LAW PLUS PEAK for the binary system's primary mass and a UNIFORM MASS DISTRIBUTION for the secondary defined between 1 and 3 solar masses (Figure A.3). Figure 3.5 shows the posterior resulting from the use of Gray, R et al. 2023's models and parameters; our constraint with errors at the 68% level is  $H_0 = 71^{+50}_{-19} \text{ km/s/Mpc}$  and can be compared to Gray, R et al. 2023's at around  $H_0 = 74^{+59}_{-12} \text{ km/s/Mpc}$ . In both cases, our results are in good agreement with those presented in the existing literature; in particular, some of the  $H_0$  posterior features at lower  $H_0$  are visible in both works and can be further enhanced by modifying the smoothing factor used to plot the posterior (set to 0.05 for both results).

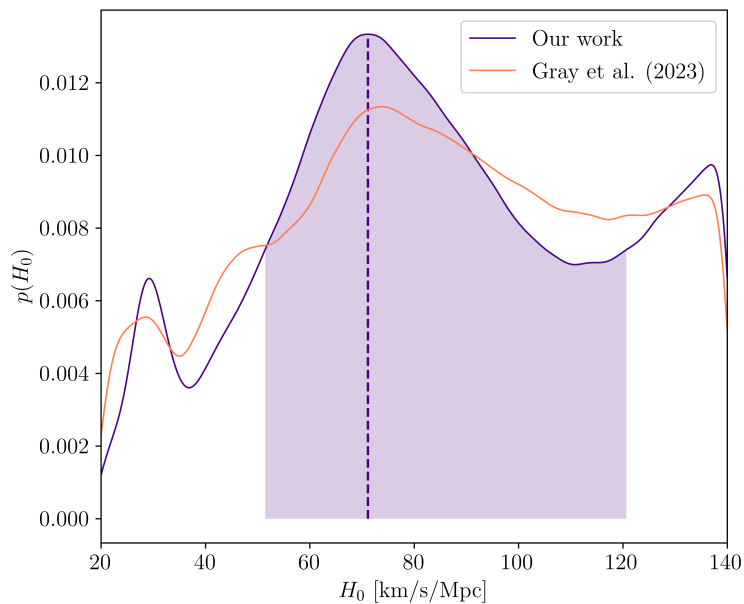


**Figure 3.5:** Our  $H_0$  posterior probability function found for GW190814 (violet), compared to the result obtained by Gray, R et al. 2023 (orange) for the same event and a similar choice of parameters (see Tables 3.2 and 3.3). The bias term is calculated starting from O3 injection data and a completeness interpolant computed with  $L_{thr} = 0.02 L_*$  is used. Gray, R et al. 2023's data is taken from [https://git.ligo.org/rachel.gray/gwcosmo-cosmo-pop-method-paper/-/tree/main/data/fixed-population/GW190814?ref\\_type=heads](https://git.ligo.org/rachel.gray/gwcosmo-cosmo-pop-method-paper/-/tree/main/data/fixed-population/GW190814?ref_type=heads)

## GW190814 - effects of the systematics

The aim of this portion of the work is to test the effect that changing some parameters has on the  $H_0$  posterior computed for GW190814 with a smoothing factor equal to 0.2; the list of possible tests presented at the beginning of section 3.3 is used as a reference point for the following discussion. All the results referenced in this sub-section are presented in Figures 3.6 and 3.7. It is useful to start from a comparison of two cases where the completeness correction is absent: the posterior produced with the analytical bias term  $\xi(\lambda) \propto H_0^3$  and the one produced with injection data. The former, shown at the top-left of Figure 3.6 in red, peaks at  $H_0 = 73_{-24}^{+39} \text{ km/s/Mpc}$ , while the latter, in blue, peaks at  $H_0 = 73_{-23}^{+41} \text{ km/s/Mpc}$ . As a result of the inclusion of the injection-based bias term, the  $H_0$  posterior appears to have slightly higher levels of uncertainty at larger  $H_0$  values.

Issues with catalog incompleteness arise when computing the  $H_0$  posterior for this event. In particular, with reference to Figure 3.7, one can notice how it greatly differs from 3.4: the galactic distribution in the latter is heavily affected by the  $\frac{dV}{dz}$  term which, as one can see in equation 2.15, is assumed to describe the distribution of all the galaxies that are missing from our catalog and effectively make it incomplete.

With the addition of the completeness term, I analyze the effects of imposing different luminosity cuts on the galaxy catalog. More specifically, as anticipated at the beginning of section 3.1, I test two cut values:  $L_{cut} = 1 L_*$  and  $L_{cut} = 0.001 L_*$ . The two resulting posteriors are shown in Figure 3.6 (top-right), where the first cut is in blue and peaks at  $H_0 = 74_{-17}^{+50} \text{ km/s/Mpc}$  and the second (red) peaks at  $73_{-24}^{+46} \text{ km/s/Mpc}$ . By applying a more stringent cut at  $L_{cut} = 1 L_*$  more galaxies are neglected in the computation, more specifically those at lower redshifts, whose probabilities are visible in Figure 3.4: this is the most likely reason behind the reduced probability at lower  $H_0$  values shown by the blue curve, together with the slightly larger level of uncertainty towards larger  $H_0$  ones shown by the peak.

The focus is then moved on the concept of luminosity weighting; I compare the posteriors computed by applying a stringent cut a  $L_{cut} = 0.6 L_*$  and no luminosity weighting to that obtained without luminosity cuts and K-band luminosity weighting alone: the first, peaking at  $H_0 = 72_{-24}^{+41} \text{ km/s/Mpc}$ , is slightly more well-constrained than the second, which peaks at  $H_0 = 73_{-25}^{+45} \text{ km/s/Mpc}$  (these results are shown in Figure 3.6, bottom-left); by keeping galaxies with lower luminosities, even when their redshift probabilities are weighted, the uncertainties become larger at lower  $H_0$  values, which is not the case when applying a stringent luminosity cut with no weighting. On this regard, applying a luminosity cut can be seen as akin to a rough weighting process. An important specification has to be made with regards to the un-weighted case: since likelihood and bias must be coherent with one another, an un-weighted catalog interpolant (akin to the one presented in Chapter 2) was used to compute the posterior, whereas a weighted catalog interpolant (shown in Appendix A, Figure A.6) was used in the other case.

Lastly, some considerations can be made about the posteriors obtained with different choices for the `z_int_sigma` parameter ( $\sigma$ ), which determines the width of the redshift grid used to compute the  $p_{gw}$  term. When setting it to a value equal to 2, the resulting peak at  $H_0 = 73_{-22}^{+46} \text{ km/s/Mpc}$  (red) is almost equal to that which is obtained with a choice of  $\sigma = 10$ , which peaks at  $H_0 = 73_{-21}^{+46} \text{ km/s/Mpc}$  (Figure 3.6, bottom-right); this means that, even when the redshift grid is widened for this event, no additional galaxies are taken into the computation of the  $p_{gw}$  term and therefore do not affect the results.

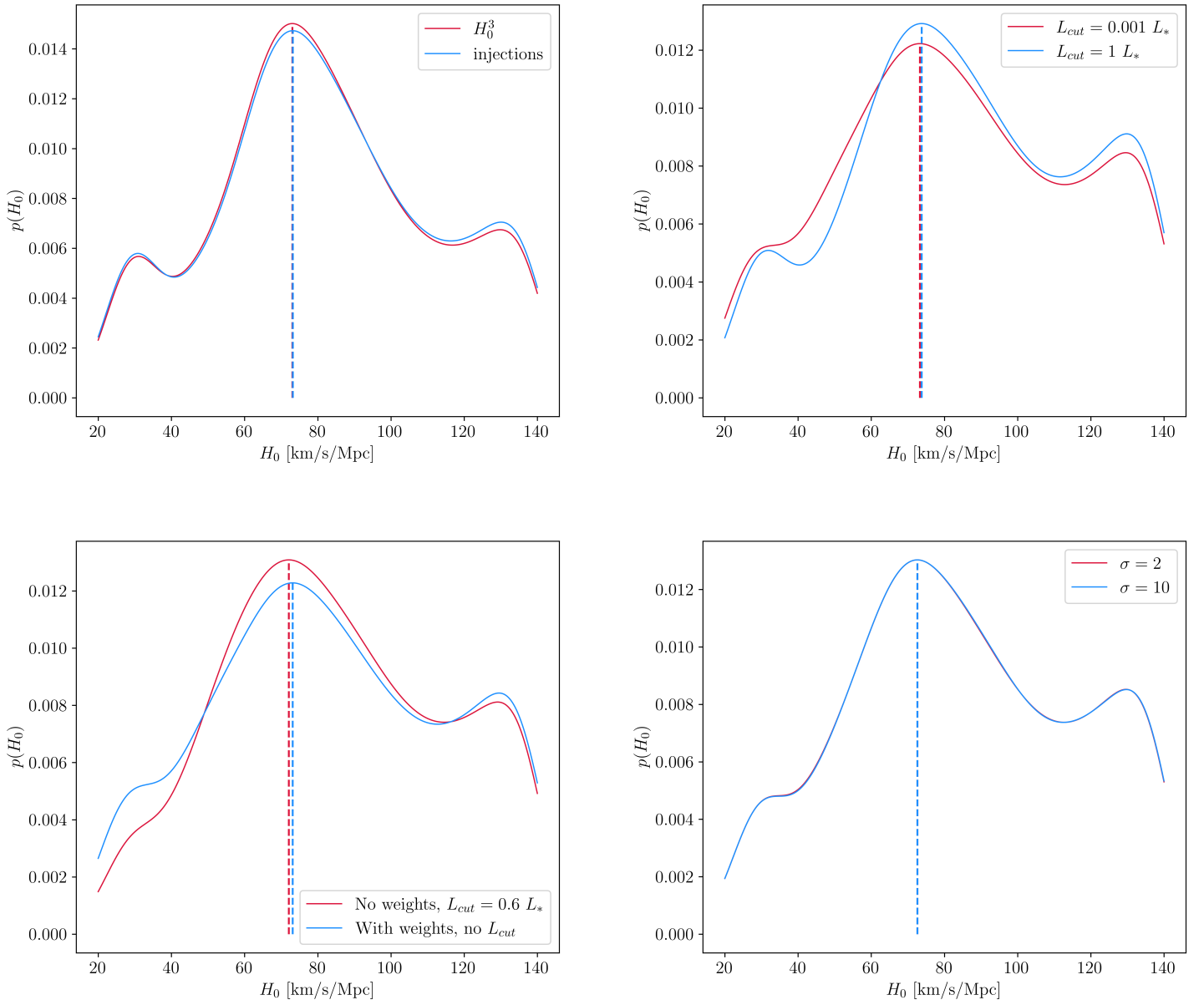


**Figure 3.6:** Set of 4 tests performed on the parameters used to compute GW190814's  $H_0$  posterior. Top-left: no completeness correction and a bias term proportional to  $H_0^3$  (red) or computed with O3 injections (blue); top-right:  $L_{cut} = 0.001 L_*$  (red) or  $L_{cut} = 1 L_*$  (blue); bottom-left:  $L_{cut} = 0.6 L_*$  and no galaxy luminosity weighting (red) or  $L_K$  luminosity weighting and no luminosity cut (blue); bottom-right: redshift grid computed with  $z_{int\_sigma} = 2$  (red) or  $z_{int\_sigma} = 10$  (blue).

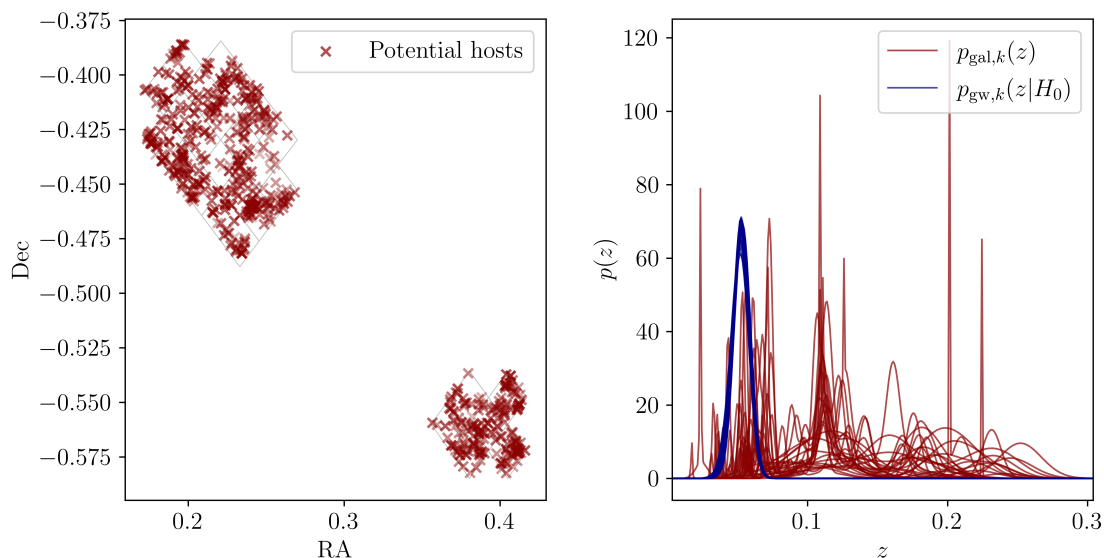


**Figure 3.7:** Two plots representing (*left*) the galaxies selected for GW190814 and (*right*) the event's  $p_{gal,k}(z)$  (in red) and  $p_{gw,k}(z|H_0)$  (in blue) terms when no completeness correction is applied; a cut in luminosity is set at  $L_{cut} = 0.6 L_*$  and the galaxies are luminosity-weighted in the K-band.

**Table 3.2.** Parameters used for the population models, POWER-LAW PLUS PEAK PLUS UNIFORM and MADAU-DICKINSON, for GW190814. See section 1.6 for the definitions.

POWER-LAW PLUS UNIFORM	MADAU-DICKINSON
$\lambda_p = 0.03$	$\gamma = 4.59$
$\alpha = 3.78$	$\kappa = 2.8$
$\delta_m = 4.8$	$z_p = 2.47$
$\mu_g = 32.27 M_\odot$	
$\sigma_g = 3.88$	
$\beta = 0.81$	
$m_{low,BH} = 4.98 M_\odot$	
$m_{high,BH} = 112.5 M_\odot$	
$m_{low,NS} = 1 M_\odot$	
$m_{high,NS} = 3 M_\odot$	

**Table 3.3.** Baseline configuration of CHIMERA for GW190814. In bold, the parameters that are subject to change in the analysis of the systematics for this event. See Table 2.3 for the definitions.

Parameter	Value
model_mass	plpplustpl
model_rate	madau_dickinson
H0_prior	[20, 140]
<b>z_int_sigma</b>	5
<b>data_GAL_weights</b>	L_K
<b>Lcut</b>	0.6 $L_*$
<b>completeness</b>	Active
N_inj	5413902
snr_th	20

## 3.2 Applying the new framework to a sample of 42 BBH events from GWTC-3

This section is divided in two main parts: the first contains the results relative to the 1-D analyses I conducted on the  $H_0$  parameter using the set of 42 BBH events identified as the best by the LVK Collaboration with an  $\text{SNR} > 11$  and presented in Chapter 2. These events represent a benchmark for cosmological analyses with dark sirens and were analyzed, with different codes, in other works (Gray, R et al. 2023, Abbott, R. et al. 2023a): this allows for comparisons.

This section also contains a discussion on how changing certain parameters affects said results, plus the results of a joint population-cosmology analysis obtained through Markov Chain Monte Carlo simulations on the same sample.

The final part of the analysis provides inferences of  $H_0$  together with the population parameters presented in the first two columns of Table 2.2, which are left free to change within a set of prior ranges: these represent the most accurate constraints that we can obtain on  $H_0$  and astrophysical parameters of the BBH population. On the basis of these final results I also discuss the relations between  $H_0$  and a selection of population parameters which are observable in the resulting corner plot; some final considerations are made with regards to O4 and O5 and the ways in which the data that will result from future runs of the LVK detector network is likely to improve parameter inferences. Full posteriors are produced by combining the one obtained for the 42 BBH samples with those relative to GW190814 and GW170817; this is done for the case in which the BBH population parameters are left free to change (the *marginalized* case).

### 3.2.1 1-D analysis of $H_0$

The following analysis is centered on a set of 42 BBH events released by the LVK Collaboration up to their third observing run (O3), selected by applying an SNR threshold at 11 and a FAR threshold at  $\frac{1}{4} \text{ yr}^{-1}$ ; the same sample was also used in the work Gray, R et al. 2023, thus allowing for comparisons.

The analysis of multiple events required some adjustments to be applied to the code; in particular, the completeness term was modified to assign different  $f_R$  and  $P_{\text{compl}}$  values to each event and additional steps were performed to use the posteriors of the events to compute a single *combined posterior*. With regards to the last point, the single posteriors were taken in logarithmic form and summed to produce the combined posterior, which was then re-normalized over the  $H_0$  grid; the exponential of the combined logarithmic posterior is then used to plot the results.

The redshift distribution of the selected sample of events can be found in Figure 2.4; for said plot we assume a standard flat  $\Lambda$ CDM cosmology with  $H_0 = 70 \text{ km/s/Mpc}$  and  $\Omega_{m,0} = 0.3$ .

The recipe adopted for this analysis is nearly identical to the one presented in Tables 3.2 and 3.3 exception made for the mass model, now set to POWER-LAW PLUS PEAK (p1p). As for the bias term, the injection file is one that describes a population of Binary Black Holes, the SNR threshold is set to 11 and the number of total injections to  $\approx 70$  million.

I present the results relative to six different cases: the first one represents the baseline configuration, whereas the following five are relative to the results obtained by varying certain parameters, as was done for the case of GW190814.

- The population parameters used by Gray, R et al. 2023 and the closest match of likelihood and bias parameters to said work, as was done for GW190814, in order to allow for a direct comparison.
- The results obtained with a bias term proportional to  $H_0^3$  and one computed with O3 injection data, both without a completeness correction.
- The results obtained with two different luminosity cuts, namely  $L_{cut} = 1$  and  $0.001 L_*$ , to be applied to the galaxy catalog. These choices for the  $L_{cut}$  parameter are dictated by a need to investigate two extreme cases: two  $L_{cut}$  parameters that are too similar in value may result in the same selection of galaxies and lead to the same resulting  $H_0$  posterior.
- A comparison between the results obtained without luminosity weighting of the catalog's galaxies for  $L_{cut} = 0.6 L_*$  and K-band luminosity weighting with no cut. This test is carried out in order to determine the impact produced by removing galaxies with a luminosity cut as opposed to what is obtained by keeping all galaxies and assigning different weights to them.
- A comparison between the results obtained with two  $z_{int\_sigma}$  (see Table 2.3) values, 2 and 10. Said parameter influences the redshift grid on which the  $p_{gw}$  term is computed and might result in a different selection of galaxies.
- A different choice for the values of the mass and rate parameters  $m_{low}$  and  $\gamma$  (see section 1.6 for the definitions).

### GWTC-3 BBH sample - comparison with Gray, R et al. 2023

In order to ease the comparison with the results from the literature, we chose to fix all the parameters of the astrophysical BBH population to the ones adopted by Gray, R et al. 2023 (data extracted from [https://git.ligo.org/rachel.gray/gwcosmo-cosmo-pop-method-paper/-/tree/main/data/fixed-population/catalog?ref\\_type=heads](https://git.ligo.org/rachel.gray/gwcosmo-cosmo-pop-method-paper/-/tree/main/data/fixed-population/catalog?ref_type=heads)); we show the single-event posteriors obtained for said choices (Figure 3.8) in comparison with Gray, R et al. 2023's and the combined posterior (Figure 3.9), once again compared with Gray, R et al. 2023's; together with the combined posterior are the single-event posteriors obtained through our analysis, shown in gray: it's possible to see how we find  $H_0 = 76_{-14}^{+17} \text{ km/s/Mpc}$ , whereas Gray, R et al. 2023's is constrained at  $H_0 = 64_{-13}^{+13} \text{ km/s/Mpc}$ , with errors defined at a level of 68% uncertainty and a posterior smoothing factor of 0.2.

Despite the two results being consistent with one another within their respective errors (which are still large given the quality of the available data), Gray, R et al. 2023's result is systematically lower than ours.

Said difference can be analyzed by comparing the single-event posteriors relative to our work and Gray, R et al. 2023, as shown in Figure 3.8. Despite most posteriors being in good agreement with each other, some (GW190412, for instance) present visibly different behaviors; given how the differences are mainly found at low values of  $H_0$ , they could be due to the luminosity-weighted catalog interpolant used to produce the bias, or, alternatively, to the completeness correction, which might be shaped differently at low redshifts. These small event-level differences may be responsible for the contrasting peaks found in Figure 3.9 for the combined posteriors.

Together with these reasons, it is worth investigating the possible systematic effects that might also affect the resulting posterior and the constraint on  $H_0$ .

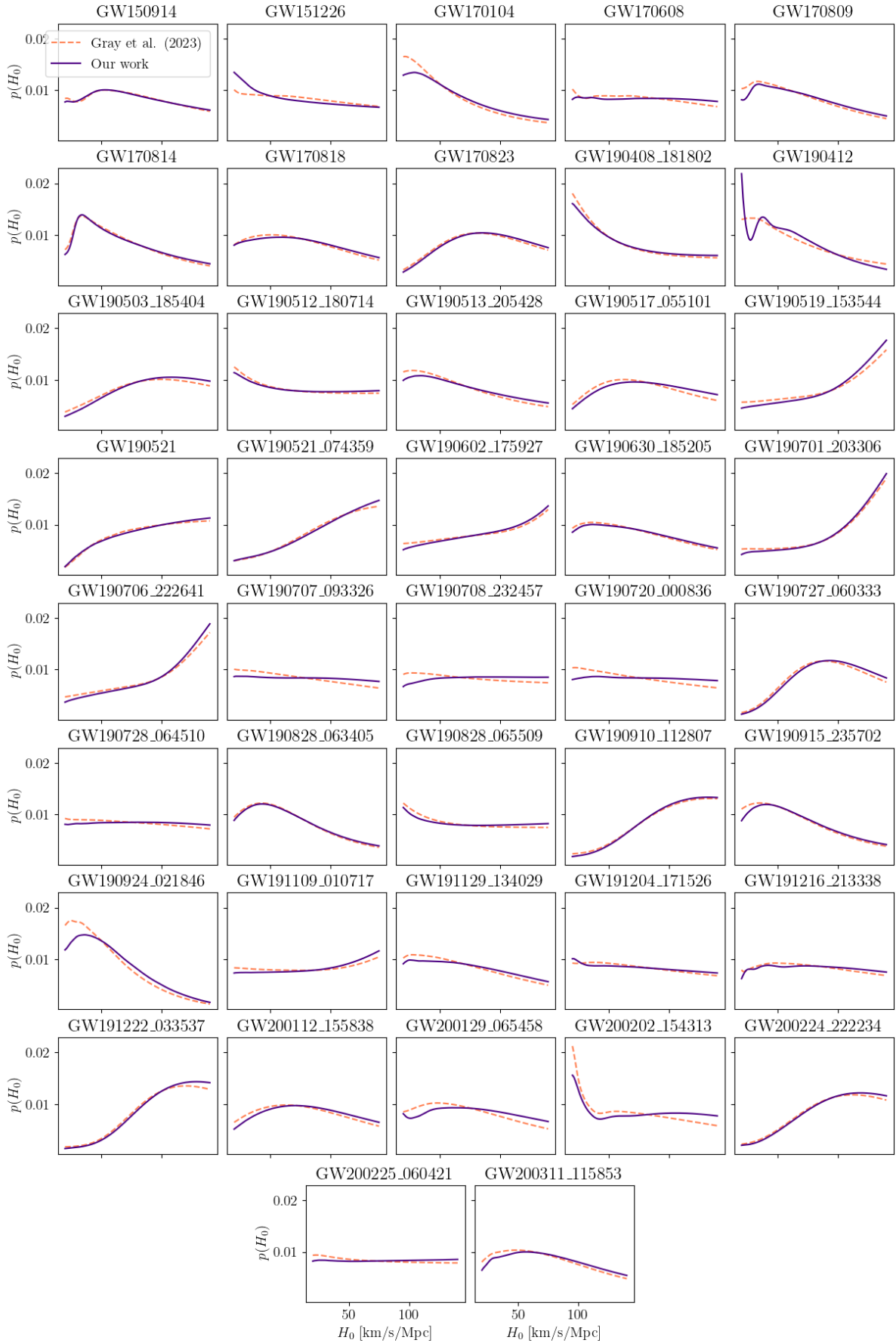


**Figure 3.8:** Single-event  $H_0$  posteriors obtained for a sample of 42 BBH events by Gray, R et al. 2023 (orange) and our work (violet). Gray, R et al. 2023's results were taken from [https://git.ligo.org/rachel.gray/gwcosmo-cosmo-pop-method-paper/-/tree/main/data/fixed-population/catalog?ref\\_type=heads](https://git.ligo.org/rachel.gray/gwcosmo-cosmo-pop-method-paper/-/tree/main/data/fixed-population/catalog?ref_type=heads).

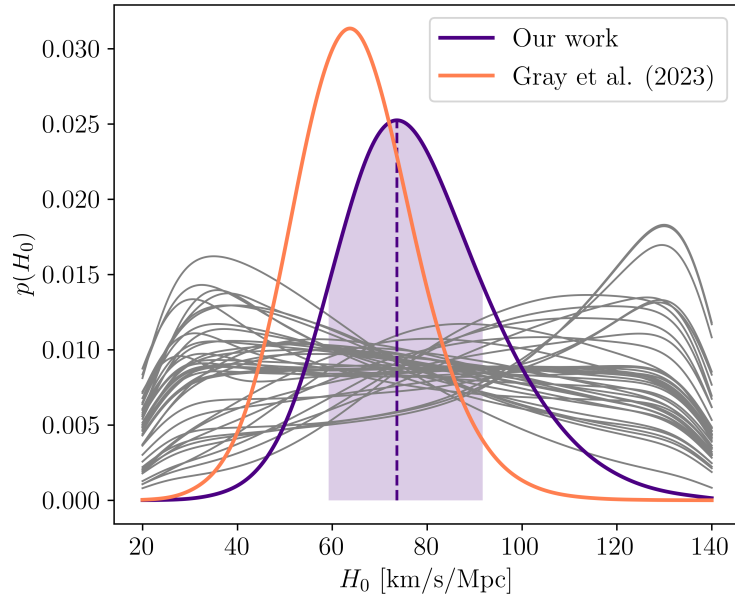


**Figure 3.9:**  $H_0$  combined posterior distribution obtained with a set of 42 BBH events. In violet, the posterior relative to our work; in orange, the posterior relative to Gray, R et al. 2023’s work. The bias term is calculated using O3 injection data and a completeness interpolant computed with  $L_{thr} = 0.02 L_*$  is used. Gray, R et al. 2023’s results were taken from [https://git.ligo.org/rachel.gray/gwcosmo-cosmo-pop-method-paper/-/tree/main/data/fixed-population/catalog?ref\\_type=heads](https://git.ligo.org/rachel.gray/gwcosmo-cosmo-pop-method-paper/-/tree/main/data/fixed-population/catalog?ref_type=heads).

**Table 3.4.** Parameters of the POWER-LAW PLUS PEAK mass population model (section 1.6) adopted for the 1D  $H_0$  analysis. The values are taken by Gray, R et al. 2023

POWER-LAW PLUS PEAK parameter	Value
$\lambda_P$	0.03
$\alpha$	3.78
$\delta_m$	4.8
$\mu_g$	$32.27 M_\odot$
$\sigma_g$	3.88
$\beta$	0.81
$m_{low}$	$4.98 M_\odot$
$m_{high}$	$112.5 M_\odot$

**Table 3.5.** Baseline configuration of CHIMERA adopted for the 1D  $H_0$  analysis. The parameters varied to study potential systematics are shown in bold.

Parameter	Value
model_mass	plp
model_rate	madau_dickinson
H0_prior	[20, 140]
<b>z_int_sigma</b>	5
<b>data_GAL_weights</b>	L_K
<b>Lcut</b>	$0.6 L_*$
<b>completeness</b>	Active
N_inj	73957576
snr_th	11

### GWTC-3 BBH sample - effects of the systematics

Similarly to the analysis I conducted on GW190814 (sub-section 3.1.2), I now explore the possible effects that the various parameters included in the likelihood might have on the final posterior obtained for our sample of 42 BBH events. The results of these tests can be found in Figures 3.10 and 3.11, and can give hints as to which parameters may affect the  $H_0$  fixed-population distribution shown in Figure 3.9.

The most extreme cases are found 3.10 (top-left and top-right), where the effect of including a bias term proportional to  $H_0^3$  is compared to one produced with O3 injection data: both figures are created without applying a completeness correction in the computation of the posterior and, differently than what was found for GW190814, this choice produces significant effects on the results, for which the posterior peaks are heavily shifted towards the lower prior value of the  $H_0$  distribution ( $H_0 = 20_{-0}^{+1} \text{ km/s/Mpc}$  in both cases). We identify a possible source for this bias in the inclusion of events located at larger redshifts, for which the lack of galaxies in the catalog is not properly corrected for. The fact that this bias is present, regardless of the type of bias term, highlights the crucial need for a completeness correction in a dark siren approach.

As for the results found for GW190814, the choice of two different values for the parameter that determines the width of the redshift grid,  $z\_int\_sigma = 2$  and  $10$ , (3.10, center-left and center-right), produces slightly different results. The  $H_0$  posterior peak that results from the first choice is located at  $75_{-14}^{+19} \text{ km/s/Mpc}$ , while the second produces a slightly better constraint at  $74_{-14}^{+17} \text{ km/s/Mpc}$ . Even if these two values do not result in a different selection of galaxies, the peaks may be modified due to normalization effects.

Much like in the case of GW190814, applying two different luminosity cuts at  $L_{cut} = 0.001$  and  $1 L_*$  does not produce visible changes, if not for differences in the position of the peak (3.10, bottom-left and bottom-right respectively). The first produces  $H_0 = 73_{-13}^{+20} \text{ km/s/Mpc}$ , the second  $H_0 = 75_{-16}^{+18} \text{ km/s/Mpc}$ ; the second peak in particular appears to be shifted towards slightly larger  $H_0$  values: this could be caused by the fact that requesting larger luminosities may result in the selection of galaxies located at higher redshifts.

When galaxies are not given weights that are proportional to their K-band luminosity, but rather only excluded on the basis of  $L_{cut} = 0.6 L_*$ , the limitations caused by the reduced statistical power of the analysis are clearly evident. Figure 3.11 (top-left) shows a posterior peak that is located at  $H_0 = 79_{-14}^{+17} \text{ km/s/Mpc}$ ; the relevance of luminosity weighting is highlighted in Figure 3.11 (top-right), where the posterior peaks at  $H_0 = 73_{-13}^{+19} \text{ km/s/Mpc}$ . Despite both results having comparable levels of uncertainty on the peak, the luminosity-weighted case should be considered as the more reliable of the two, given the limitations of GLADE+ at higher redshifts.

The last portion of this analysis focuses on the effects of different values for two population parameters:  $m_{low}$  and  $\gamma$ , which are chosen in order to identify possible trends. Starting from  $m_{low}$ , the two values that are tested are  $m_{low} = 1 M_\odot$  and  $m_{low} = 6 M_\odot$ , for which the results are shown in Figure 3.11 (center-left and center-right respectively): it is clearly visible how setting the parameter in question to lower values (first case) moves the  $H_0$  constraint to a larger value ( $H_0 = 103_{-10}^{+11} \text{ km/s/Mpc}$ ), while the opposite is true for the second case (peaking at  $H_0 = 56_{-15}^{+15} \text{ km/s/Mpc}$ ), with one event being particularly subject to an increase in posterior probability at lower  $H_0$  values. We note that  $m_{low} = 1 M_\odot$  is un-physical as the minimum mass for a stellar black hole mass model is found at around  $5 M_\odot$  (see section 1.6). As for  $\gamma$ , a similar trend can be identified when choosing two values,  $\gamma = 1$  and  $\gamma = 10$  which, for the chosen model, correspond to a lower peak at lower redshift and a higher peak at higher redshift respectively: the first choice results in a constraint equal to  $H_0 = 69_{-19}^{+20} \text{ km/s/Mpc}$  (3.11, bottom-left), while the second produces a peak at  $H_0 = 47_{-10}^{+9} \text{ km/s/Mpc}$  (3.11, bottom-right); the discussion on these apparent anti-correlations between  $H_0$  and  $m_{low}$ ,  $\gamma$  is presented in sub-section 3.2.2.

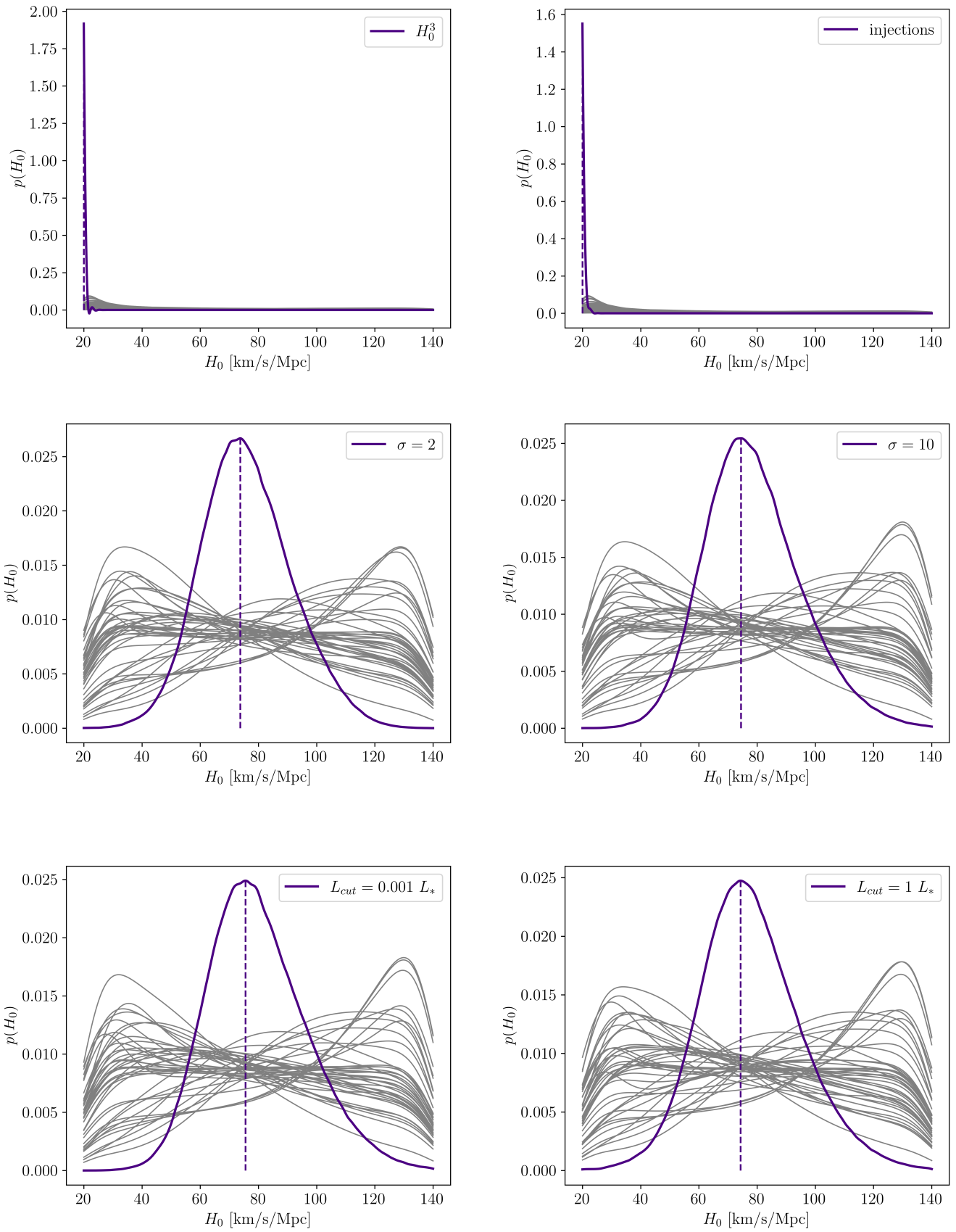


**Figure 3.10:** Set of six tests performed on the parameters used to compute the combined  $H_0$  posterior starting from a set of 42 BBH events. Top-left:  $H_0^3$  bias; top-right: injection-based bias; center-left:  $z_{\text{int\_sigma}} = 2$ ; center-right:  $z_{\text{int\_sigma}} = 10$ ; bottom-left:  $L_{\text{cut}} = 0.001 L_*$ ; bottom-right:  $L_{\text{cut}} = 1 L_*$ .

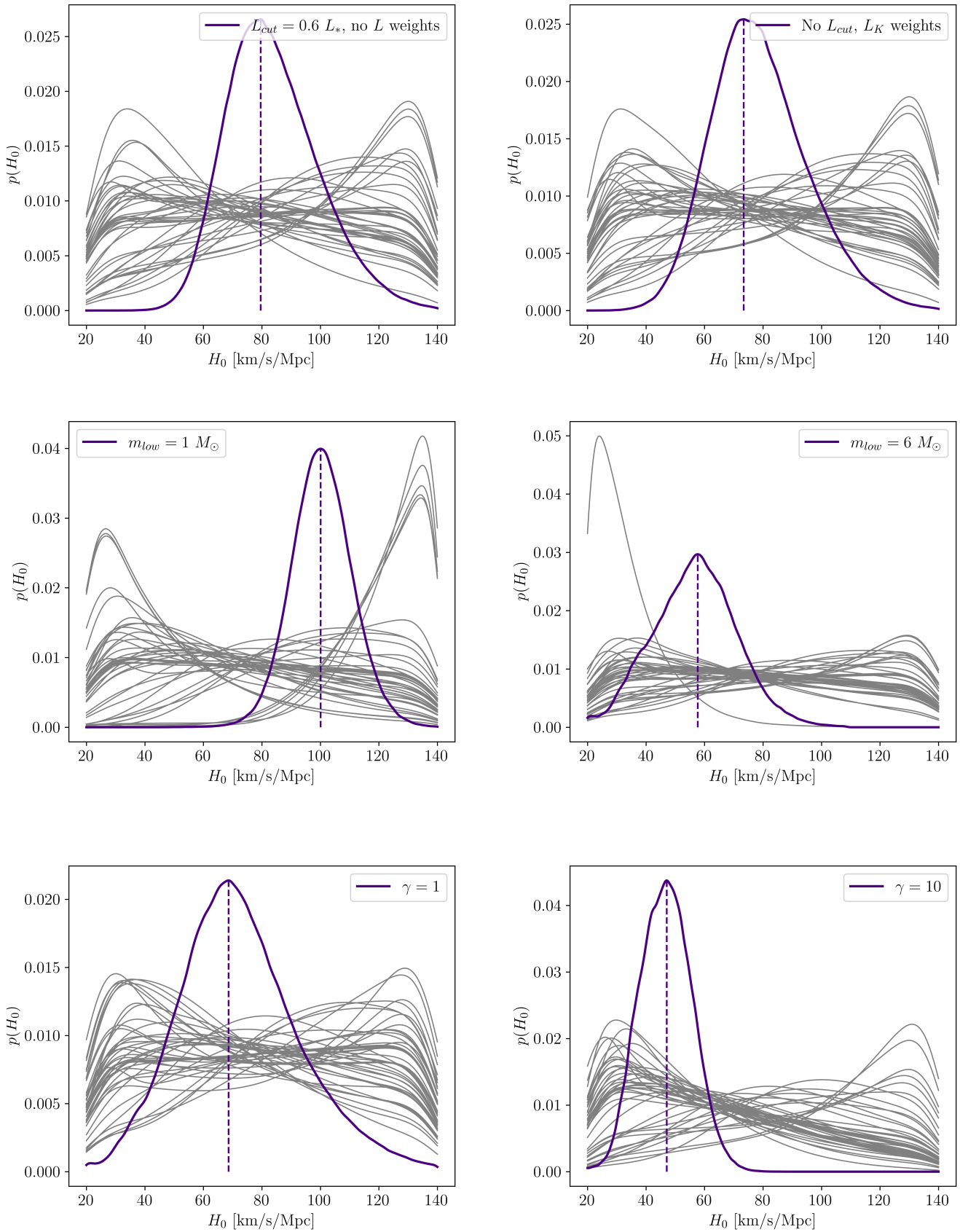


**Figure 3.11:** Set of four tests performed on the parameters used to compute the combined  $H_0$  posterior starting from a set of 42 BBH events. Top-left:  $L_{cut} = 0.6 L_*$ , no luminosity weighting; top-right: K-band luminosity weighting, no  $L_{cut}$ ; center-left:  $m_{low} = 1 M_\odot$ ; center-right:  $m_{low} = 6 M_\odot$ ; bottom-left:  $\gamma = 1$ ; bottom-right:  $\gamma = 10$ .

### 3.2.2 Full MCMC analysis

Monte Carlo methods refer, in general, to a series of mathematical techniques used to sample unknown or complex distributions of variables by simulating random processes. In a Bayesian framework, this means sampling from distributions in the form

$$f(\theta|d) = p(\theta)p(d|\theta). \quad (3.3)$$

Markov Chain Monte Carlo analyses (or MCMCs), in particular, do so by applying changes to an arbitrary initial state chosen for a given variable following an assumed prior distribution for it (in our case we deal with uniform distributions); the sampling is done recursively, which means that the  $n^{\text{th}}$  iteration of the sampling process is only dependent on the  $(n - 1)^{\text{th}}$  and independent of the initial state. The variable space in which a *sampler* can move is discretized in a number of *steps*, and the sampling process can be run in parallel on a set of *walkers*. This type of algorithm is implemented in CHIMERA in the `MCMC.py` module, which makes use of the `emcee` Python package released by Foreman-Mackey et al. 2013. In order to produce posterior samples for a number of different variables instead of a single one, the `HyperLike` class in the `Likelihood.py` module must be used, for which the necessary recipe contains the parameters used both for the `LikeNumeratorLVK` class and the `Bias` class (see Table 2.3 and eq. 2.1). As for the initialization of the MCMC instance, the requirements are shown in Table 3.7, together with a short description. This analysis produces the results for a combination of the cosmological ( $H_0$ ) and astrophysical parameters presented in section 1.5.

The ones that follow are the results obtained from an MCMC run on the sample of 42 BBH events used in the previous section. The prior ranges and initial values for each parameter in analysis are displayed in Table 3.8 and coincide with the choices made by Gray, R et al. 2023 for their joint cosmology and population analysis (exception made for  $H_0$ 's prior range, which we set to  $[20, 200] \text{ km/s/Mpc}$ ); as for the MCMC sampler settings, they are listed in Table 3.9.

Figure A.4 (Appendix A) shows the distributions of all the parameters in analysis and their 1-D posterior probabilities in a corner plot with a completeness interpolant computed on an  $L_{\text{cut}}$  parameter equal to  $0.02 L_*$ .

The  $H_0$  posterior can be analyzed in detail in Figure 3.14 and compared to the results found in Gray, R et al. 2023: our posterior sample distribution has a median value of  $H_0 = 76^{+52.16}_{-33.03} \text{ km/s/Mpc}$ , while the latter peaks at  $H_0 = 33^{+51}_{-18} \text{ km/s/Mpc}$ . Choosing the maximum-a-posteriori distribution obtained for each parameter (which is the case in Gray, R et al. 2023's work) can differ from the posterior probability obtained by marginalizing over the other parameters and may lead to discrepancies (Raveri, Doux, and Pandey 2024): for this reason, we decide to keep the median value of the posterior as representative of the distribution. The full list of parameter medians that resulted from the MCMC run can be found in Table 3.6.

The final result in Figure 3.12 shows the combined posterior (with a smoothing factor equal to 0.2) obtained both through our sample of BBH events (orange line) and the two significant GW events GW170817 (BNS, pink line) and GW190814 (NSBH, red line), the last two for fixed population parameters. GW170817's  $H_0$  posterior is re-computed with the same likelihood parameters as the other events (an  $H_0$  prior grid equal to  $[20, 140]$  and  $L_{\text{cut}} = 0.6 L_*$ ): this results in a constraint at  $H_0 = 77^{+24}_{-11} \text{ km/s/Mpc}$ . Our full posterior, for which  $H_0 = 74^{+15}_{-7} \text{ km/s/Mpc}$ , can be compared to a similar result found in Gray, R et al. 2023, Figure 3.13, with the second being constrained at  $H_0 = 65^{+12}_{-4} \text{ km/s/Mpc}$  for a posterior smoothing factor equal to 0.2: the two results appear to be in good agreement within the errors. GW170817's  $H_0$  constraint alone is characterized by a maximum error of  $\simeq 31\%$ , whereas GW190814's is of the order of  $70\%$ . The marginalized BBH analysis produces errors  $< 68\%$ , but the true significance of the dark siren approach is apparent from the combination of all three cases, which results in an error of the order of  $< 23\%$ .

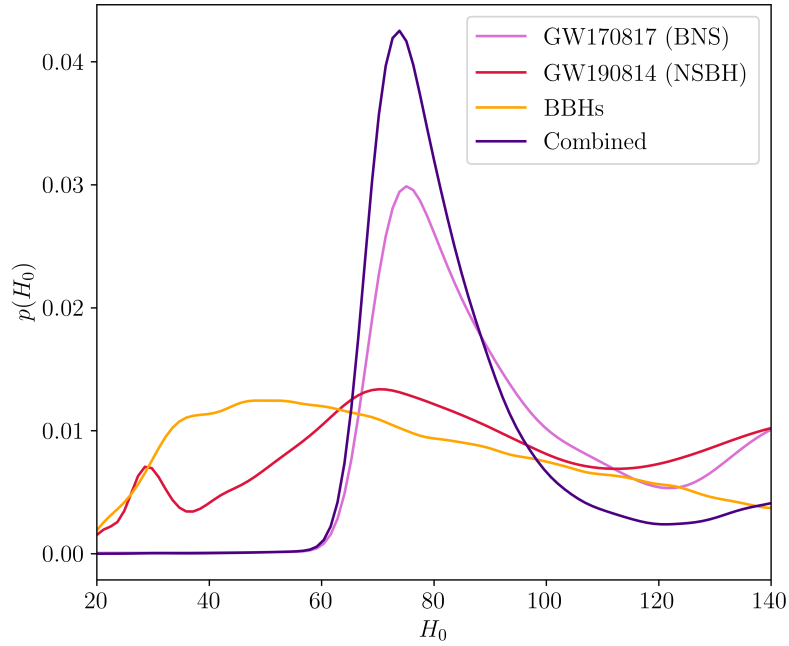


**Figure 3.12:**  $H_0$  combined posterior distribution (violet) obtained with a set of 42 BBH events by marginalizing over all population parameters with the addition of the NSBH event GW190814 and the BNS event GW170817, which were instead computed with fixed population assumptions. In orange, the combined BBH posterior (which does not include GW190814 and GW170817); in red, GW190814's posterior; in pink, GW170817's posterior. The bias term is calculated using O3 injection data and a completeness interpolant computed with  $L_{thr} = 0.02 L_*$  is used.

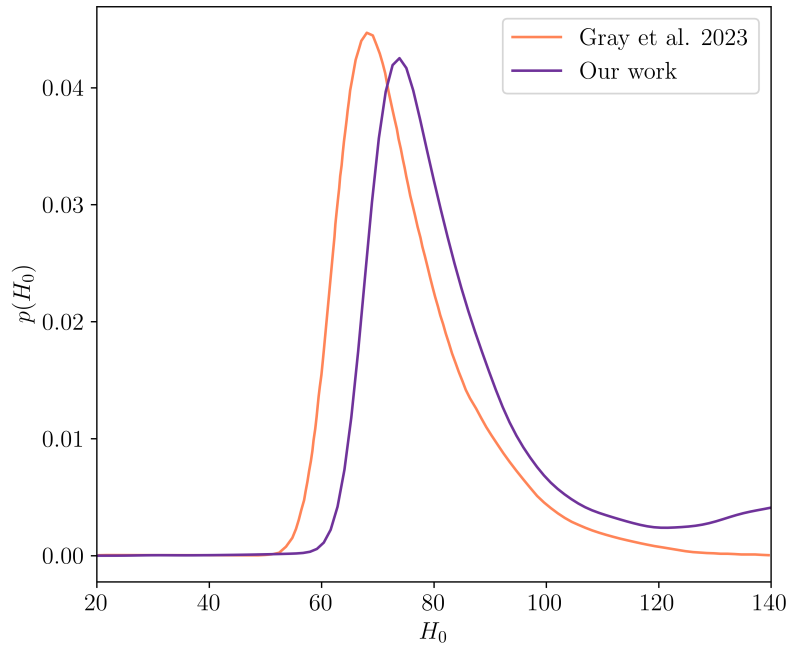


**Figure 3.13:** Combined posteriors obtained with a set of 42 BBH events (whose posterior was marginalized over all population parameters) and a selection of non-BBH events. In our case (violet), GW170817 and GW190814 were added to the combined posterior; in Gray, R et al. 2023's case (orange), all NSBH events, together with GW170817, were added to the combined posterior. Gray, R et al. 2023's results were taken from [https://git.ligo.org/rachel.gray/gwcosmo-cosmo-pop-method-paper/-/tree/main/data/BBH/catalog?ref\\_type=heads](https://git.ligo.org/rachel.gray/gwcosmo-cosmo-pop-method-paper/-/tree/main/data/BBH/catalog?ref_type=heads) and [https://git.ligo.org/rachel.gray/gwcosmo-cosmo-pop-method-paper/-/tree/main/data/NSBH?ref\\_type=heads](https://git.ligo.org/rachel.gray/gwcosmo-cosmo-pop-method-paper/-/tree/main/data/NSBH?ref_type=heads).

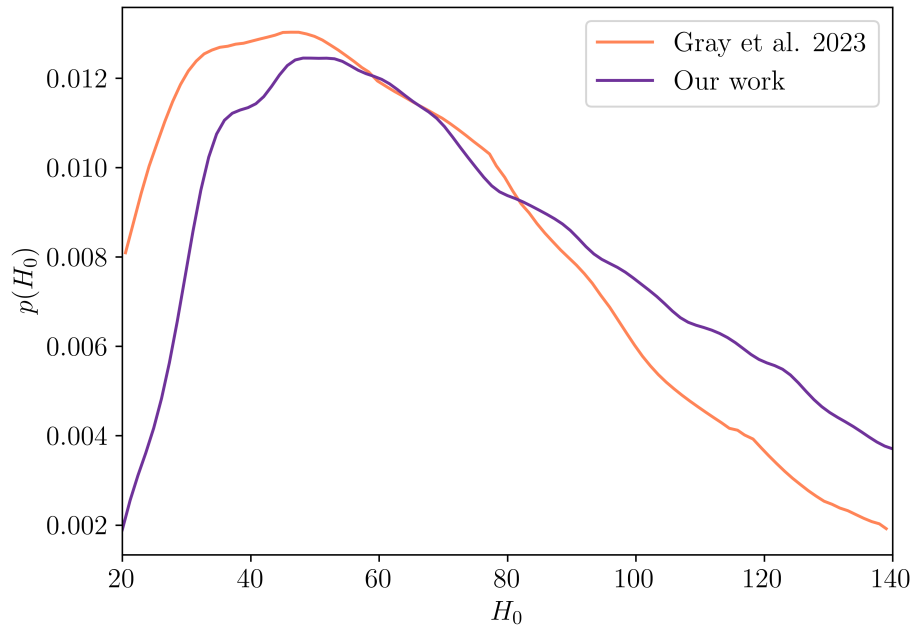


**Figure 3.14:**  $H_0$  posterior distribution resulting from an MCMC run on 42 BBH events. Our posterior (violet) is compared to the result obtained by Gray, R et al. 2023 (orange). Gray, R et al. 2023's results were taken from [https://git.ligo.org/rachel.gray/gwcosmo-cosmo-pop-method-paper/-/tree/main/data/BBH/catalog?ref\\_type=heads](https://git.ligo.org/rachel.gray/gwcosmo-cosmo-pop-method-paper/-/tree/main/data/BBH/catalog?ref_type=heads).

### The $H_0 - \mu_g$ and $H_0 - \gamma$ anti-correlations

With Figure 3.15, we focus on three specific parameters constrained in the MCMC analysis, which were extracted from the full distribution shown in Figure A.4. In particular, we focus on the parameters showing the more significant dependence on  $H_0$  as to explore possible correlations between them.

The anti-correlation between  $\mu_g$  and  $H_0$ , which was already anticipated when analyzing the 1-D  $H_0$  posterior for varying values of  $m_{low}$ , can be observed in Figure 3.15 and justified if one considers the mass-redshift degeneracy mentioned in Chapter 1 (equation 1.44), which stands at the core of the dark siren method (Borghi, Mancarella, Moresco, et al. 2024): in the absence of high redshift accuracy for a given sample of events, the different values  $H_0$  can play a role in determining their redshift at fixed values of  $d_L$  (see equation 1.45). For instance, a larger  $H_0$  results in a lower  $\mu_g$ , hence the anti-correlation in Figure 3.15 (already commented on in the work by Borghi et al. (2023)). This anti-correlation is reflected onto the results obtained in section 4.1; setting  $m_{low}$  to a larger value results in an  $H_0$  posterior peak at lower values, as visible in Figure 3.11 (top-right): this happens because excluding low-mass samples moves the model's 'peak' (the primary mass's gaussian component's peak,  $\mu_g$ ) to larger values, thereby shifting the  $H_0$  peak towards lower ones. As for  $\gamma$ , a similar anti-correlation is found; if one looks at equation 1.63, the terms  $(1+z)^\gamma$  at the numerator and  $(\frac{1+z}{1+z_p})^{\gamma+\kappa}$  at the denominator determine the presence of degeneracy between the  $H_0$  and  $\gamma$  regardless of the changes in  $z_p$  and  $\kappa$ ; the reason behind this is similar to the one explained with regards to the  $H_0 - \mu_g$  anti-correlation: a large  $H_0$  coupled with a low  $\gamma$  can produce the same results as a low  $H_0$  coupled with a large  $\gamma$ , on the account of the relation that runs between  $H_0$  and redshift; when lower  $H_0$  values decrease the redshifts and make them incompatible with the mass distribution,  $\gamma$  becomes larger to compensate for this effect (as noted in Abbott, R. et al. 2023a's work (2023)); the opposite is then also true: increasing  $\gamma$  causes a decrease in  $H_0$ .

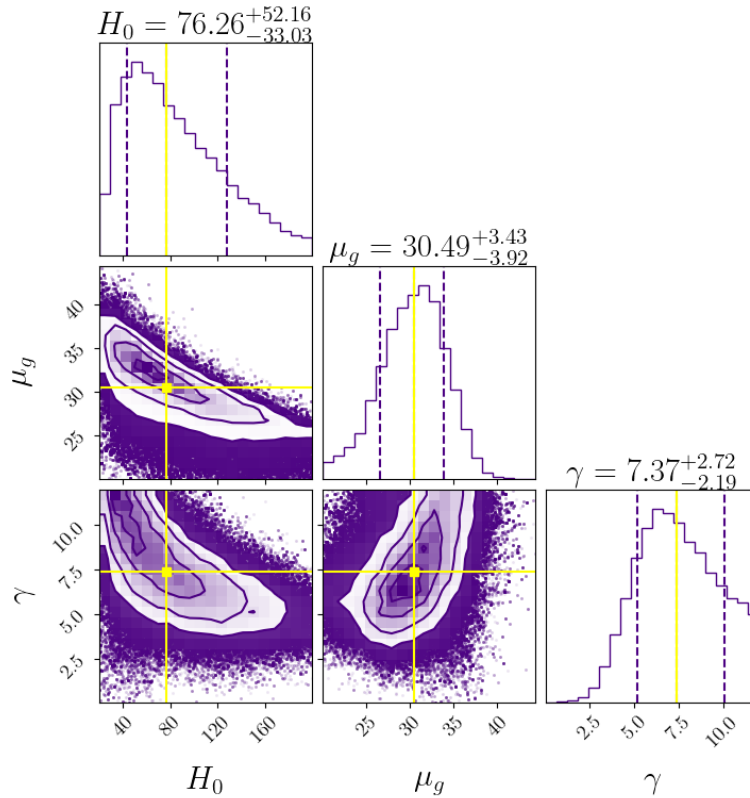


**Figure 3.15:** 2-D contours of the  $\mu_g$ ,  $\gamma$  and  $H_0$  parameter samples resulting from an MCMC run on 42 BBH events. The yellow lines identify the median values relative to the three parameters' distributions, namely  $76.26 \text{ km/s/Mpc}$  for  $H_0$ ,  $30.49 M_\odot$  for  $\mu_g$  and  $7.37$  for  $\gamma$  (the uncertainties were neglected to plot the lines).

### O4 and O5 run predictions

The analysis we performed using data extracted from the O1, O2 and O3 runs of the LVK detector network highlights the need for a larger number of detected events (to raise the statistical relevance of the results) at larger distances, together with lower  $d_L$  uncertainties and smaller localization areas (to provide more stringent constraints of the galaxies that are selected to compute the likelihood term and remove the degeneracies that were identified between  $H_0$  and the  $\mu_g$  and  $\gamma$  parameters). The next runs of the LVK detector network will present improvements on these fronts, specifically the O4 run, which began in May of 2023 and is set to end in October of 2025, together with O5, which is programmed to operate between 2026 and 2028. The properties of the signals that will result from these upcoming runs can be simulated; this was done, for instance, in the work by Iacovelli et al. 2022, in which the GFAST software was used to predict the capabilities of the LVK detector network during the O4 run, together with the possible addition of the Einstein Telescope (ET) and Cosmic Explorer (CE).

According to the work by Borghi et al (2023), using GFAST to simulate two sets of events measured during the O4 and O5 runs returns  $\approx 100$  events with  $\text{SNR} > 12$  and  $\approx 100$  events with  $\text{SNR} > 25$  respectively; the addition of the Einstein Telescope to O4's estimates would further increase the constraining power of the GW signals, with a predicted  $\approx 100$  events with  $\text{SNR} > 100$  (according to Iacovelli et al. 2022's work).

Table 3.6. Medians of the distributions of the 12 parameters analyzed during an MCMC run on a set of 42 BBHs. See sections 1.1 and 1.6 for definitions of the parameters.

Parameter	Median of the resulting distribution
$H_0$ [km/s/Mpc]	$76.36^{+52.16}_{-33.03}$
$\lambda_p$	$0.04^{+0.04}_{-0.02}$
$\alpha$	$3.68^{+0.50}_{-0.46}$
$\beta$	$0.15^{+1.21}_{-0.95}$
$\delta_m$	$4.51^{+2.27}_{-2.56}$
$m_{low}$ [ $M_\odot$ ]	$4.92^{+0.74}_{-0.85}$
$m_{high}$ [ $M_\odot$ ]	$124.71^{+30.03}_{-41.66}$
$\mu_g$ [ $M_\odot$ ]	$30.49^{+3.43}_{-3.92}$
$\sigma_g$	$3.14^{+3.36}_{-1.87}$
$\gamma$	$7.37^{+2.72}_{-2.19}$
$\kappa$	$2.98^{+2.04}_{-2.00}$
$z_p$	$2.54^{+0.98}_{-1.07}$

Table 3.7. Parameters used for the initialization of the MCMC class in CHIMERA.

Parameter	Description
sampler	sampler algorithm
use_joblib	option to use the joblib package
use_mpi	option to run the MCMC on multiple tasks with MPI
nsteps	number of MCMC steps
nwalkers	number of MCMC walkers
output_dir	output directory for the MCMC results
restart_chain	option to restart the MCMC from an existing file
chain_prefix	file name prefix
hyper_model	HyperLike instance
priors	prior ranges relative to the different parameters
prior_kind	type of prior range (e.g. flat)
initial_state_distribution	assumed distribution type for the given parameters
gaussian_bests	gaussian best values to generate the initial parameter distributions
gaussian_sigmas	together with gaussian_bests, used to generate the initial parameter distributions

Table 3.8. Parameter priors and initial values used to run the MCMC analyses on a sample of 42 BBHs. See sections 1.1 and 1.6 for definitions of the parameters.

Parameter	Prior range (priors)	Initial value (gaussian_bests)
$H_0$ [km/s/Mpc]	[20, 200]	70.
$\lambda_p$	[0.01, 0.99]	0.03
$\alpha$	[1.5, 12]	3.78
$\beta$	[-4, 12]	0.81
$\delta_m$	[0.01, 10]	4.8
$m_{low}$ [ $M_\odot$ ]	[2, 10]	4.98
$m_{high}$ [ $M_\odot$ ]	[50, 200]	112.5
$\mu_g$ [ $M_\odot$ ]	[20, 50]	32.37
$\sigma_g$	[0.4, 10]	3.88
$\gamma$	[0, 12]	4.59
$\kappa$	[0, 6]	2.86
$z_p$	[0, 4]	2.47

Table 3.9. Parameters used for the MCMC analysis with CHIMERA.

Parameter	Description
sampler	emcee
use_joblib	False
use_mpi pool	True
nsteps	10000
nwalkers	56
restart_chain	False
prior_kind	flat
initial_state_distribution	truncgauss (truncated gaussian distribution)
gaussian_sigmas	prior range difference -0.05

# Chapter 4

## Conclusions and Future Prospects

The introduction of the  $\Lambda$ CDM model in Cosmology allowed for the successful description of many features of the observable Universe. During the last few decades, however, many issues have arisen from the application of said framework: starting from the accelerated expansion of the Universe observed in Riess, Adam G. et al. 1998, in fact, two main components in the energetic budget of the Universe have been identified, with Dark Energy (DE) constituting its largest portion despite it not having been identified yet. As for the second largest component, Dark Matter (DM), the majority of its gravitational contribution is still unknown.

Various methods have been developed to allow for a precise measurement of these components, such as the use of Type Ia Supernovae and the Cosmic Microwave Background (CMB) to accurately quantify cosmic distances (which are necessary for this purpose). With the increase in accuracy, these methods have consistently shown discrepancies in inferred values of a variety of cosmological parameters, with the most controversial being the *Hubble tension*, for which consistently different values of the local expansion rate of the Universe ( $H_0$ ) are found. This is particularly interesting, as it could lead to the discovery of unforeseen systematic errors in one of the current methods, or even new physics.

For these reasons, the research into new *cosmological probes* has proven itself to be pivotal to determine the possible origins of such discrepancies.

Gravitational waves are among the most promising emerging cosmological probes, as they provide independent luminosity distance measurements which rely only on GR, without the need for external calibrators (as is the case for standard candles like SNe); therefore, they can provide an independent measurement of the expansion history of the Universe. In particular, the merger of two compact objects like black holes and/or neutron stars generates a signal that, when detected, can provide a measurement of the source's luminosity distance from the observer; this can allow us to use GWs as *standard sirens*. This method, however, does not come without its caveats: the luminosity distance information that can be gathered from such signals features a degeneracy with the redshift that appears alongside it in the signal's expression. In order to break this degeneracy, different approaches have been identified, with the *bright siren*, *dark siren* and *spectral siren* cases being the most notable. The dark siren approach, in particular, allows for the determination of a GW source's redshift by means of a galaxy catalog that covers its signal's localization area: the most likely hosts are identified through *Bayesian* statistical inference and assigned to the event together with their redshift information. The implementation of a galaxy catalog must account for its accuracies and limitations in its redshift distribution and sky coverage: failing to do so when working in a Bayesian framework is likely to result in the presence of significant measurement biases.

The main goal of my work was the successful introduction of real galaxy and gravitational wave data to the Bayesian statistical framework used to produce inferences of cosmological and astrophysical parameters with a dark siren approach. More specifically, I focused on the correct modeling of the galaxy catalog's incompleteness at higher redshifts with the goal of removing any possible biases that might have otherwise resulted from it.

I added the resulting corrective terms to CHIMERA (Borghi, Mancarella, Moresco, et al. 2024), a novel Python code that can be used to produce joint cosmological-population statistical inferences through a Bayesian framework, which was previously limited to the analysis of mock galaxy and gravitational wave catalogs.

The results of my work can be articulated in the following three points:

1. **Quantitative analysis of the galaxy and gravitational wave catalogs** - The use of real catalogs of data required an in-depth analysis of their components. For what pertains the galaxy catalog, I based my work on GLADE+ (Dály, G. et al. 2022); the redshift distribution of its elements shows its limitations at high redshift, together with its heterogeneity on the sky plane: GLADE+ is, in fact, the product of a combination of various sub-catalogs which are not uniformly distributed, not in redshift nor on the sky plane. Together with this, the errors associated to the redshift measurements are themselves heterogeneous and differ depending on the sub-catalog of origin. Modeling the catalog's distribution is therefore pivotal in order to effectively use it for the production of statistical inferences. As for the GW data, I used the GWTC-3 gravitational wave catalog (Abbott, R. et al. 2023a, Abbott, R. et al. 2023b), for which I developed a new portion of the code (`GW_stats`) that allows for the computation of a given gravitational wave event's localization volume among other features;
2. **Extending the bayesian framework to account for the galaxy catalog's incompleteness** - To properly include a realistic galaxy catalog in the analysis done with the Bayesian framework, two different effects need to be included, which are crucial to obtain robust and unbiased measurements with real data:
  - a **completeness correction**, which accounts for the fact that our galaxy catalog is likely incomplete at high redshifts and is not representative of the actual distribution of all galaxies in the Universe; by failing to acknowledge this, the galaxies associated to a given GW event would only be a sub-sample of the underlying distribution, thus resulting in the introduction of a bias. In order to correctly compensate for this effect, I modeled the galaxy catalog's incompleteness at higher redshifts;
  - **luminosity weighting and cuts**: since not all galaxies within a catalog are equally likely to host a GW event, they can be weighted or removed depending on some criteria. The most commonly used one is based on the introduction of a probability weight proportional to the luminosity of the galaxy, since more luminous and massive galaxies can be thought to be more likely to host compact objects like BBHs or BNSs.

To account for these effects, I updated different areas of the code to compute *completeness interpolants*, which are functions that define a galaxy catalog's level of completeness as a function of redshift, and a catalog's *completeness fraction*. Together with these, I introduced luminosity weighting to account for how likely a given galaxy can be considered to host a CBC merger event. These terms can be computed with a variety of different assumptions and choices, for which I conducted a number of tests. The analysis conducted in this work is based on a selection of completeness and luminosity weighting

parameters that allow for the comparison of our results to those found in the existing literature.

A visual representation of the completeness interpolant as a function of redshift is shown in Figure 4.1, where an average  $P_{compl}$  is computed over the entire sky area and is shown in black: the function starts decreasing as the completeness of the catalog becomes lower. The criterion used to determine when that happens is chosen as the luminosity density of the catalog, which is computed starting from a luminosity threshold  $L_{thr} = 0.02 L_*$ , where  $L_*$  is the knee of the Schechter function used to describe the distribution of the galaxies in luminosity.

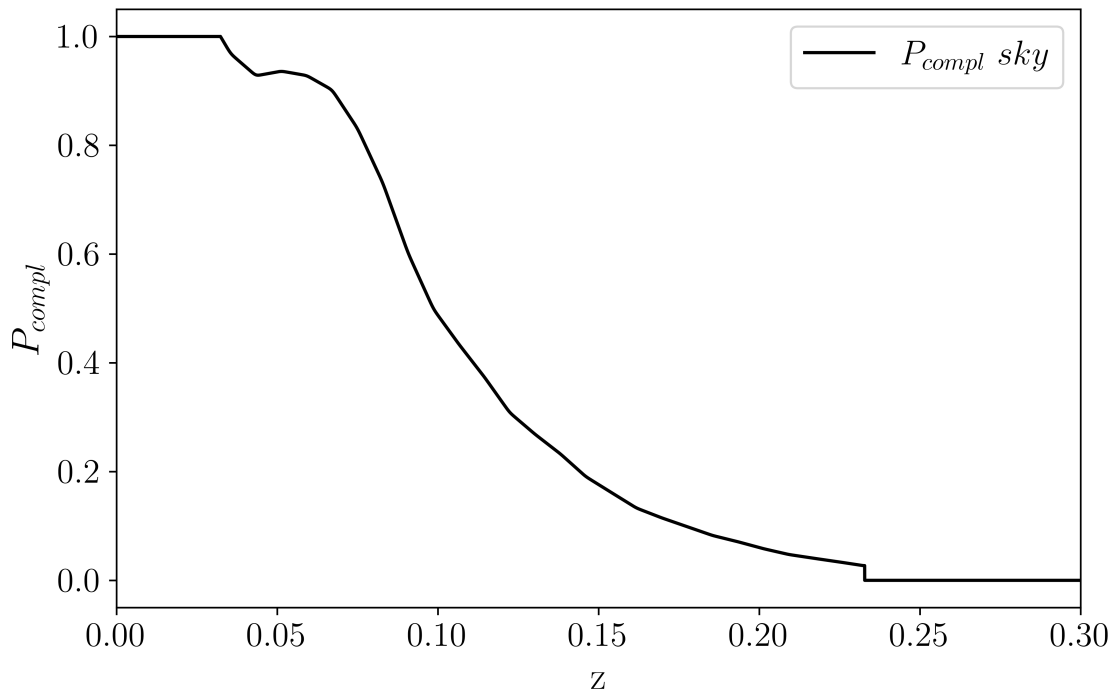


**Figure 4.1:** Completeness interpolant  $P_{compl}$  computed on the entire sky area by using a criterion based on the luminosity density of the galaxy catalog. Said luminosity density is computed starting from a threshold luminosity of  $L_{thr} = 0.02 L_*$ , where  $L_*$  is the knee of the Schechter function used to describe the distribution of the galaxies in luminosity.

3. **First application of the new framework to real data** - I used the newly updated framework of the CHIMERA code to analyze and produce statistical inferences using the catalogs that I analyzed above. In particular, to properly test and validate the new pipeline, I followed these steps.;

- I started from the analysis of two well-localized GW events, GW170817 and GW190814, that I used as test cases. The first one represents a case of Binary Neutron Star event, while the second is an example of a Neutron Star-Black Hole merger. These two case studies were used to produce statistical inferences on the  $H_0$  parameter alone in a dark siren framework, whereas all other astrophysical parameters were fixed; the selection of these two events in particular also depended on their localization in the sky: whereas GW170817 is localized in a small area that is well-covered by the galaxy catalog, such is not the case for GW190814 which is located on a larger area and is therefore more susceptible to the effects of catalog incompleteness. The result I obtained for

GW170817 on  $H_0$  was used to determine the robustness of the framework and compared to the one obtained by M. Fishbach et al. 2019 since it was made with a similar set of likelihood and bias parameter choices. We find that our result is consistent with theirs within  $\approx 0.03 \sigma$ . As for the second event, the population models and parameters used by Gray, R et al. 2023 resulted in an  $H_0$  peak at  $H_0 = 71_{-19}^{+50} \text{ km/s/Mpc}$ , which is consistent with their result within  $\approx 0.05 \sigma$ . GW190814 in particular was used to perform tests on possible systematic effects: different choices for the luminosity cuts and weights applied to the galaxies in the catalog were applied and resulted in different posterior shapes. I find that applying more stringent luminosity cuts on the catalog results in a decrease of the probability at lower values of  $H_0$ , which is also the case when no luminosity weighting is applied. Widening the redshift grid on which the  $H_0$  posterior probability is computed, on the other hand, does not show meaningful differences for GW190814: this is probably indicative of the fact that the addition of a larger number of galaxies into its calculation is not impactful for this event;

- I further tested the performance of the code by conducting a statistical inference of the  $H_0$  parameter with fixed population assumptions on a set of 42 BBH events extracted from the GWTC-3 catalog that represent the best sample of GW events available to date; this set has also been previously analyzed by Gray, R et al. 2023 and Abbott, R. et al. 2023a. An event-by-event posterior comparison shows good agreement between our results and those found by Gray, R et al. 2023, except for some minor differences at low  $H_0$  which seem to impact the peak of the combined posterior probability. The one obtained with the same parameters used by Gray, R et al. 2023, in fact, shows a peak at  $H_0 = 76_{-15}^{+18} \text{ km/s/Mpc}$ , which is consistent with Gray, R et al. 2023's within  $\approx 0.6 \sigma$ . I tested the sample of BBHs on the same set of possible systematic effects as was done for GW190814: ignoring the completeness correction heavily impacts the resulting posterior, whose peak is shifted to the lower boundary of the  $H_0$  grid (at  $H_0 = 20_{-0}^{+1} \text{ km/s/Mpc}$ ); this is because the selected sample of GW events extends to larger redshifts, for which the incompleteness of the catalog becomes manifest. Different cuts in luminosity also produce minor effects, justifiable for the same reasons given for GW190814. The absence of galaxy weighting is instead shown to result in more prominent differences: the combined posterior computed without weighting the galaxies in K-band luminosity peaks at  $H_0 = 79_{-14}^{+17} \text{ km/s/Mpc}$ , whereas weighting alone moves the peak at  $H_0 = 73_{-13}^{+19} \text{ km/s/Mpc}$ . In addition to these tests, I also analyzed the effects of different choices for the  $m_{low}$  and  $\gamma$  population parameters and found apparent anti-correlations between them and the peak of the  $H_0$  posterior distribution; these effects were further discussed in the joint cosmological-population section of the work;
- finally, I performed a complete joint fit of the cosmological and astrophysical parameters that can be obtained from the sample of 42 BBH events described above with a MCMC analysis. This allowed me to properly assess the error associated to the Hubble constant when the astrophysical parameters of the BBH populations are also allowed to vary; the results highlighted the apparent anti-correlation trends that run between  $H_0$  and the two population parameters  $m_{low}$  and  $\gamma$ . These effects are discussed and justified in the context of redshift degeneracies: for what concerns  $m_{low}$ , setting it to a lower value causes changes in the shape of the mass model, whose gaussian component's peak ( $\mu_g$ ) is also shifted to lower values. Since a degeneracy exists between the redshift and the source-frame masses of the objects in a binary system, a lower value for the source-frame mass can produce the same detector-frame mass if the redshift moves to

larger values: this causes the  $H_0$  parameter to move to larger values as well. A similar type of degeneracy exists in the CBC merger rate model between the  $\gamma$  parameter and the redshift. As for the marginalized  $H_0$  posterior alone, it is found to peak at  $H_0 = 76.26^{+52.16}_{-33.03} \text{ km/s/Mpc}$ .

In Figure 4.2 I present the full  $H_0$  posterior obtained by marginalizing over all population parameters for the BBH sample and combining it with the posteriors relative to GW170817 and GW190814 (the last two were computed by fixing the population parameters), from which I find  $H_0 = 74^{+15}_{-17} \text{ km/s/Mpc}$ . This result can be compared to a similar one obtained by Gray, R et al. 2023, which peaks at  $H_0 \simeq 65^{+12}_{-4} \text{ km/s/Mpc}$  with a smoothing factor of 0.2 and is consistent with ours within  $\simeq 0.7 \sigma$ . Together with the posteriors, Figure 4.2 shows the range of  $H_0$  found by Aghanim, N. et al. 2020 (green) and the one found by Riess, Adam G. et al. 2022 (blue).

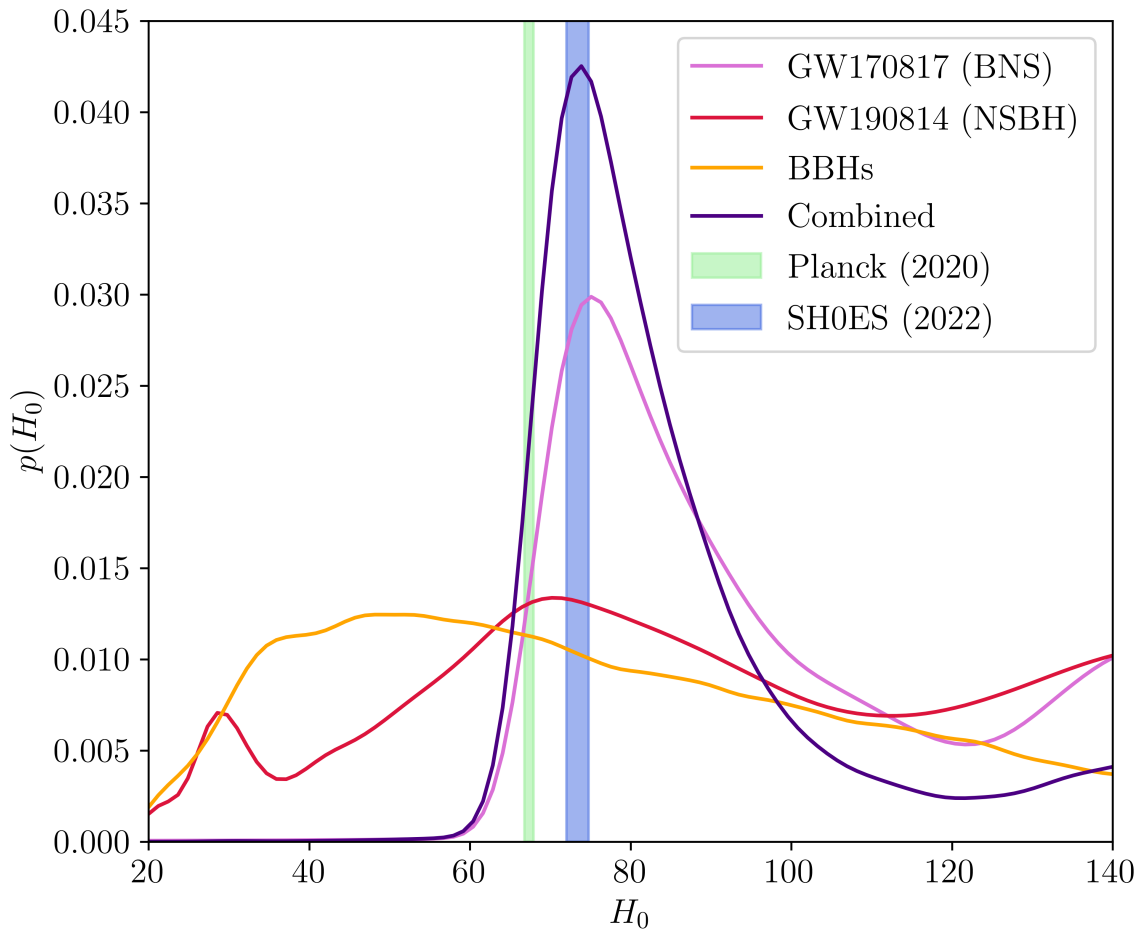


**Figure 4.2:**  $H_0$  combined posterior distribution obtained with a set of 42 BBH events by marginalizing over all population parameters, with the addition of the NSBH event GW190814 and the BNS event GW170817. The plot features: the combined posterior (including GW190814 and GW170817 at fixed population parameters) in violet, the marginalized combined BBH posterior (which does not include GW190814 and GW170817) in orange, GW190814's posterior in red and GW170817's posterior in pink. The green area represents the range of  $H_0$  found by Aghanim, N. et al. 2020, while the blue area represents the one found by Riess, Adam G. et al. 2022.

The key take-away point of my work is the following: in order to successfully include real galaxy data in the statistical inference of cosmological and astrophysical parameters, one must accurately model the catalog's incompleteness at large redshift and account for the different results that may be obtained when applying different cuts or weights to it. In the case of well-localized events, for which less redshift information is necessary, the results may be better-constrained and less prone to these effects.

In order to do that, I extended the CHIMERA code in several areas, and my work enabled its first application to real GW and galaxy data. The cosmological and astrophysical parameter estimates I obtained are in good agreement with the ones featured in the existing literature by other groups, and my work fundamentally paved the way for the application of CHIMERA to the next generation of real GW data, generated both by LVK and future GW interferometers.

With regards to this last point, I present some of the possible future prospects related to my work:

- **The use of O4 and O5 gravitational wave data** - the increase in detector sensitivity and signal constraints, both in localization region and luminosity distance, will likely result in an improvement in the posterior results for the population and astrophysical parameters that characterize GW signals, together with the  $H_0$  cosmological parameter; O4 and O5 data will also probably require adapting the code to the analysis of larger datasets. The future addition of the **Einstein Telescope (ET)** (Branchesi et al. 2023) to the configuration could further increase the number of detected events to an estimated order of magnitude of  $10^4 - 10^5$  per year for BBH, NSBH and BNS events.
- **The use of a galaxy catalog other than GLADE+** - given that GLADE+ is limited to low redshift values, analyzing future data will require the use of a galaxy catalog that is more populated at higher redshifts; this is in anticipation of the larger distances at which future detector runs will be able to detect GW signals; a possible candidate for this role is the **Euclid** mission (Castander et al. 2024, Mellier et al. 2024), launched on July 1<sup>st</sup> 2023, which is set to operate for 6 years and provide data to build two surveys, the *Euclid Wide Survey* and the *Euclid Deep Survey*, for which the completeness correction would be estimated.
- **Extending CHIMERA to produce inferences of the  $\Omega_m$  parameter** - the results presented in this work were obtained by fixing all cosmological parameters except for  $H_0$ ; a possible improvement on this front would be extending the statistical analysis to the  $\Omega_m$  parameter, given that higher-quality gravitational wave and galaxy data could help break the degeneracy that exists between  $H_0$  and  $\Omega_m$ .

# Appendix A

## Additional plots

This appendix contains supplementary plots referenced in the main text that provide additional context to the primary findings of this Thesis.

### A.1 GWTC-3 BBH sample - mean properties

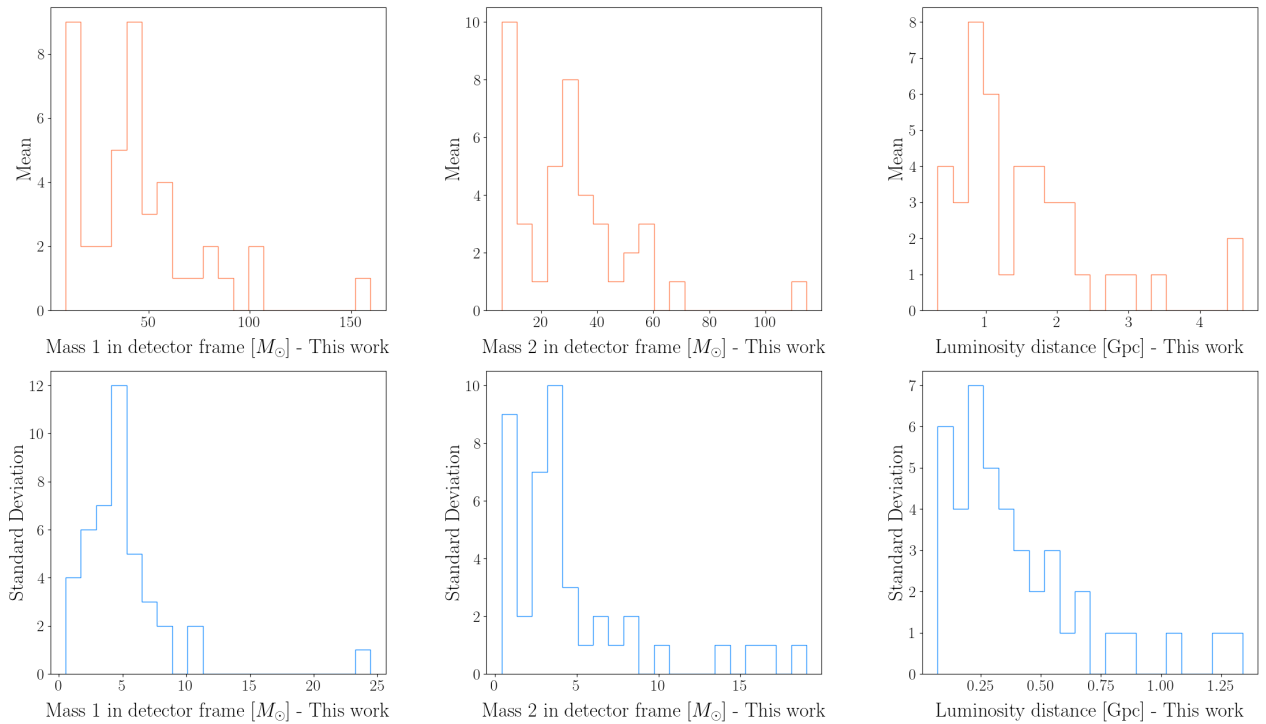


**Figure A.1:** Histograms produced using the set of 42 BBHs we selected from the second version of the available GWTC-3 data (Abbott, R. et al. 2023a) with a criterion of  $SNR > 11$  for the mass of the primary object  $m_1$ , the mass of the secondary object  $m_2$ , the values of luminosity distance  $d_L$  (first row) and relative uncertainties (second row)

## A.2 GWTC-3 BBH sample - posteriors KDEs

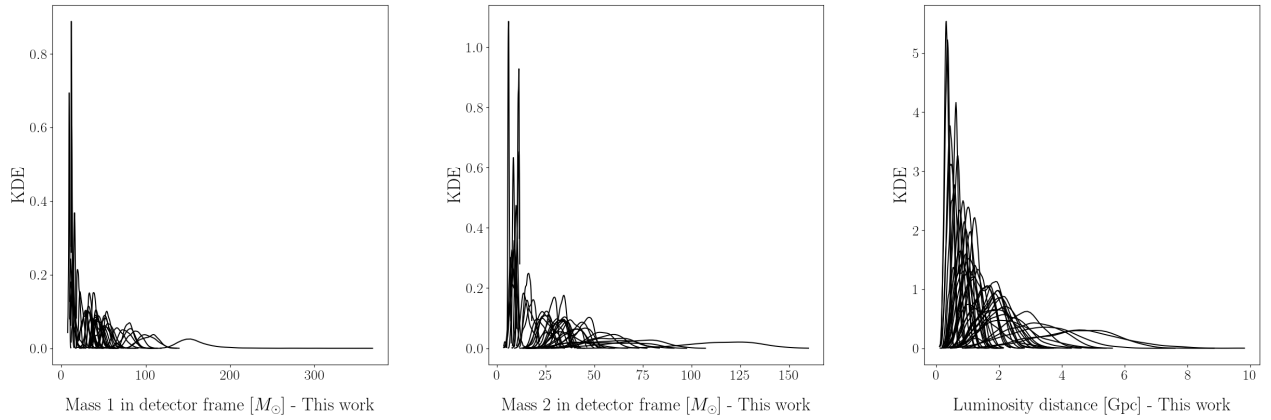


**Figure A.2:** PDFs produced using the set of 42 BBHs we selected from the second version of the available GWTC-3 data (Abbott, R. et al. 2023a) with a criterion of  $SNR > 11$  for the mass of the primary object  $m_1$ , the mass of the secondary object  $m_2$  and the luminosity distance  $d_L$ .

## A.3 PLPPLUSUNIF distribution

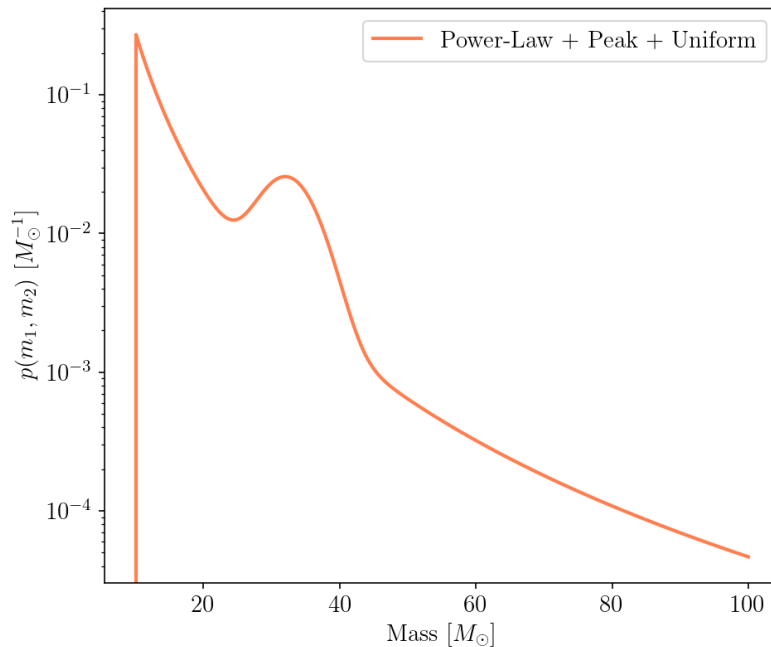


**Figure A.3:** The  $p(m_1, m_2) [M_{\odot}^{-1}]$  probability distribution obtained with a POWER-LAW PLUS PEAK PLUS UNIFORM distribution (Gray, R et al. 2023). The distribution is used to describe a population of Neutron Star-Black Hole binaries, where the NS's mass is computed in a range equal to  $[1, 3] M_{\odot}$  and the BH's mass is computed in a range equal to  $[10, 100] M_{\odot}$ .

## A.4 Full MCMC corner plot

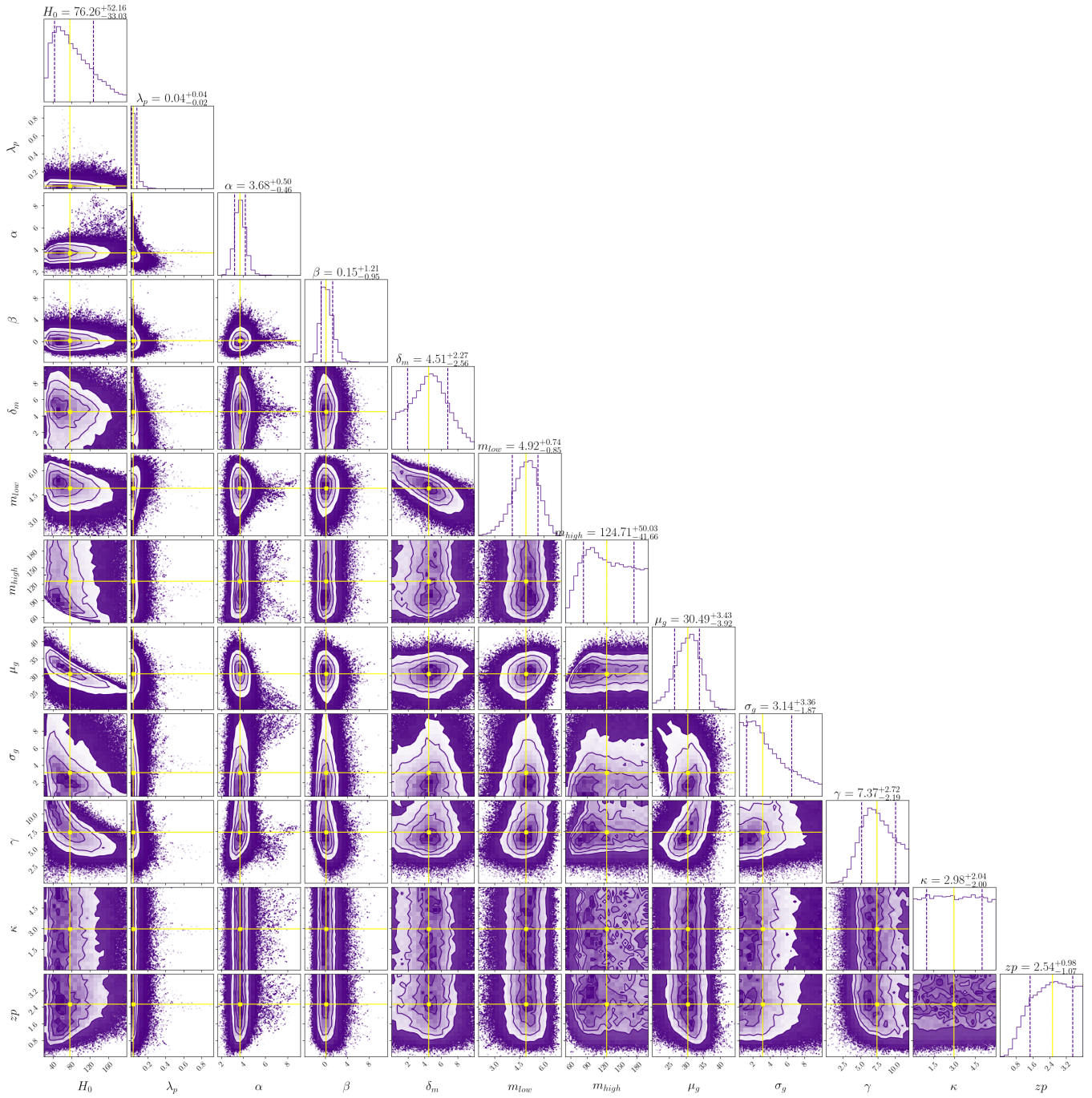


**Figure A.4:** Full corner plot resulting from an MCMC simulation run on a sample of 42 BBH events which returned posterior estimates for the following parameters:  $H_0$ ,  $\lambda_p$ ,  $\alpha$ ,  $\beta$ ,  $\delta_m$ ,  $m_{low}$ ,  $m_{high}$ ,  $\mu_g$ ,  $\sigma_g$ ,  $\gamma$ ,  $\kappa$ ,  $z_p$ . A completeness interpolant computed using  $L_{cut} = 0.02 L_*$  is used, together with an injection-bias term which used O3 run injection data. The MCMC simulation was run using 10000 steps and 56 walkers.

## A.5 MCMC step plots

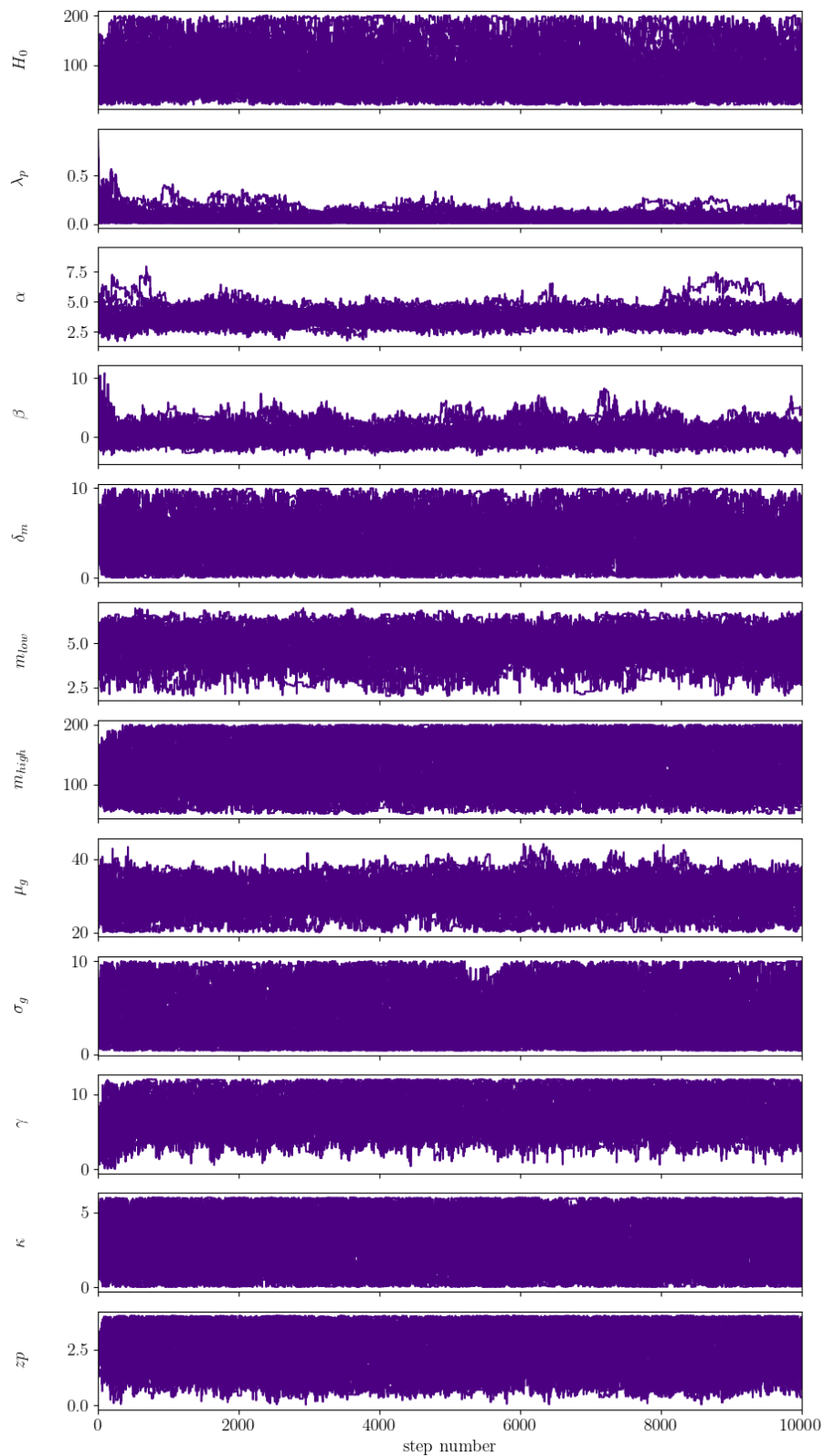


**Figure A.5:** Parameter - vs - step plot resulting from an MCMC simulation run on a sample of 42 BBH events which shows the evolution of the following parameters with increasing step number:  $H_0, \lambda_p, \alpha, \beta, \delta_m, m_{low}, m_{high}, \mu_g, \sigma_g, \gamma, \kappa, z_p$ . A completeness interpolant computed using  $L_{cut} = 0.02 L_*$  is used, together with an injection-bias term which used O3 run injection data. The MCMC simulation was run using 10000 steps and 56 walkers.

## A.6 GLADE+ weighted galaxy interpolant

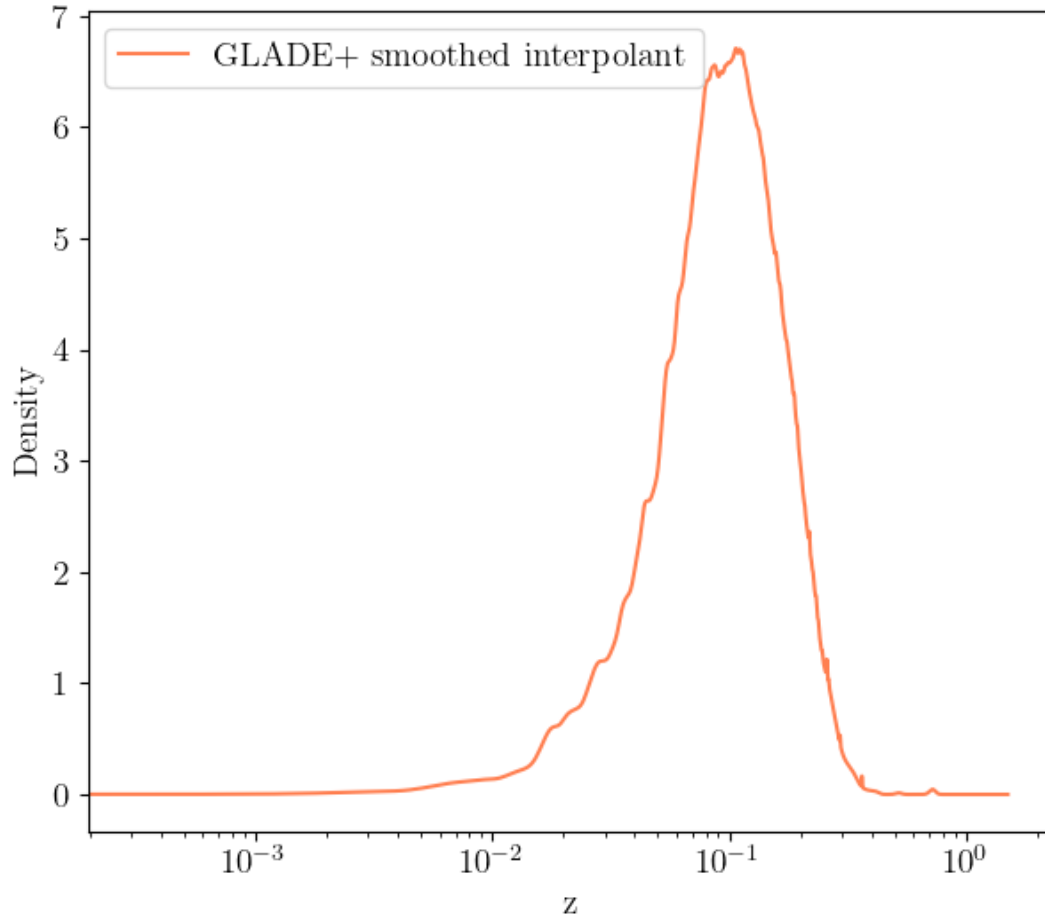


**Figure A.6:** GLADE+ smoothed interpolant computed on the same distribution (in orange) and weighted on the galaxies' K-band luminosity values. The x-axis, representing the redshift values, is shown in  $\log_{10}$  scale.

# Bibliography

- Aasi, J et al., The LIGO Scientific Collaboration (Mar. 2015). “Advanced LIGO”. In: *Classical and Quantum Gravity* 32.7, p. 074001. DOI: 10.1088/0264-9381/32/7/074001. URL: <https://dx.doi.org/10.1088/0264-9381/32/7/074001>.
- Abbott, B. P. et al. (Feb. 2016). “Observation of Gravitational Waves from a Binary Black Hole Merger”. In: *Phys. Rev. Lett.* 116 (6), p. 061102. DOI: 10.1103/PhysRevLett.116.061102. URL: <https://link.aps.org/doi/10.1103/PhysRevLett.116.061102>.
- Abbott, R. et al. (June 2020). “GW190814: Gravitational Waves from the Coalescence of a 23 Solar Mass Black Hole with a 2.6 Solar Mass Compact Object”. In: *The Astrophysical Journal Letters* 896.2, p. L44. DOI: 10.3847/2041-8213/ab960f. URL: <http://dx.doi.org/10.3847/2041-8213/ab960f>.
- Abbott, B. P. et al. (Oct. 2017a). “A gravitational-wave standard siren measurement of the Hubble constant”. In: *Nature* 551.7678, pp. 85–88. DOI: 10.1038/nature24471. URL: <http://dx.doi.org/10.1038/nature24471>.
- (Oct. 2017b). “GW170817: Observation of Gravitational Waves from a Binary Neutron Star Inspirals”. In: *Physical Review Letters* 119.16. DOI: 10.1103/physrevlett.119.161101. URL: <http://dx.doi.org/10.1103/PhysRevLett.119.161101>.
- Abbott, R. et al. (May 2021). “Population Properties of Compact Objects from the Second LIGO–Virgo Gravitational-Wave Transient Catalog”. In: *The Astrophysical Journal Letters* 913.1, p. L7. DOI: 10.3847/2041-8213/abe949. URL: <http://dx.doi.org/10.3847/2041-8213/abe949>.
- (June 2023a). “Constraints on the Cosmic Expansion History from GWTC–3”. In: *The Astrophysical Journal* 949.2, p. 76. DOI: 10.3847/1538-4357/ac74bb. URL: <https://link.aps.org/doi/10.1103/PhysRevX.13.011048>.
- (Dec. 2023b). “GWTC-3: Compact Binary Coalescences Observed by LIGO and Virgo during the Second Part of the Third Observing Run”. In: *Physical Review X* 13.4. DOI: 10.1103/physrevx.13.041039. URL: <http://dx.doi.org/10.1103/PhysRevX.13.041039>.
- Acernese, F et al. (Dec. 2014). “Advanced Virgo: a second-generation interferometric gravitational wave detector”. In: *Classical and Quantum Gravity* 32.2, p. 024001. DOI: 10.1088/0264-9381/32/2/024001. URL: <http://dx.doi.org/10.1088/0264-9381/32/2/024001>.
- Aghanim, N. et al., Planck Collaboration (Sept. 2020). “Planck2018 results: VI. Cosmological parameters”. In: *Astronomy and Astrophysics* 641, A6. DOI: 10.1051/0004-6361/201833910. URL: <http://dx.doi.org/10.1051/0004-6361/201833910>.
- Akutsu, T. et al. (Jan. 2019). “KAGRA: 2.5 generation interferometric gravitational wave detector”. In: *Nature Astronomy* 3.1, pp. 35–40. DOI: 10.1038/s41550-018-0658-y. URL: <http://dx.doi.org/10.1038/s41550-018-0658-y>.
- Belgacem, Enis et al. (July 2018). “Modified gravitational-wave propagation and standard sirens”. In: *Phys. Rev. D* 98 (2), p. 023510. DOI: 10.1103/PhysRevD.98.023510. URL: <https://link.aps.org/doi/10.1103/PhysRevD.98.023510>.

- Bera, Sayantani et al. (Oct. 2020). “Incompleteness Matters Not: Inference of  $H_0$  from Binary Black Hole–Galaxy Cross-correlations”. In: *The Astrophysical Journal* 902.1, p. 79. DOI: 10.3847/1538-4357/abb4e0. URL: <https://dx.doi.org/10.3847/1538-4357/abb4e0>.
- Bilicki, Maciej et al. (Dec. 2013). “TWO MICRON ALL SKY SURVEY PHOTOMETRIC REDSHIFT CATALOG: A COMPREHENSIVE THREE-DIMENSIONAL CENSUS OF THE WHOLE SKY”. In: *The Astrophysical Journal Supplement Series* 210.1, p. 9. DOI: 10.1088/0067-0049/210/1/9. URL: <http://dx.doi.org/10.1088/0067-0049/210/1/9>.
- Bilicki, M. et al. (June 2016). “WISE × SuperCOSMOS PHOTOMETRIC REDSHIFT CATALOG: 20 MILLION GALAXIES OVER  $3\pi$  STERADIANS”. In: *The Astrophysical Journal Supplement Series* 225.1, p. 5. DOI: 10.3847/0067-0049/225/1/5. URL: <http://dx.doi.org/10.3847/0067-0049/225/1/5>.
- Borghi, Nicola (Apr. 2024). “Unveiling the expansion history of the universe with cosmic chronometers and gravitational waves”. PhD thesis. Alma Mater Studiorum - Università di Bologna. URL: <http://amsdottorato.unibo.it/11090/>.
- Borghi, Nicola, Michele Mancarella, Michele Moresco, et al. (Apr. 2024). “Cosmology and Astrophysics with Standard Sirens and Galaxy Catalogs in View of Future Gravitational Wave Observations”. In: *Astrophysical Journal* 964.2, 191, p. 191. DOI: 10.3847/1538-4357/ad20eb. arXiv: 2312.05302 [astro-ph.CO].
- Branchesi, Marica et al. (July 2023). “Science with the Einstein Telescope: a comparison of different designs”. In: *Journal of Cosmology and Astroparticle Physics* 2023.7, p. 068. DOI: 10.1088/1475-7516/2023/07/068.
- Carretero, J. et al. (July 2017). “CosmoHub and SciPIC: Massive cosmological data analysis, distribution and generation using a Big Data platform”. In: *Proceedings of the European Physical Society Conference on High Energy Physics. 5-12 July*, 488, p. 488.
- Castander, F. J. et al., Euclid Collaboration (2024). *Euclid. I. Overview of the Euclid mission*. arXiv: 2405.13491 [astro-ph.CO]. URL: <https://arxiv.org/abs/2405.13491>.
- Chen, Hsin-Yu, Maya Fishbach, and Daniel E. Holz (Oct. 2018). “A two per cent Hubble constant measurement from standard sirens within five years”. In: *Nature* 562.7728, pp. 545–547. ISSN: 1476-4687. DOI: 10.1038/s41586-018-0606-0. URL: <http://dx.doi.org/10.1038/s41586-018-0606-0>.
- Collaboration, LIGO Scientific, Virgo Collaboration, and KAGRA Collaboration (Nov. 2021). *GWTC-3: Compact Binary Coalescences Observed by LIGO and Virgo During the Second Part of the Third Observing Run — O3 search sensitivity estimates*. Zenodo. DOI: 10.5281/zenodo.5546676. URL: <https://doi.org/10.5281/zenodo.5546676>.
- Conselice, Christopher J. et al. (Oct. 2016). “THE EVOLUTION OF GALAXY NUMBER DENSITY AT  $z < 8$  AND ITS IMPLICATIONS”. In: *The Astrophysical Journal* 830.2, p. 83. DOI: 10.3847/0004-637X/830/2/83. URL: <https://dx.doi.org/10.3847/0004-637X/830/2/83>.
- Cutri, R.M. et al. (Feb. 2021). “VizieR Online Data Catalog: AllWISE Data Release (Cutri+2013)”. In: II/328. URL: <https://ui.adsabs.harvard.edu/abs/2014yCat..2328....0C>.
- D. A. Holz, S. A. Hughes (2005). “Using gravitational-wave standard sirens”. In: *The Astrophysical Journal* 629, pp. 15–22. DOI: 10.1086/431341. URL: <http://dx.doi.org/10.1086/431341>.
- Dálya, G. et al. (June 2018). “GLADE: A galaxy catalogue for multimessenger searches in the advanced gravitational-wave detector era”. In: *Monthly Notices of the Royal Astronomical Society* 479.2, pp. 2374–2381. ISSN: 1365-2966. DOI: 10.1093/mnras/sty1703. URL: <http://dx.doi.org/10.1093/mnras/sty1703>.
- (May 2022). “GLADE+: an extended galaxy catalogue for multimessenger searches with advanced gravitational-wave detectors”. In: *Monthly Notices of the Royal Astronomical Soci-*

- ety 514.1, pp. 1403–1411. ISSN: 1365-2966. DOI: 10.1093/mnras/stac1443. URL: <http://dx.doi.org/10.1093/mnras/stac1443>.
- Ezquiaga, Jose María and Daniel E. Holz (Aug. 2022). “Spectral Sirens: Cosmology from the Full Mass Distribution of Compact Binaries”. In: *Physical Review Letters* 129.6. DOI: 10.1103/physrevlett.129.061102. URL: <http://dx.doi.org/10.1103/PhysRevLett.129.061102>.
- Farr, W. M. and T. A. Callister (2021). *Re-Weighting Existing Samples to a Population Analysis*. <https://github.com/farr/Reweighting/blob/master-pdf/note/reweighting.pdf>.
- Farr, Will M. et al. (Jan. 2015). “Counting and confusion: Bayesian rate estimation with multiple populations”. In: *Physical Review D* 91.2, p. 023005. DOI: 10.1103/PhysRevD.91.023005.
- Fishbach, M. et al. (Jan. 2019). “A Standard Siren Measurement of the Hubble Constant from GW170817 without the Electromagnetic Counterpart”. In: *The Astrophysical Journal Letters* 871.1, p. L13. DOI: 10.3847/2041-8213/aaf96e. URL: <https://dx.doi.org/10.3847/2041-8213/aaf96e>.
- Flaminio, Raffaele (Dec. 2020). “Status and plans of the Virgo gravitational wave detector”. In: *Proc.SPIE Int.Soc.Opt.Eng.* Vol. 11445. Online, United States, p. 1144511. DOI: 10.1117/12.2565418. URL: <https://hal.science/hal-03107929>.
- Foreman-Mackey, Daniel et al. (Mar. 2013). “emcee: The MCMC Hammer”. In: *Publications of the Astronomical Society of the Pacific* 125.925, pp. 306–312. ISSN: 1538-3873. DOI: 10.1086/670067. URL: <http://dx.doi.org/10.1086/670067>.
- Fryer, Chris L. et al. (Mar. 2012). “COMPACT REMNANT MASS FUNCTION: DEPENDENCE ON THE EXPLOSION MECHANISM AND METALLICITY”. In: *The Astrophysical Journal* 749.1, p. 91. DOI: 10.1088/0004-637X/749/1/91. URL: <https://dx.doi.org/10.1088/0004-637X/749/1/91>.
- Górski, K. M. et al. (Apr. 2005). “HEALPix: A Framework for High-Resolution Discretization and Fast Analysis of Data Distributed on the Sphere”. In: *The Astrophysical Journal* 622, pp. 759–771. DOI: 10.1086/427976. eprint: arXiv:astro-ph/0409513.
- Gray, R, C Messenger, and J Veitch (Feb. 2022). “A pixelated approach to galaxy catalogue incompleteness: improving the dark siren measurement of the Hubble constant”. In: *Monthly Notices of the Royal Astronomical Society* 512.1, pp. 1127–1140. ISSN: 0035-8711. DOI: 10.1093/mnras/stac366. eprint: <https://academic.oup.com/mnras/article-pdf/512/1/1127/45303118/stac366.pdf>. URL: <https://doi.org/10.1093/mnras/stac366>.
- Gray, Rachel et al. (June 2020). “Cosmological inference using gravitational wave standard sirens: A mock data analysis”. In: *Phys. Rev. D* 101 (12), p. 122001. DOI: 10.1103/PhysRevD.101.122001. URL: <https://link.aps.org/doi/10.1103/PhysRevD.101.122001>.
- Gray, R et al. (2023). *Joint cosmological and gravitational-wave population inference using dark sirens and galaxy catalogues*. arXiv: 2308.02281 [astro-ph.CO]. URL: <https://arxiv.org/abs/2308.02281>.
- Hambly, N.C. et al. (Oct. 2001). “The SuperCOSMOS Sky Survey — I. Introduction and description”. In: *Monthly Notices of the Royal Astronomical Society* 326.4, pp. 1279–1294. ISSN: 0035-8711. DOI: 10.1111/j.1365-2966.2001.04660.x. URL: <https://doi.org/10.1111/j.1365-2966.2001.04660.x>.
- Iacovelli, Francesco et al. (Dec. 2022). “Forecasting the Detection Capabilities of Third-generation Gravitational-wave Detectors Using GWFASST”. In: *The Astrophysical Journal* 941.2, p. 208. ISSN: 1538-4357. DOI: 10.3847/1538-4357/ac9cd4. URL: <http://dx.doi.org/10.3847/1538-4357/ac9cd4>.
- Jarrett, T. H. et al. (May 2000). “2MASS Extended Source Catalog: Overview and Algorithms”. In: *The Astronomical Journal* 119.5, pp. 2498–2531. ISSN: 0004-6256. DOI: 10.1086/301330. URL: <http://dx.doi.org/10.1086/301330>.

- Karachentsev, Igor D. et al. (Apr. 2004). “A Catalog of Neighboring Galaxies”. In: *The Astronomical Journal* 127, p. 2031. DOI: 10.1086/382905. URL: <https://dx.doi.org/10.1086/382905>.
- Loredo, T. J. (2004). “Accounting for Source Uncertainties in Analyses of Astronomical Survey Data”. In: *AIP Conference Proceedings*. Vol. 735. AIP, pp. 195–206. DOI: 10.1063/1.1835214. URL: <http://dx.doi.org/10.1063/1.1835214>.
- Lyke, B. W. et al. (Aug. 2020). “The Sloan Digital Sky Survey Quasar Catalog: Sixteenth Data Release”. In: *The Astrophysical Journal Supplement Series* 250.1, p. 8. ISSN: 1538-4365. DOI: 10.3847/1538-4365/aba623. URL: <http://dx.doi.org/10.3847/1538-4365/aba623>.
- MacLeod, Chelsea L. and Craig J. Hogan (Feb. 2008). “Precision of Hubble constant derived using black hole binary absolute distances and statistical redshift information”. In: *Phys. Rev. D* 77 (4), p. 043512. DOI: 10.1103/PhysRevD.77.043512. URL: <https://link.aps.org/doi/10.1103/PhysRevD.77.043512>.
- Madau, Piero and Mark Dickinson (Sept. 2014). “Cosmic Star-Formation History”. In: *Annual Review of Astronomy and Astrophysics* 52.1, pp. 415–486. DOI: 10.1146/annurev-astro-081811-125615. URL: <http://dx.doi.org/10.1146/annurev-astro-081811-125615>.
- Maggiore, Michele (2007). *Gravitational Waves. Vol. 1: Theory and Experiments*. Oxford University Press. ISBN: 978-0-19-852074-0. DOI: 10.1093/acprof:oso/9780198570745.001.0001. – (Mar. 2018). *Gravitational Waves. Vol. 2: Astrophysics and Cosmology*. Oxford University Press. ISBN: 978-0-19-857089-9.
- Makarov, Dmitry et al. (Oct. 2014). “HyperLEDA. III. The catalogue of extragalactic distances”. In: *Astronomy & Astrophysics* 570, A13. ISSN: 1432-0746. DOI: 10.1051/0004-6361/201423496. URL: <http://dx.doi.org/10.1051/0004-6361/201423496>.
- Mandel, Ilya, Will M Farr, and Jonathan R Gair (Mar. 2019). “Extracting distribution parameters from multiple uncertain observations with selection biases”. In: *Monthly Notices of the Royal Astronomical Society* 486.1, pp. 1086–1093. DOI: 10.1093/mnras/stz896. URL: <http://dx.doi.org/10.1093/mnras/stz896>.
- Mastrogiovanni, S. et al. (Sept. 2021). “On the importance of source population models for gravitational-wave cosmology”. In: *Physical Review D* 104.6, p. 062009. DOI: 10.1103/PhysRevD.104.062009. URL: <https://ui.adsabs.harvard.edu/abs/2021PhRvD.104f2009M>.
- Mellier, Y. et al., Euclid Collaboration (May 2024). “Euclid. V. The Flagship galaxy mock catalogue: a comprehensive simulation for the Euclid mission”. In: *arXiv e-prints*. DOI: 10.48550/arXiv.2405.13495.
- Moresco, Michele et al. (Dec. 2022). “Unveiling the Universe with emerging cosmological probes”. In: *Living Reviews in Relativity* 25.1. DOI: 10.1007/s41114-022-00040-z. URL: <http://dx.doi.org/10.1007/s41114-022-00040-z>.
- Mukherjee, Suvodip and Benjamin D. Wandelt (2018). *Beyond the classical distance-redshift test: cross-correlating redshift-free standard candles and sirens with redshift surveys*. arXiv: 1808.06615 [astro-ph.CO]. URL: <https://arxiv.org/abs/1808.06615>.
- Ochsenbein, F. et al. (Apr. 2000). “The VizieR database of astronomical catalogues”. In: *Astronomy and Astrophysics Supplement* 143, pp. 23–32. DOI: 10.1051/aas:2000169. URL: <https://ui.adsabs.harvard.edu/abs/2000Astronomy%20and%20AstrophysicsS..143...23O>.
- Oguri, Masamune (Apr. 2016). “Measuring the distance-redshift relation with the cross-correlation of gravitational wave standard sirens and galaxies”. In: *Physical Review D* 93.8. DOI: 10.1103/physrevd.93.083511. URL: <http://dx.doi.org/10.1103/PhysRevD.93.083511>.
- Pâris, I. et al. (Jan. 2017). “The Sloan Digital Sky Survey Quasar Catalog: Twelfth data release”. In: *Astronomy & Astrophysics* 597, A79. ISSN: 1432-0746. DOI: 10.1051/0004-6361/201527999. URL: <http://dx.doi.org/10.1051/0004-6361/201527999>.

- Paturel, G. et al. (Jan. 1988). “The extragalactic database of the Lyon-Meudon Observatories.” In: *European Southern Observatory Conference and Workshop Proceedings*. Vol. 28, pp. 435–440. URL: <https://ui.adsabs.harvard.edu/abs/1988ESOC...28..435P>.
- Prugniel, Ph. et al. (Jan. 1999). “The HYPERCAT Database”. In: *Star Formation in Early Type Galaxies*. Vol. 163, p. 296. URL: <https://ui.adsabs.harvard.edu/abs/1999ASPC...163..296P>.
- Raveri, Marco, Cyrille Doux, and Shivam Pandey (2024). *Understanding posterior projection effects with normalizing flows*. arXiv: 2409.09101 [astro-ph.IM]. URL: <https://arxiv.org/abs/2409.09101>.
- Riess, Adam G. et al. (Sept. 1998). “Observational Evidence from Supernovae for an Accelerating Universe and a Cosmological Constant”. In: *The Astronomical Journal* 116.3, pp. 1009–1038. DOI: 10.1086/300499. URL: <http://dx.doi.org/10.1086/300499>.
- (July 2022). “A Comprehensive Measurement of the Local Value of the Hubble Constant with 1 km s<sup>-1</sup> Mpc<sup>-1</sup> Uncertainty from the Hubble Space Telescope and the SH0ES Team”. In: *The Astrophysical Journal Letters* 934.1, p. L7. DOI: 10.3847/2041-8213/ac5c5b. URL: <http://dx.doi.org/10.3847/2041-8213/ac5c5b>.
- Schutz, B. F. (1986). “Determining the Hubble constant from gravitational wave observations”. In: *Nature* 323, pp. 310–311. DOI: 10.1038/323310a0. URL: <https://doi.org/10.1038/323310a0>.
- Tagliazucchi, M. et al. (2025). *in preparation*.
- Talbot, Colm and Eric Thrane (Apr. 2018). “Measuring the Binary Black Hole Mass Spectrum with an Astrophysically Motivated Parameterization”. In: *The Astrophysical Journal* 856.2, p. 173. DOI: 10.3847/1538-4357/aab34c. URL: <https://dx.doi.org/10.3847/1538-4357/aab34c>.
- Tallada, P. et al. (2020). “CosmoHub: Interactive exploration and distribution of astronomical data on Hadoop”. In: *Astronomy and Computing* 32, p. 100391. ISSN: 2213-1337. DOI: <https://doi.org/10.1016/j.ascom.2020.100391>.
- Tully, R. Brent (Oct. 1987). “Nearby Groups of Galaxies. II. an All-Sky Survey within 3000 Kilometers per Second”. In: *The Astrophysical Journal* 321, p. 280. DOI: 10.1086/165629. URL: <https://ui.adsabs.harvard.edu/abs/1987ApJ...321..280T>.
- Tully, R. Brent et al. (June 2009). “THE EXTRAGALACTIC DISTANCE DATABASE”. In: *The Astronomical Journal* 138, p. 323. DOI: 10.1088/0004-6256/138/2/323. URL: <https://dx.doi.org/10.1088/0004-6256/138/2/323>.
- Verde, Licia, Tommaso Treu, and Adam G. Riess (Sept. 2019). “Tensions between the early and late Universe”. In: *Nature Astronomy* 3.10, pp. 891–895. DOI: 10.1038/s41550-019-0902-0. URL: <http://dx.doi.org/10.1038/s41550-019-0902-0>.
- White, D. J. et al. (Mar. 2011). “A list of galaxies for gravitational wave searches”. In: *Classical and Quantum Gravity* 28.8, p. 085016. ISSN: 1361-6382. DOI: 10.1088/0264-9381/28/8/085016. URL: <http://dx.doi.org/10.1088/0264-9381/28/8/085016>.
- Wright, E. L. et al. (Dec. 2010). “The Wide-field Infrared Survey Explorer (WISE): Mission Description and Initial On-orbit Performance”. In: *The Astronomical Journal* 140.6, pp. 1868–1881. DOI: 10.1088/0004-6256/140/6/1868. URL: <https://ui.adsabs.harvard.edu/abs/2010AJ....140.1868W>.
- Ye, Christine and Maya Fishbach (Aug. 2021). “Cosmology with standard sirens at cosmic noon”. In: *Phys. Rev. D* 104 (4), p. 043507. DOI: 10.1103/PhysRevD.104.043507. URL: <https://link.aps.org/doi/10.1103/PhysRevD.104.043507>.
- Zonca, Andrea et al. (Mar. 2019). “healpy: equal area pixelization and spherical harmonics transforms for data on the sphere in Python”. In: *Journal of Open Source Software* 4.35, p. 1298. DOI: 10.21105/joss.01298. URL: <https://doi.org/10.21105/joss.01298>.